KU LEUVEN

FACULTY OF BIOSCIENCE ENGINEERING

The effects of urban green space on mitigating urban heat islands and improving thermal comfort: a case study of Leuven, Belgium

De effecten van stedelijk groen op het mitigeren van stedelijke hitte-eilanden en het verbeteren van thermisch comfort: een case study in Leuven, België

Promotor:
Prof. Ben Somers
Department of Earth and Environmental Sciences
Division of Forest, Nature and Landscape

Dissertation presented in
Fulfillment of the requirements
for the degree of Master of Bioscience Engineering:
Agro- and Ecosystems Engineering

Eva Beele

June 2020

Acknowledgements

I am very grateful to have gotten the thesis subject I was aiming for and that it turned out to be as fun and interesting as I hoped it would be. I would like to thank my promotor Ben Somers for his constructive advice and good ideas, both throughout the year as in the final stages of completing this manuscript. I would also like to thank my daily supervisor Jingli for helping me with problems I encountered during my analyses and his eagerness in helping explain unexpected results. Without your green map or guidance during the fieldwork, this thesis would not have been possible. Another thank you goes out to the KMI and especially Maarten for his help in setting up the Garmon network and continuous advice during the meteorological analyses. I would also like to thank the city of Leuven, Leuven 2030 and especially Hanne for helping us find suitable locations and obtaining the necessary approvals for installing the weather stations. Also Laura and Margot deserve my thanks as they took over the administrative burden of the project when I needed to focus on the data itself.

My fieldwork would not have been possible, and to be honest not have been half as fun without the job students of the Forest, Nature and Landscape Division – Jonas, Floris, Lennert and Karlien. Thank you for your hard work in these 30°C+ weather conditions, not everyone would have done that. Of course, I would also like to thank the citizens of Leuven for their massive response and eagerness to participate in the project.

Lastly, a big thank you to my friends and family for not only letting me talk on and on about weather stations and the mitigating impacts of urban green, but also for showing your interest into the subject and engaging in our discussions on the topic. Very much appreciated!

Scientific summary

The world's urban population has rapidly grown during the last decennia, leading to a phenomenon called urban heat islands (UHIs). These UHIs are characterized by higher air temperatures in city centers compared to their rural surroundings and negatively affect human health and well-being. The creation and enhancement of urban green infrastructure (UGI) are one of the most promising solutions for mitigating urban heat through evaporation and shading. These cooling benefits are however highly affected by the composition and configuration of urban green. Since cities generally only have limited space available for urban green, an optimal spatial configuration of UGI would help city managers and decision makers to plan and manage their urban green in order to maximize their cooling effect.

In this research we therefore studied the urban heat island in Leuven and evaluated the effects of UGI composition and configuration on urban air temperatures and the Thom's discomfort index. We firstly investigated the spatio-temporal variations of urban air temperatures and human discomfort using a newly implemented in situ weather station network. Subsequently we examined how the composition and configuration of different urban green types can impact these urban air temperatures and discomfort indices on multiple spatial and temporal extents. The composition and configuration of the different urban green types were measured by a series of landscape metrics, which were calculated based on a high-resolution green map with an overall accuracy of 91%.

The results show that both the composition and the configuration of high and low green matter in the mitigation of urban heat islands. This mitigating impact of different urban green types, high and low green, does however vary for different spatial and temporal scales. At night, the composition and spatial configuration of low green was found to be the most important mitigating factor along all spatial extents. Increasing low green's percentage cover by 50%, lowers night-time temperature with 4°C. During daytime, high green was more effective in reducing urban air temperatures and human discomfort. The resulting temperature decrease was however smaller, a 50% increase in high green's percentage cover decreased air temperature with 2°C.

This research may provide important insights for urban green planning and design. We have shown that different urban green types, shapes and sizes at multiple spatial scales are needed to improve thermal comfort of citizens during both night and day.

List of abbreviations

AREA_MN	Mean patch size
AUHI	Atmospheric urban heat island
Cfb	Temperate climate with no dry season and a warm summer [Köppen]
CHM	Canopy height model
DI	Discomfort index
DTM	Digital terrain model
ED	Edge density
EMR	Electromagnetic radiation
ESP	Estimation of scale parameter
LCZ	Local climate zones
LiDAR	Light detection and ranging
LPI	Largest patch index
LST	Land surface temperature
LV	Local variance
PAR	Photosynthetically active region
PD	Patch density
PLAND	Percentage cover
PP	Polsby-Popper
MIR	Mid infrared (region)
MRS	Multi-resolution segmentation
NDVI	Normalized difference vegetation index
NIR	Near infrared (region)
OBIA	Object based image analysis
RH	Relative humidity
RMI	Royal meteorological institute
RMSE	Root mean square error
ROC	Rate of change
SD	Standard deviation
SHAPE_MN	Mean shape index
SUHI	Surface urban heat island
SVF	Sky view factor
SWIR	Short-wave infrared (region)

T	Temperature
Tbias	Temperature bias
TIR	Thermal infrared (region)
UAT	Urban air temperature
UBL	Urban boundary layer
UCL	Urban canopy layer
UGI	Urban green infrastructure
UHI	Urban heat island
UV	Ultraviolet (region)
VIS	Visible (region)

List of tables

List of figures

Contents

1 Introduction

1.1 Context

The world's urban population has grown rapidly from 751 million in 1950 to 4.2 billion in 2018. (UN, 2018). This means that today more than 50% of the global population lives in urban areas. Projections show that this urbanization together with an increasing overall world's population could add another 2.5 billion people to urban areas by 2050. In 2018, 74% of the European population was living in cities, making it the third most urbanized region in the world (UN, 2018). The urban population in Belgium has shown a steady increase from 92% in 1960 to 98% in 2017 (The World Bank Group, 2017).

This worldwide urbanization has led to the phenomenon of urban heat islands (UHIs), which are characterized by higher air temperatures in cities compared to their rural surroundings, during both day- and night-time (Arnfield, 2003; Marando et al., 2019). These temperature differences are typically due to surface modifications in which soil and vegetation are replaced by impervious soil layers like asphalt and concrete. Such modifications result in a different albedo, thermal emissivity and heat capacity of the urban landscape in comparison to its natural and rural environment. Additionally, heat released from anthropogenic sources will affect urban temperatures (Marando et al., 2019; Zhou et al., 2011).

Increased temperatures due to UHIs lead to increased water and energy consumption and can affect the composition and distribution of local biotic communities (Marando et al., 2019). Increased urban temperatures also directly affect human health and well-being, shown by increased health risks and mortality rates during heat waves in cities worldwide (Marando et al., 2019). Furthermore, increased temperatures will have a negative effect on air quality, due to an increased production of ozone in combination with a limited horizontal air dispersion (Marando et al., 2019; Zhou et al., 2017).

One of the most effective solutions for cooling UHIs is the creation and enhancement of Urban Green Infrastructure (UGI) (Marando et al., 2019). UGI can be defined as "a strategically planned network of natural and semi-natural areas with other environmental features designed and managed to deliver a wide range of ecosystem services" (European Commission, 2013).

UGI and especially trees have been identified as a promising factor to mitigate urban air temperatures. This reduction in air temperature can be explained by several mechanisms. The first and most important mechanism reported by previous studies is evapotranspiration (Marando et al., 2019). Water is transpired trough the stomata of leaves by absorbing energy from solar radiation, resulting in an increased latent rather than sensible heat flux (Gunawardena et al., 2017; Marando et al., 2019; Mohammed & Salman, 2018; Qian et al., 2018). Evapotranspiration additionally increases the air humidity, which will help relieve the UHI effect (Xiao et al., 2018). Secondly, leaves and branches intercept incoming shortwave solar radiation, hereby reducing the amount of radiation that reaches the underlying surface. This process is known as the shading effect (Marando et al., 2019; Mohammed & Salman, 2018; Qian et al., 2018). The green infrastructures will also absorb less heat due to their lower specific heat capacity in comparison with their impervious surroundings. Lastly, vegetation has a higher albedo than its non-natural environment, resulting in larger amount of reflected energy (Mohammed & Salman, 2018).

1.2 Problem statement and objectives

The benefits of urban green described above are highly affected by their composition and configuration (Qian et al., 2018; Zhou et al., 2011, 2017). The composition refers to the abundance and variability of urban green infrastructure, while the configuration refers to the spatial arrangement or distribution of urban green infrastructure (Zhou et al., 2011).

Previous UHI research has examined the spatial and temporal variations of UHIs (dos Santos et al., 2017) and have primarily focused on urban green's composition, especially expressed as the percentage of greenspace, as a possible solution towards urban cooling (Weng et al., 2004; Zhou et al., 2011, 2017). These studies have shown that an increasing percentage cover of urban green will negatively affect urban air temperatures and land surface temperatures. In addition to the total amount of vegetation, few studies have examined the effects of shape and size of vegetation patches on air temperatures, mostly in urban parks (Cao et al., 2010; Marando et al., 2019; Xiao et al., 2018). These studies however neglect the spatial configuration of these vegetation patches within the total landscape matrix and generally consider the isolated impact of a single urban green patch, such as a park.

Recent studies on UHI mitigation have included the effect of spatial configuration of urban green in the landscape pattern (Fan et al., 2015; Qian et al., 2018; Zhou et al., 2011, 2017). Since cities generally only have limited space available for urban green, an optimal spatial configuration of UGI would help managers and decision makers to plan and manage their urban green infrastructure in order to maximize their cooling effect (Zhou et al., 2017). These studies use landscape metrics to measure the spatial patterns of urban green. Mean patch size, edge density, patch density, largest patch index and mean shape index are examples of such configuration metrics. All these could potentially affect air temperature (Fan et al., 2015; Qian et al., 2018; Zhou et al., 2011, 2017). Yet, a comprehensive understanding of how the heterogeneity of urban green affects temperature variations on multiple temporal and spatial scales is still lacking (Qian et al., 2018; Yan et al., 2014).

Most of the previous studies focused on the effect of UGI on land surface temperature (LST) (Fan et al., 2015; Zhou et al., 2011, 2017), while only a few paid particular attention to urban air temperatures (Qian et al., 2018). A study of Arnfield (2003) however explains that there is no consistent relationship between the two. Especially under calm conditions, LST are more dependent on microscale site characterizations. The overabundance of studies based on LST can be easily explained by the rather simple extraction method of LST from thermal remote sensing satellite data, which deliver spatially continuous data over large geographical extents (Arnfield, 2003; Qian et al., 2018). It is however proven that, opposed to LST, urban air temperatures are more closely related to human health and comfort, and thus deserve at least an equal amount of attention (Qian et al., 2018; Yan et al., 2014).

In this thesis we will therefore examine the effect of composition and more importantly configuration of UGI on urban air temperatures and the Thom's discomfort index using different landscape metrics. More specifically, we will study the spatio-temporal variations of the urban air temperatures and the discomfort index in and around the city of Leuven, Belgium. Subsequently, we will determine how the composition and configuration of the urban green infrastructure impact these urban air temperatures and discomfort index. This will be done by (1) characterizing Leuven's urban heat island on different temporal and spatial scales using a newly implemented in-situ weather station network, (2) producing a detailed green map of Leuven using both high resolution Pleiades satellite images and LiDAR imagery and an object based classification method, (3) performing a GIS analysis to examine the urban green's composition and configuration using multiple landscape metrices and lastly (4) using a

correlation index and simple regression models to measure the effect, cooling distance and contribution of different urban green classes to mitigate urban air temperatures.

2 Literature review

2.1 Urbanisation

Urbanisation is a complex process referring to the population shift from dispersed rural settlements towards densely populated urban areas. As a consequence, urban settlements will expand rapidly at the expanse of undeveloped rural areas, a phenomenon known as urban sprawl (UN, 2019).

The world's urban population has grown rapidly from 751 million in 1950 to 4.2 billion in 2018 as can be seen in figure 2.1. This means that today more than 50% of the global population lives in urban areas. Projections show that this urbanization together with an increasing overall world's population could add another 2.5 billion people to urban areas by 2050 (UN, 2018). In 2018, almost three quarters of the European population was living in cities, making it the third most urbanized region in the world (UN, 2018). This percentage is expected to rise to just over 80% by 2050 (Vidal-Abarca et al., 2016). Within Europe, urbanization has shown a positive relation with income, labor productivity, technological adaptation and competitiveness levels, resulting in a lower urbanization growth for the developing Europe compared to the more advanced Europe (Vidal-Abarca et al., 2016). The urban population in Belgium has shown a steady increase from 92% in 1960 to 98% in 2017 (The World Bank Group, 2017). With a population density of 376 inhabitants/km^2, Belgium is one of the smallest and most densely populated countries in western Europe (The World Bank Group, 2018).

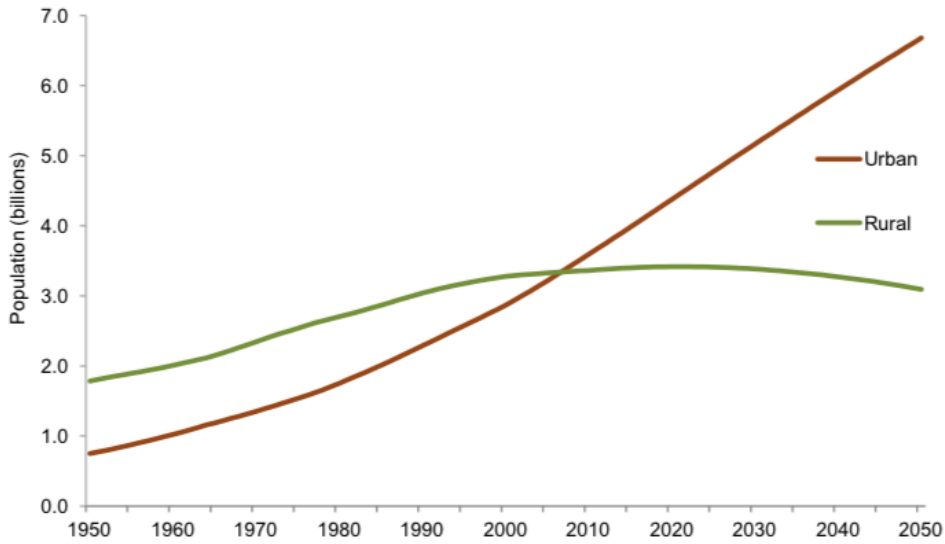

Figure 2.1: Urban and rural population growth from 1950 to 2015 UN, 2019).

2.2 Urban Heat Island (UHI) effect

2.2.1 Definition

The increased urbanisation in the last decennia has led to a phenomenon called urban heat islands (UHIs). These UHIs, characterized by higher temperatures in the city centres compared to their rural and more natural surroundings, were first measured and described by Lake Howard during the 19th century (Howard, 1833). Oke (1995) later clarifies the "island" term by comparing the isotherm air temperature patterns with the contours of an island located within the sea of the cooler rural surroundings. The UHI intensity is defined as "the difference in temperature between the urban areas and rural surroundings" (Roth et al., 1989; van Hove et al., 2015).

During the 20th century the need to define several types of heat islands according to various surfaces and different layers within the urban atmosphere became more important (Oke, 1995; Roth et al., 1989). Two broad types of UHIs were recognised: surface UHIs (SUHI) and atmospheric UHIs (AUHIs). Just like the name suggests, surface UHIs describe the difference in land surface temperature between the city center and their rural environment, while atmospheric UHIs focus on the difference in air temperatures between both locations (U.S. EPA, 2008). Previous research has shown that surface heat islands are often greater by day, while the reverse is true for atmospheric heat islands (Oke, 1995; Roth et al., 1989; Zhou et al., 2011). Figure 2.2 partly confirms his theory. The transect shows a higher variation in surface temperatures compared to air temperatures during daytime. During night time, however, both temperatures show similar values (U.S. EPA, 2008).

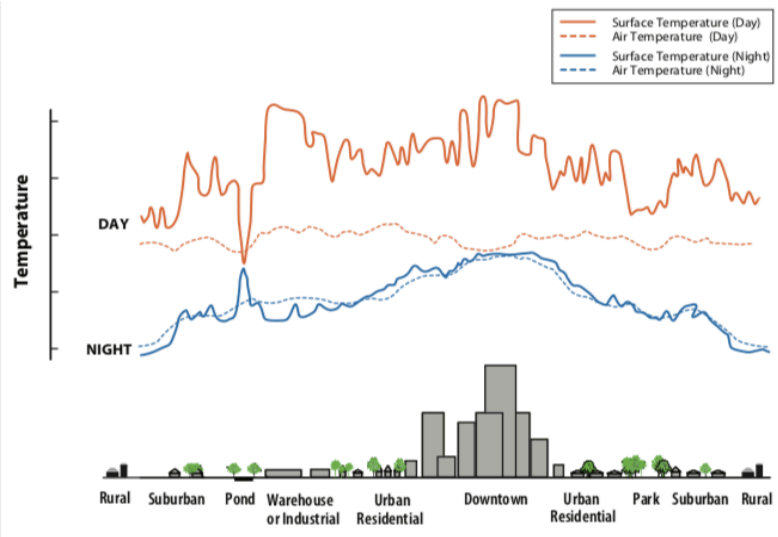

Figure 2.2: Variations in surface and air temperatures during day- and night-time. "The temperatures displayed above do not represent absolute temperature values or any one particular measured heat island" (U.S. EPA, 2008).

The surface urban heat island is generally measured by aircraft-borne thermal remote sensors. These techniques allow to obtain continuous data over large geographical extents (Roth et al., 1989; U.S. EPA, 2008; Voogt & Oke, 2003).

When studying the atmospheric UHI, Oke (1976) stated that the urban atmosphere has to be divided into two layers: the urban canopy layer (UCL) and the urban boundary layer (UBL). Both layers are closely coupled but differ in magnitude and underlying generation processes (Arnfield, 2003). The UCL is that layer of the atmosphere going from the land surface upwards until the mean building height in which processes of airflow are controlled by microscale site-specific characteristics. The UBL is situated above the UCL and is that part of the planetary boundary layer (PBL) whose characteristics are still influenced by the urban landscape below (Arnfield, 2003; Oke, 1976; Roth et al., 1989; U.S. EPA, 2008; Voogt & Oke, 2003). Figure 2.3 shows that the UBL has a varying vertical scale, going from 100 meters at nighttime up to 1500 meters during the day (Bassett et al., 2016).

The UBL is often described as a mesoscale or local concept controlled by processes at large spatial and temporal scale. The UCL, on the contrary, is a microscale concept that measures the local climate only. This local climate is influenced by the immediate building geometry and materials within the urban landscape, also denoted as the "urban roughness" (Arnfield, 2003; Oke, 1976). Since this layer is occupied by people, it is of great importance in human health and comfort studies. For this reason, the more general term UHI is often used to describe the canopy layer UHI, the same will be done in this thesis (Bassett et al., 2016; Gunawardena et al., 2017).

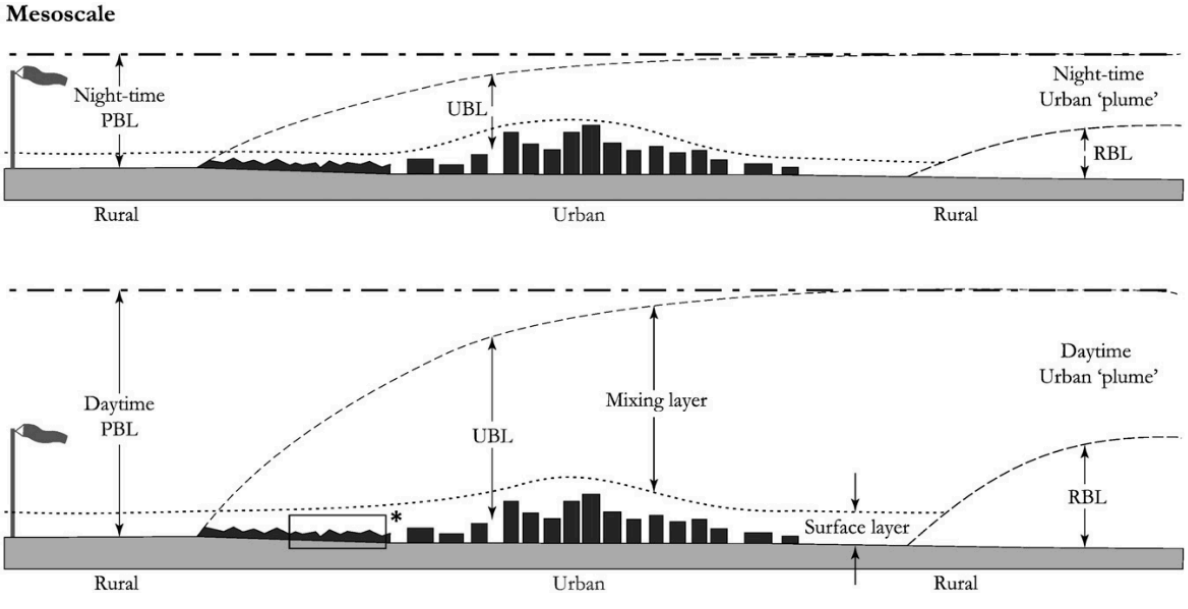

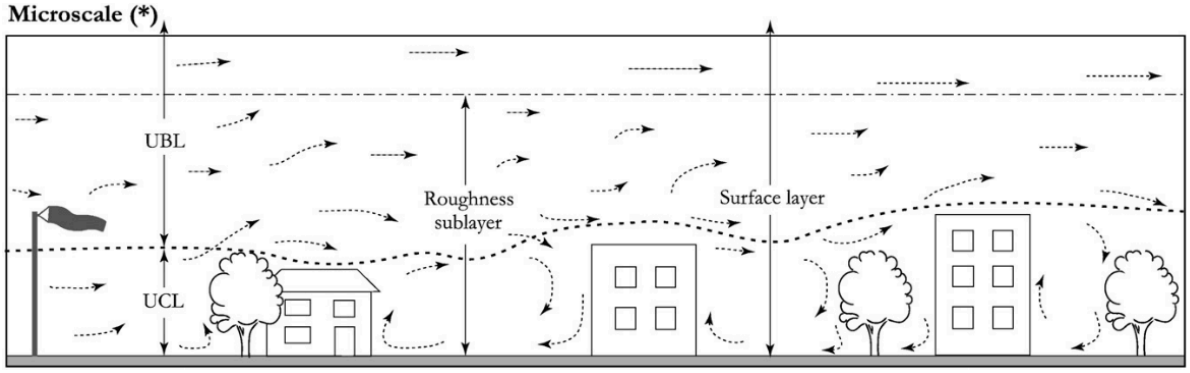

Figure 2.3: Canopy and boundary layers over a city and its rural environment (based on Oke (1987), edited from Gunawardena et al. (2017))

Canopy layer UHIs are generally measured by in-situ sensors at a standard height either fixed on a certain location or mounted on mobile devices, while boundary layer measurements are made using more specializes sensor platforms or aircraft-mounted instruments (Voogt & Oke, 2003).

2.2.2 Causes

An UHI develops through the absorption of solar radiance during the day and the subsequent release during night time. Anthropogenic changes to this surface energy balance greatly influence the intensity of UHIs. These anthropogenic changes include urban morphology, impervious and artificial construction materials and human activities (Bassett et al., 2016; Marando et al., 2019; U.S. EPA, 2008; Zhou et al., 2011).

The increased urbanisation in the last decennia has significantly altered the urban morphology of cities worldwide. The height and density of buildings has increased resulting into a reduced sky view factor (SVF). This SVF is the fraction of visible sky from the ground and is closely related to narrow canyon streets (U.S. EPA, 2008). Within these canyons both short and long wave radiation are entrapped hereby reducing the amount of longwave radiation loss during the night. The more densely built up areas have increased the surface roughness, hereby diminishing wind flow and preventing heat evacuation (Bassett et al., 2016).

The higher fraction of impervious materials in cities greatly diminishes the possible evapotranspiration, which will lead to increased surface and air temperatures (Bassett et al., 2016; U.S. EPA, 2008). Additionally, these impervious and artificial construction materials have different reflective properties, thermal emissivity's and heat capacity's than the natural materials present in the surrounding rural areas. The typical dark-coloured materials used in

cities have a lower solar reflectance or albedo, leading to a greater absorbance of the sun's energy. Also the thermal emissivity of materials play a role. A higher thermal emissivity will cause a material to emit more longwave infrared radiation, which can increase UHI intensities. Lastly the heat capacity, a measure for the ability of a material to store heat, will influence the UHI development. Most construction materials, like steel and concrete have greater heat capacities in comparison with the more natural materials, including soil and sand. As a result more heat is absorbed by cities, hereby contributing to the formation of UHIs (U.S. EPA, 2008; Zhou et al., 2011).

Lastly, anthropogenic heat will further contribute to the development of UHIs. This heat, released by human activities, has a wide variety of sources including transport, cooling and heating processes and industries (Bassett et al., 2016; Marando et al., 2019; U.S. EPA, 2008).

2.2.3 Diurnal and seasonal variations

UHI intensities have both diurnal and seasonal variations (Bassett et al., 2016; Roth et al., 1989; U.S. EPA, 2008; van Hove et al., 2015). Atmospheric UHIs are often weak in the morning but further develop during the day as the build environment absorbs solar radiance (Bassett et al., 2016; van Hove et al., 2015). During night-time subsequent heat release takes place (Bassett et al., 2016; van Hove et al., 2015). Because the urban environment is characterized by a reduced longwave radiation loss and lower albedo, the cooling of cities will be delayed compared to their rural surroundings, resulting in a maximum UHI intensity at night (Bassett et al., 2016; Hamdi & Schayes, 2008; Nichol et al., 2009; U.S. EPA, 2008). The specific timing of this maximum UHI intensity depends on season, prevailing weather conditions and the surface properties (U.S. EPA, 2008). Atmospheric UHIs are typically more intense in wintertime (Roth et al., 1989; U.S. EPA, 2008). Roth et al. (1989) explains that these seasonal variations are related to cyclical changes of solar radiation, synoptic weather type, plant phenology, moisture availability or fuel use.

2.2.4 Consequences

Increased temperatures due to UHIs will lead to an intensified water and energy consumption needed for summer building cooling (Marando et al., 2019; U.S. EPA, 2008; Zhou et al., 2011, 2017). Santamouris et al. (2015) found that the potential increase in peak electricity demands

per degree of temperature rise can escalate from 0.45% to 4.6%. This demands are influenced by the building's structures, climate zone and general city form (Santamouris et al., 2015).

If the increased energy demand explained above is produced by the combustion of fossil fuels, higher levels of air pollution and greenhouse gas emissions can be expected (U.S. EPA, 2008). In addition, higher temperatures within the city centre will accelerate the formation of ground level ozone. This tropospheric ozone is created by the chemical reaction between nitrogen (NOx gases) and volatile organic compounds (VOCs) in the presence of sunlight. Higher temperatures and more solar radiation will shift the equilibrium to the right, hereby creating direct consequences for human health (U.S. EPA, 2008; Zhou et al., 2011, 2017).

Also heat excess present in cities will affect human health and wellbeing, shown by increased mortality rates during heat waves worldwide (Marando et al., 2019; U.S. EPA, 2008; Zhou et al., 2017). In the EU, heat related mortalities are expected to increase by 1% to 4% for every one-degree rise in temperature (Sajani et al., 2016). The Discomfort Index (DI) proposed by Thom (1959) is one of the most used indexes to calculate the discomfort on a specific day and time and can be used in the development of heat risk alert systems (Georgi & Zafiriadis, 2006). The DI is defined as "a measure of the reaction of the human body to a combination of heat and humidity" (Thom, 1959).

Lastly, the composition, distribution and phenology of species will be affected as a consequence of the UHI (Marando et al., 2019; Zhou et al., 2011, 2017). A 10 yearlong study from White et al. (2002) revealed that the length of the growing season in urban areas is expanded by 8 days in comparison with the rural environment. Reductions in fractional cover and greenness amplitude on the other hand suggest a lower productivity within the urban areas (White et al., 2002).

2.2.5 Solutions

Projections show that heat waves and higher summer temperatures will become increasingly regular by the end of the century due to global climate change (Bassett et al., 2016; Solecki et al., 2005). In combination with the increasing urbanisation, well-developed strategies will be needed to secure to healthy quality of life within our cities (Bassett et al., 2016).

Two possible reactions to the UHI exist: adaptation or mitigation. In UHI adaptation strategies a person tries to deal with the consequences of UHIs, mostly increased night temperatures, while UHI mitigation strategies try to prevent or reduce these consequences (Solecki et al., 2005).

Adaptation strategies include wearing light clothes, prevent inside cooking and try to find locations to sleep outside. Using air conditioners is an adaptation strategy as well but has major drawbacks (Solecki et al., 2005). Their high energy demands will generally lead to increased emissions of greenhouse gases, who further contribute to the formation of UHI (U.S. EPA, 2008).

Because of these limitations, mitigation strategies are becoming more and more important. The two most promising mitigations strategies are an increased vegetation cover and the implementation of higher albedo surfaces. Since the mitigating factors of urban green are a central topic in this thesis, they will be discussed in more detail below (section 2.3). Next to a low vegetation cover, cities contain a high amount of non-reflecting impervious surfaces characterized by a low albedo and high heat capacity. They absorb great amounts of solar radiation during the day and re-emit this radiation at night. Altering these surfaces both at ground and roof level into lighter-colored materials, also called cool pavements and cool roofs, can greatly reduce the UHI effect (Solecki et al., 2005). Additionally, reducing anthropogenic heat releases or optimizing the SVF in new developments can help in mitigating the UHI effect (Lee et al., 2014).

2.3 Urban green infrastructure (UGI) as a solution for UHIs

The enhancement of sustainable cities can be achieved through the realisation of Nature-Based solutions, which are defined as “inspired by, supported by or copied from nature; both using and enhancing existing solutions to challenges, as well as exploring more novel solutions” (European Commission, 2015). In other words, nature-based solutions try to use natural processes within the built environment to address and ultimately solve environmental and socio-economic problems (Marando et al., 2019).

One of the most effective Nature-Based solutions is the creation and enhancement of the urban green infrastructure (UGI), such as urban forests, parks, individual street trees, verges, private

gardens, transport corridors and vegetated roofs and façades (Gunawardena et al., 2017; Marando et al., 2019). The UGI can be defined as a strategically planned interconnected network of natural and semi-natural areas designed and managed to deliver a wide range of ecosystem services, hereby offering ecological, social and economic benefits (European Commission, 2013; Gunawardena et al., 2017; Marando et al., 2019). These ecosystem services include the mitigation of the UHI effect, the improvement of air quality, the reduction of runoff and the reduction of energy use.

Urban green will mitigate the UHI effect through a combination of several mechanisms. The first and most important mechanism reported by previous studies is evapotranspiration, known as the combined process of transpiration from the plants itself and evaporation from the soils underneath (Gunawardena et al., 2017; Marando et al., 2019; Mohammed & Salman, 2018). This process is positively influenced by the availability of moisture and wind flow (Gunawardena et al., 2017). During evapotranspiration water is transpired through the stomata of leaves by absorbing energy from solar radiation, resulting in an increased latent rather than sensible heat flux. As a consequence both canopy and surrounding air temperatures will decrease (Gunawardena et al., 2017; Marando et al., 2019; Qian et al., 2018). Evapotranspiration additionally increases the air humidity, which will help relieve the UHI effect (Xiao et al., 2018). Secondly, leaves and branches will intercept incoming shortwave radiation hereby reducing the amount of radiation that reaches the underlying surface, a process known as the shading effect (Gunawardena et al., 2017; Marando et al., 2019; Mohammed & Salman, 2018; Qian et al., 2018; Solecki et al., 2005). The green infrastructures will also absorb less heat due to their lower specific heat capacity in comparison with their impervious surroundings. Lastly, vegetation has a higher albedo than its non-natural environment, resulting in larger amount of reflected energy (Mohammed & Salman, 2018).

Additionally, vegetation will improve air quality and reduce runoff in cities. Two processes which will indirectly help mitigate high temperatures. An improved air quality is obtained by both the direct dry deposition of pollutant molecules on the vegetation surface and the absorption of small gaseous pollutants by the leaves (Gunawardena et al., 2017). Through urban cooling vegetation can also mitigate the formation of ground level ozone (Solecki et al., 2005). The reduction of these emissions will minimize atmospheric scattering and the absorption of long- and short-wave radiation, resulting in a cooler city climate. Besides improving air quality, the urban green canopy will intercept precipitation and assist absorption, hereby reducing the

amount of run-off. This reduced run-off will lead to a higher available moisture content, which positively influences evapotranspiration (Gunawardena et al., 2017).

Lastly, a higher and well-situated vegetation cover in cities can help reduce energy use during both summer and winter. During summer, trees located on the east, south or west of a building can intercept the incoming solar radiation and provide shade, hereby reducing the need for air-conditioning. In winter time vegetation can be used as isolation to shield buildings from cold winds. Since broadleaved trees will lose their leaves, they lose their ability to block incoming radiation, which will in turn reduce heating costs (Solecki et al., 2005).

2.4 Remote sensing of vegetation

2.4.1 Theoretical background

Remote sensing is a technique used to detect and monitor the physical characteristics of an object of interest using instruments that are not in direct contact with this object. These instruments, or specifically sensors, can be mounted on a satellite, manned airplane, remotely piloted aerial system or simply carried by hand. The sensors measure the electromagnetic radiation (EMR) that is reflected from or emitted by vegetation present on the earth's surface (Jones & Vaughan, 2010).

Electromagnetic radiation is a form of energy consisting of electric and magnetic fields. Within these fields the magnitude and direction of the electric and magnetic vector change in time, oscillating in phase at right angles to each other. The resulting electromagnetic wave does not need a medium to travel and its characteristic velocity equals 2.99×10^8 m s^{-1} in vacuum, also known as the speed of light. The continuum of all electromagnetic waves with different frequencies and wavelengths is defined as the electromagnetic spectrum. This spectrum can be divided into multiple regions. The visible (VIS) region, ranging from 400 to 700 nm, comprises only a small part of the spectrum corresponding with the photosynthetically active region (PAR). This is the only part visible through the human eye. The ultraviolet (UV) region, found left of the VIS region, has smaller wavelengths ranging from 10 to 400 nm. Wavelengths smaller than 10 nm belong to the high-energetic X-rays and γ-rays. On the right side of the VIS region, the longer wavelengths of the infrared are found. They are split up into the near infrared (NIR) ranging from 700 nm to 1 μm, the short-wave infrared (SWIR) with wavelengths up to 3 μm, the mid-infrared (MIR) up to 8 μm, the thermal infrared (TIR) up to 15 μm and lastly the

far infrared with 100 μm as upper boundary. The least energetic microwaves and radio waves can reach a length of several meters (Jones & Vaughan, 2010).

There are several wavelength dependent interactions possible between the EMR and the target surface, here vegetation. A part of the EMR will be transmitted through the plant canopies, hereby not interacting with the surface material. A second type of interaction is the absorption of the incoming solar radiation. In plants, the most dominant absorption is performed by chlorophyll and other pigments within the visible part of the spectrum. These pigments mainly absorb red and blue wavelengths, the green part of the spectrum is less strongly absorbed, explaining the green appearance of vegetation. Solar radiation that is not transmitted or absorbed by the surface material is directly reflected back to space. Depending on the roughness of the surface, smooth or rough, both specular and diffuse reflection are possible. In the first case a ray of light is reflected at an angle equal to the incidence angle, in the second case scattering occurs, in which the rays are reflected at different angles. It is this reflection that is measured by remote sensors and will give insights into the plant's physical characteristics (Jones & Vaughan, 2010).

2.4.2 Leaf radiative properties

The amount of radiation that is reflected, absorbed and transmitted by the plant is directly influenced by its characteristics, such as leaf structure, leaf maturity and moisture content. Understanding the interaction between EMR and plant tissues is crucial in order to derive correct conclusions (Jones & Vaughan, 2010).

In the longer wavelength UV region, most of the incoming radiation is absorbed by the cuticular wax of the plants. Radiation below 300 nm falls outside the atmospheric window and won't reach the earth's surface. In the VIS region 85 to 90% of the PAR is absorbed by pigments and will be used as energy for photosynthesis. Since chlorophyll is the most dominant pigment, the vegetation spectra show greater absorption in the blue and red parts of the spectra. The NIR regions is known as the absorptive no man's land because no strong absorptions occur. Because of the chaotic internal leaf structure radiation is diffused and scattered in all directions leading to ½ transmittance and ½ reflectance. Within the SWIR region strong water absorption bands occur. Additionally, absorption by cellulose and lignin take place (Jones & Vaughan, 2010).

A more complex leaf structure or older well-developed leaf with more pronounced sponsparenchym will encounter higher internal scattering and higher reflectance in the NIR. When the leaves become too old, their tissue will break down resulting in a decreased number of intracellular cavities, hereby lowering the NIR reflectance. The translocation of nutrients and pigments to the stem, will result in a higher VIS reflectance. Dehydrated leaves can be detected by less extreme water absorption bands. When the dehydration continues a chlorophyll and structural breakdown can follow (Jones & Vaughan, 2010).

2.4.3 Object Based Image Analysis

Image classification is a method used to quantify discrete or categorical indicators of land cover features. Three broad classification techniques exist: pixel-based, sub-pixel-based and object-based classification (Jones & Vaughan, 2010). Sub-pixel classification methods are needed for low resolution images where the pixels are significantly larger than the objects you want to classify. For medium resolution images where the pixels and objects size are of the same order, pixel-based classification methods are appropriate. High resolution images, where the pixels are significantly smaller than the objects you want to classify require an object-based classification methods (Blaschke, 2010). Because an object-based classification will be used in this thesis, we further focus on this classification method.

An object-based image analysis (OBIA) uses both the signatures of the individual pixels and the spatial measurements to characterize the shape of a region. OBIA follows a two-step process involving (1) the segmentation of the imagery into discrete objects based on spectral and shape (dis)similarities, followed by (2) the classification of those objects using a supervised classifier (Blaschke, 2010).

2.4.3.1 Criteria for image segmentation

The image segmentation algorithm will divide the image into relatively homogeneous and semantically significant groups of pixels. Using this method will help overcome the problem of salt and pepper images often acquired through common pixel-based classification methods (Blaschke, 2010; Myint et al., 2014).

A multi-resolution segmentation (MRS) algorithm is a good first step to delineate the objects' boundaries (Myint et al., 2014; Yan et al., 2018). MRS is a bottom-up segmentation, starting

with one-pixel objects, that consecutively merges pixels or existing image objects into bigger objects based on a relative heterogeneity criterion (Benz et al., 2004; Yan et al., 2018). In each step, those pixels or image objects are merged which give the smallest growth in heterogeneity (Benz et al., 2004).

This heterogeneity is controlled by three key parameters: scale, shape and colour. The scale parameter is the stop criterium for the segmentation process. If the resulting increase in heterogeneity exceeds the threshold value set by the scale parameter, no fusion takes place. Larger scale parameters will result in larger objects. The shape and colour criteria are part of the general segmentation function shown below.

$$S_f = w_{colour} \cdot h_{colour} + w_{shape} \cdot h_{shape}$$

$$where\ w_{colour} + w_{shape} = 1\ and\ w_{colour}, w_{shape} \in [0,1]$$

The weight parameters allow the user to place greater emphasis on the spectral characteristics (w_{colour}) or the spatial characteristics (w_{shape}). The spectral heterogeneity (h_{colour}) is related to the pixel value while the shape heterogeneity (h_{shape}) describes the smoothness and compactness of an image object (Benz et al., 2004).

2.4.3.2 Classifiers for object classification

The objects created in step 1 are classified using supervised classification algorithms. Supervised classification starts from a training dataset, consisting of areas or pixels that are known to be representative for a certain land cover type. From these training areas spectral signatures are distracted, which are used by a supervised classifier to classify the entire image accordingly (Jones & Vaughan, 2010).

Many supervised classifiers, methods used to assign pixels within an image to one of the training classes, can be used. Below some examples are given, ordered from simple easy-understandable classifiers to more complex ones which are hard to interpret.

The *minimum distance to mean* classifier calculates the distances between the centroids of the training classes and an unclassified pixel (or object), this pixel will be assigned to the nearest training class. The *maximum likelihood* classifier uses the training data to calculate means and variances of each training class in order to provide the probability of any pixel belonging to a given class. *Support vector machines (SMV)* in a non-parametric method that makes no

assumptions about the data structures. SMV try to find the best hyperplane within the multidimensional feature space that forms the optimal separation between different training classes. This approach differs from minimum distance or maximum likelihood because only the spectral boundaries of the different classes is taken into account, without looking at the centroids of each class. *Decision tree* classifiers are the mostly used supervised classifiers which use a series of binary decisions to classify a pixel into a certain class. Lastly, a *random forest* (RF) model consists of a large collection of uncorrelated decision trees, which are fit on different subsets of the data (Jones & Vaughan, 2010).

2.5 Landscape metrics

The composition and configuration of the urban green infrastructure in Leuven will be assessed using multiple landscape metrics. The usage of landscape metrics became very common by the end of the 1980s within the field of landscape ecology and they are mostly defined as indexes developed to quantitatively describe landscape patterns. Landscape metrics can be divided into several groups based on their spatial characteristics and patterns they measure or based on the level (patch, class or landscape) for which they are calculated (McGarigal et al., 2002; Uuemaa et al., 2009; Van Eetvelde, 2007).

The most complete set of landscape metrics are gathered by FRAGSTAT, the program that will be used for this analysis. The first group defined by FRAGSTAT consists of *area/density/edge metrics*, which describe the number and size of patches in combination with the amount of edge created by these patches. The *diversity metrics* tell something about the diversity within the landscape, important components are *richness* and *evenness.* The two groups mentioned above are composition metrics (McGarigal et al., 2002; Van Eetvelde, 2007).

A third group composes the *shape metrics* which describe the shape and complexity of the patches, often describe by the circumference-area ratio. *Core metrics* are defined by the core area of a patch, which is the area inside a patch not influenced by the edge-effects. *Isolation/proximity metrics* describe the spatial and temporal context of the patches rather than their spatial character. They mostly focus on the degree of fragmentation. A fifth group includes the *contrast metrics* which describe the contrast between neighboring patches, these contrasts will influence the edge effects. *Contagion/interspersion metrics* both describe the landscape texture and are indicators for the adjacency of patches. Contagion describes the spatial

distribution and intermixing of patches while interspersion focuses on the level of variation of patches within the landscape. Lastly, *connectivity metrics* reflect the degree of interconnectedness between different patch types. Both physical and ecological connectivity can be calculated. The metrics described in this paragraph are configuration metrics (McGarigal et al., 2002; Van Eetvelde, 2007).

3 Materials and methods

3.1 Study area

3.1.1 Location

The municipality of Leuven (50°52'39" N 4°42'16" E) is situated in the province Flemish Brabant in Belgium, located 25 kilometres east of Brussels, the capital of Belgium (figure 3.1). The municipality includes Leuven, Heverlee, Kessel-Lo, Wilsele, Wijgmaal, Korbeek-Lo and Haasrode, covering an area 5663 ha.

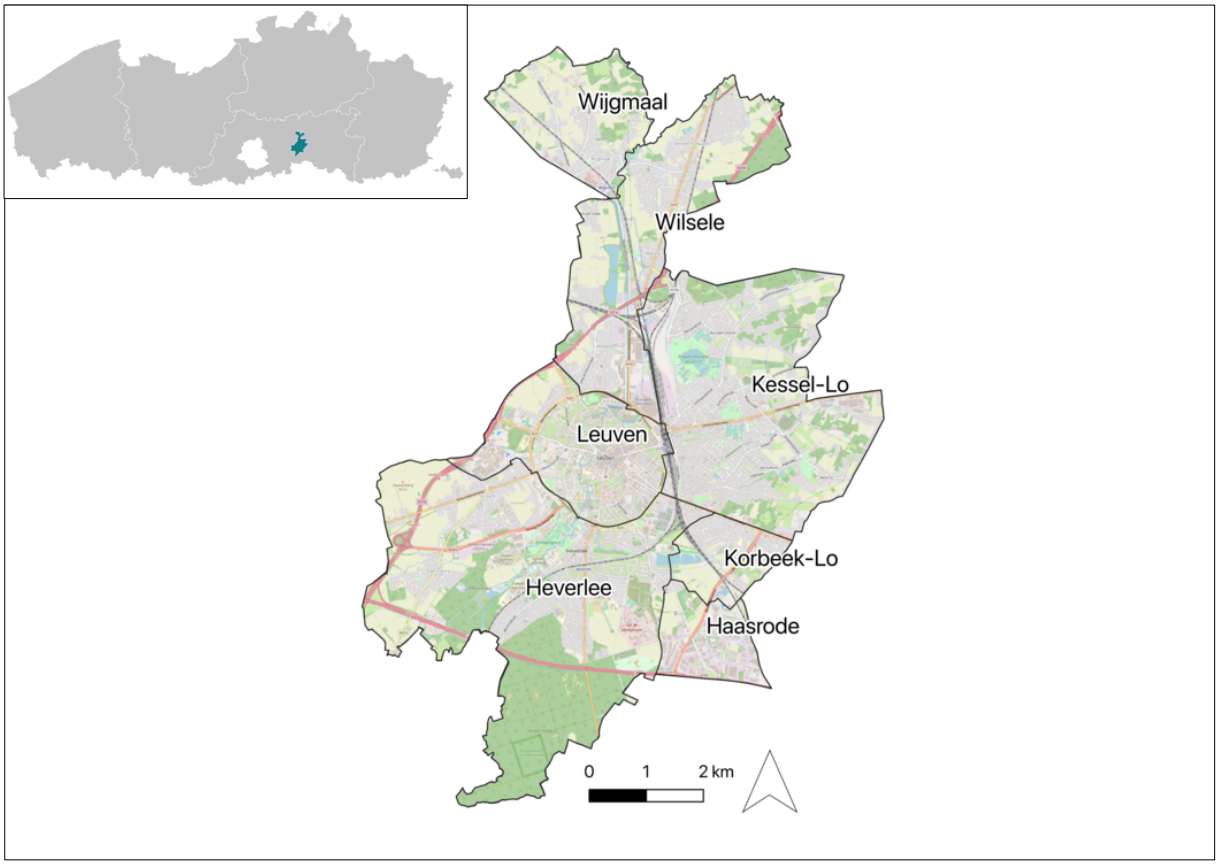

Figure 3.1: Location of the study area. Upper left corner: map of Flanders with location of Brussels (white) and Leuven (blue) highlighted. Right: Detailed map of the municipality of Leuven. Edited from shapefiles obtained from Agentschap Informatie Vlaanderen (2019) and Stad Leuven (2018).

3.1.2 Climate

Since Belgium is a small country almost no variation in climate is seen across different regions. The Köppen Climate Classification describes the climate of Belgium as a warm temperate climate with no dry season and a warm summer (Cfb). Figure 3.2 shows that the mean annual temperature equals to 9.8°C and the mean annual precipitation amounts to 821 mm, also the mean monthly precipitation and temperatures are presented (KMI, 2019).

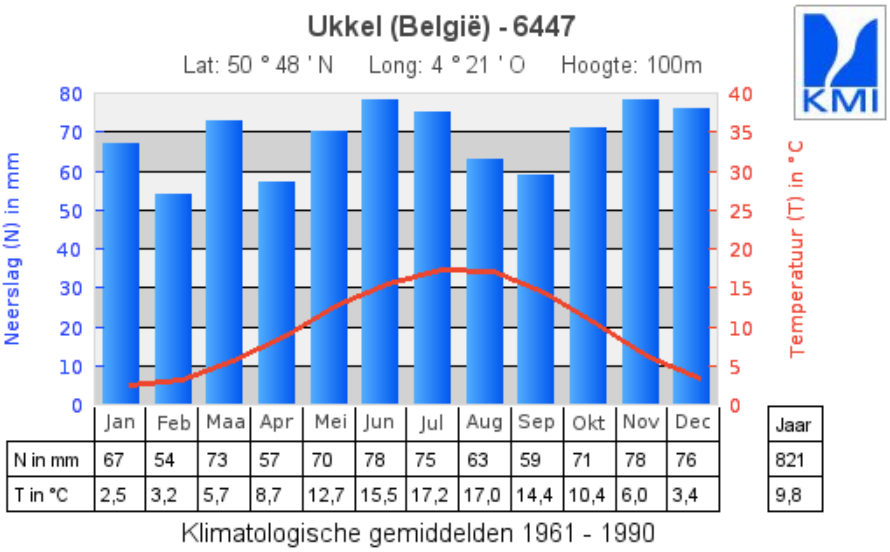

	Jan	Feb	Maa	Apr	Mei	Jun	Jul	Aug	Sep	Okt	Nov	Dec	Jaar
N in mm	67	54	73	57	70	78	75	63	59	71	78	76	821
T in °C	2,5	3,2	5,7	8,7	12,7	15,5	17,2	17,0	14,4	10,4	6,0	3,4	9,8

Figure 3.2 Climatological data from official station in Uccle (Belgium). The graph shows the mean monthly precipitation in mm (left) and the mean monthly temperature in °C (right) over the time period 1961-1990. Also the mean annual precipitation and temperature are presented (KMI, 2019).

3.1.3 Urbanization

The total population in the municipality of Leuven has grown from 84.857 in 1990 to 101.702 in 2020. This population growth is mostly explained by a population increase in sub-municipalities Leuven and Kessel-Lo, equal to an increase of 7184 and 7039 people respectively. The highest increase in population occurred between 2000 and 2010. During this period also the population density of Leuven has increased from 1.498 inhabitants/km^2 in 1990 to 1.796 inhabitants/km^2 in 2019. The sub-municipality Leuven knows the highest increase from 4.115 inhabitants/km^2 to 5.360 inhabitants/km^2 over the same time period. In 2019, Kessel-Lo has a population density of 2.187 inhabitants/km^2, followed by Wilsele and Heverlee with 1.101 and 1.088 inhabitants/km^2 respectively. Wijgmaal has the lowest population density, equal to 838 inhabitants/km^2 (Bevolkingsregister Stad Leuven, 2020).

3.2 Data collection

3.2.1 Sampling design

Weather stations are installed in both private gardens and (semi-)public locations according to a stratified sampling design. The stratification is based on the concept of Local Climate Zones (LCZ). This Local Climate Zone classification was originally used as an objective protocol for measuring UHI intensity and thus captures important urban morphological characteristics (Verdonck et al., 2018). Stewart & Oke (2012) formally define these zones as "regions of uniform surface cover, structure, material, and human activity that span hundreds of meters to several kilometers in horizontal scale".

In practice the LCZs are separated based on (i) building height, (ii) building density and (iii) vegetation cover. Using airborne LiDAR data and high-resolution Pleiades satellite imagery (for technical details of the remote sensing data see section 3.2.3.2) we could calculate the building height, building density and vegetation cover for each 100x100m grid cell within our study area and assign a LCZ class to each location in Leuven according the Steward & Oke (2012) LCZ typology (figure 3.3). By setting threshold values, two building height classes, two building density classes and three vegetation cover classes were obtained, ultimately resulting in 12 LCZ classes. The criteria for each of these parameters can be found in table 3.1. The aim is to divide the weather stations equally among these land cover classes.

Table 3.1 The criteria for the parameters building height, building density and vegetation cover in combination with related LCZ class ID.

Building height	Building density	Vegetation cover	LCZ class ID
High building [> 8 m]	High density [> 25%]	High vegetation cover [> 67 %]	111
		Medium vegetation cover [> 34 %]	112
		Low vegetation cover [< 34 %]	113
	Low density [< 25%]	High vegetation cover [> 67 %]	121
		Medium vegetation cover [> 34 %]	122
		Low vegetation cover [< 34 %]	123
Low building [< 8 m]	High density [> 25%]	High vegetation cover [> 67 %]	211
		Medium vegetation cover [> 34 %]	212
		Low vegetation cover [< 34 %]	213
	Low density [< 25%]	High vegetation cover [> 67 %]	221
		Medium vegetation cover [> 34 %]	222
		Low vegetation cover [< 34 %]	223

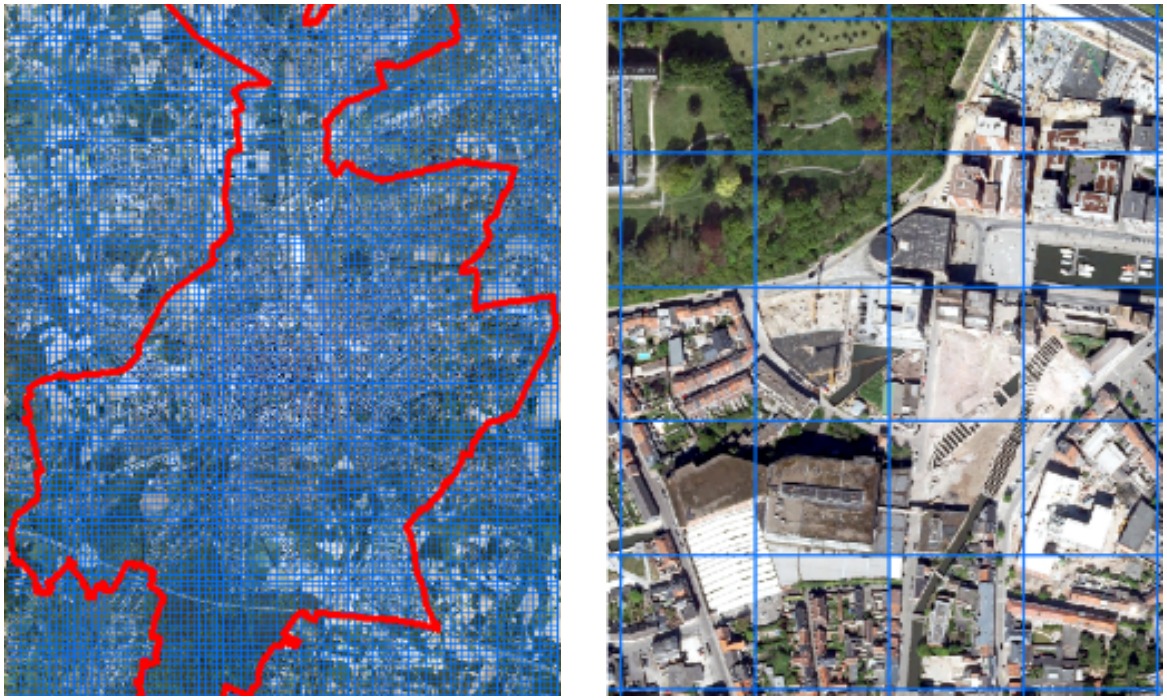

Figure 3.3: The 100x100 m grid layer shown above a satellite image of Leuven, used to derive the LCZ class IDs.

Through articles in local newspapers (Putseys, 2019b, 2019a) published in June 2019 and online (social) media platforms (Leuven 2030, 2019; ROB-TV, 2019), citizens of Leuven were invited to participate in this research. We were looking for inhabitants willing to open their gardens for (1) an inventory of the composition of their garden and/or (2) the installation of a small low-cost weather station inside their garden. The LCZ classification, explained above, was used to select the most optimal locations. In collaboration with the city of Leuven and Leuven 2030, additional semi-public locations were selected. The aim was to obtain a good spatial distribution of the weather stations and equal representation of all possible LCZ classes.

The search for suitable locations followed the following procedure: (1) possible suitable locations were identified based on their class ID and spatial distribution, (2) these sites were further examined using satellite imagery from Google Maps, gardens with an open exposure were marked, (3) the marked locations were visited, where their suitability could be assessed in the field and lastly (4) permission from the owners for installation was asked.

3.2.2 Urban air temperature (UAT)

The urban temperatures are measured using low-cost internet weather stations developed by Renkforce©, the Renkforce WH2600 wireless digital weather station to be precise (figure 3.4). The specifications of this station can be found in appendix 8.1 (Renkforce, n.d.).

The weather station consists of an indoor (WH25) and outdoor unit (WH24) measuring indoor and outdoor temperature, indoor and outdoor humidity, (indoor) air pressure, precipitation, wind speed, wind direction, solar radiation and UV every 16 seconds, respectively. Both units transmit their measured data wirelessly, through radiofrequency, to a base station. This base station must be connected to a router and subsequently sends its data to a server via a LAN-connection. The data is later visualized using the Weather Observations Website - Belgium (WOW-BE), a crowdsourcing platform from the RMI (Royal Meteorological Institute). The outdoor unit contains three rechargeable batteries that are recharged by a solar panel. The temperature and humidity sensors are protected by a radiation shield that serves as protection to extreme weather conditions and prevents the direct exposure to solar radiation by allowing surrounding air to ventilate through (Conrad, 2019; Renkforce, n.d.).

Figure 3.4: Renkforce WH2600 wireless digital weather station. From left to right: outdoor unit, base station and indoor unit (Conrad, 2019).

In private gardens the weather stations with dimensions 20x40 cm were installed at a height of 2 meters, using a 2.70 m steel pole which was anchored in the soil to a depth of 70 cm. To make sure the pole would stay perfectly vertical some dry concrete was added. Within the gardens the stations were preferably placed on an open location, at least 1 meter from interfering object, such as walls and trees (figure 3.5 left). Following the station's guidelines, the solar panel was directed towards the south to maximize the amount of solar radiation that can be captured and to obtain correct measurements of wind direction.

Figure 3.5: Example of installed weather stations in a private garden (left) and a semi-public playground (right).

The weather stations installed on a (semi-)public terrain could not follow the same procedure as explained above. In most cases stations were installed on available light poles using specially designed L-structures to avoid direct effect contact with the pole. For security reasons an installation height between 3-4 meters was used (figure 3.5 right).

3.2.3 Urban green infrastructure (UGI)

3.2.3.1 Inventory data

During the scouting of possible suitable locations for the installation of a weather station, 183 inventories were performed. Using Google Maps satellite images as a reference, a map of each garden was drawn on which the composition of its vegetation, impervious surfaces and water features were identified using a classification code presented in appendix 8.2. When possible, tree species were identified. These hand-drawn maps were digitalized in QGIS (version 3.2) (QGIS Development Team, 2019) using recent winter and summer orthophotos as a reference, obtained from Geopunt. The inventory data will be used to get more insight into the composition of the green infrastructure in Leuven and to verify the green map obtained from satellite imagery during an accuracy assessment.

3.2.3.2 Remote sensing data

Urban green is highly heterogeneous and hard to classify using low or medium resolution images. In this thesis we will use a combination of the methodologies proposed by Degerickx

et al. (2018) and Yan et al. (2018), in which high resolution satellite imagery is combined with airborne LiDAR data to precisely classify the urban landscape.

The high resolution Pleiades satellite image has a panchromatic band with a spatial resolution of 0.5m and has 4 multispectral bands (blue, green, red and NIR) with a spatial resolution of 2m (table 3.2) (Airbus Defence & Space Intelligence, 2013). The Pleiades image was acquired on April 7th, 2019. The goal was to acquire new images over the summer of 2019 but due to suboptimal weather conditions all attempts were rejected.

Table 3.2: The spectral and spatial resolution of the Pléiades imagery.

Spectral band	Wavelength	Spatial resolution
Blue	430 – 550 nm	2 m
Green	500 – 620 nm	2 m
Red	590 – 710 nm	2 m
NIR	740 – 940 nm	2 m
Pan	470 – 830 nm	0.5 m

The Pléiades mission is a combination of two sun-synchronous satellites, Pléiades 1A and 1B, operating in the same orbit, phased at 180° from each other. The Pléiades 1A was launched on December 16, 2011 from the European spaceport in French Guinea, its twin brother Pléiades 1B was launched almost 1 year later on December 2, 2012. The combined use of both satellites ensures daily revisits to any location on earth (Airbus Defence & Space Intelligence, 2013, 2019; Astrium, 2012).

The optical imagery are orthographic calibration-ready standard products obtained under cloudless conditions (cloud cover < 5%). A series of preprocessing steps, including internal sensor geometry correction, removal of optical distortions, scan distortions and line-rate variations, and band registration, were performed by the vendor (Airbus Defence & Space Intelligence). Afterwards we applied the Gramm-Schmidt (GS) algorithm (Laben & Brower, 1998) in ENVI 5.3 to pan-sharpening the multispectral bands, this GS algorithm produces better spectral quality, while maintaining the original spectrum of imagery (Yuhendra et al., 2012).

The airborne LiDAR dataset used in this thesis was collected in the summer of 2015 by Aerodata Surveys Nederland BV (GeoBusiness Nederland, 2016) and has an average point density of 15 points/m^2. The LiDAR data is used to derive a canopy height model (CHM; height of objects to ground surface) which enables us to identify the height and 3-dimensional structure

of urban green. The processing procedure, explained in Degerickx et al. (2018), include the detection and removal of noisy returns, the detection of ground returns, the creation of a DTM through interpolation, the derivation of all non-ground returns and lastly the creation of a CHM by extracting the maximum height for each cell.

3.2.3.3 Green map of Flanders

Because the extent of the used image does not cover the entire study area, the green map of Flanders (2015) was used to get info on urban green's composition and configuration for the 12 weather stations located outside the imagery extent. The green map of Flanders has a resolution of 1m and divides the landscape into four landcover classes; high green, low green, agriculture and others. For our purpose we only used high and low green (Agentschap voor Natuur en Bos, 2013).

3.3 Data analysis

3.3.1 Urban air temperature (UAT)

All data analysis regarding urban air temperatures are performed using RStudio version 1.1.463 (RStudio Team, 2016).

3.3.1.1 Data quality analysis

Because the observations are made using low cost digital weather station, a data quality analysis should be performed before the data can be used to draw any conclusions.

To this end, four low-cost WH2600 digital weather station were installed next to the official and more professional equipment of the RMI in both Uccle and Diepenbeek. Since these stations will serve as a reference, they were defined as GarmonR01, GarmonR02, GarmonR03 and GarmonR04. The specifics of each station can be found in table 3.3. A simple comparison between GarmonR01 and GarmonR02 is included in the appendix 8.3 (figure 8.1 and 8.2).

Table 3.3: The characteristics of the four reference station placed in the near vicinity of the official stations from the RMI.

Name	Location	Installation date
GarmonR01	Uccle	10/09/2018
GarmonR02	Uccle	02/09/2019
GarmonR03	Diepenbeek	06/11/2019
GarmonR04	Diepenbeek	06/11/2019

By identifying the climatic variables mostly correlated with the temperature bias between our low-cost reference stations and the official RMI station in Uccle, a predictor for temperature bias is created. This prediction model can then be applied to the whole weather station network in Leuven, hereby calculating corrected temperatures for each station in function of its local climatic conditions.

During the search for a predictor model, the dataset was split in training (0.60) and test (0.40) data. The training data was used to train simple regression models, multiple regression models and a random forest model. Because a previous study by Bell et al. (2015) already suggested that both radiation and windspeed were highly correlated with the temperature bias, we mostly focussed on these variables. This previous research also learned us that taking past radiation measurements into account, using an exponential weighting, can further improve this correlation, resulting in an advanced correction model (Bell et al., 2015). The potential predictor models are validated using the test data. The resulting coefficient of determination (R^2) and root mean square error (RMSE) help us decide the most optimal prediction model for the temperature bias.

To ensure that the predictor bias model, designed for Uccle, is applicable for stations located on a different location, two extra stations in Diepenbeek were installed. Using the predictor bias model, corrected temperatures for these stations will be calculated and can subsequently be compared to the official RMI station located in Diepenbeek.

3.3.1.2 Spatio-temporal maps of Leuven's UHI

The summer and winter UHI in Leuven will be characterized on different temporal scales and with the help of different quantitative variables.

Because the weather stations were continuously installed during the summer of 2019 and not all stations record and send their observations flawlessly to the server, we were forced to look at small temporal scales, making sure that only stations continuously recording during these timeframes were taken into account. To accomplish this, a gap analysis was performed for each temporal scale separately in which stations that did not record any measurement for at least 30 minutes were removed. For the summer UHI, the temporal scales include (1) one extreme heatwave day, (2) a complete heatwave week and (3) the five hottest days during the measuring

period. All these temporal scales are split up in night- (radiation ≤ 0) and daytime (radiation > 0) ranging from 00h00 until 05h50 and 06h00 until 18h00 respectively. For the winter UHI we looked at (a) one morning following an extreme clear night with a mean cloud cover percentage equal to 0 % and (b) five mornings following the five most extreme clear nights of the measuring period with a mean cloud cover below 25 %. These morning timeframes range from 04h until 09h. We expected to see the same patterns for the different temporal scales. If this was not the case, the observed patterns could be incidental rather than suggesting a general pattern.

For the summer UHI, the quantitative variables include (1) absolute minimum temperatures during night-time, (2) absolute maximum temperatures during daytime, (3) changing temperature differences during night and day and (4) lastly the Thom's discomfort index for both night- and daytime. For the winter UHI, we will calculate both (a) minimum temperatures and (b) changing temperature differences during early mornings.

The minimum temperatures are a good way to visualize the UHI since they focus on the fact that urban environments are characterized by a reduced longwave radiation loss during night-time (Bassett et al., 2016).The changing temperature differences are calculated as the difference between the temperature of a specific station and the mean temperature of all stations for every timestep (ever 10 minutes) and show over which timeframes the highest temperature differences occur. To compare this changing temperature difference for all stations, we summed these differences over all timesteps and divided this sum by the number of timesteps. Hereby you obtain a mean temperature difference between a specific station and the mean of all stations. Stations having a negative value will be cooler than the mean station, while stations obtaining a positive value will generally be hotter than the mean station. The Thom's discomfort, based on both mean temperature and mean humidity measurements, gives more insight into the thermal discomfort people encounter within the city centre. Thom's discomfort index is calculated using the following formula. The discomfort index values and their discomfort feeling scale are expressed in table 3.4 (Georgi & Zafiriadis, 2006).

$$DI = TEM - 0.55(1 - 0.01\,HUM)(TEM - 14.5)\ °C$$
$$where\ DI = discomfort\ index\ [°C], TEM = airtemperature\ [°C],$$
$$HUM = relative\ humidity\ [\%]$$

Table 3.4: Discomfort index (DI) values and their relative discomfort feeling scale (Georgi & Zafiriadis, 2006).

Feeling of discomfort	DI [°C]
No discomfort	< 21
Discomfort expressed by < 50% of the population	21 -24
Discomfort expressed by > 50% of the population	24 - 27
Discomfort expressed by the majority of the population	27 - 29
Discomfort expressed by all	29 - 32
Stages of medical alarm	> 32

The calculation of minimum temperatures for one day is straightforward. When this variable is calculated for an entire week or combination of days, we first calculated the minimum temperature for each day, afterwards the mean of these minimum temperatures is calculated. For only one night or morning, the changing temperature difference is calculated as a difference between the mean night/morning temperature of all stations and the night/morning temperature of a specific station. For an entire week or combination of days, first the mean temperatures over these timeframes are calculated, after which a difference between both is made. The Thom's discomfort index is simply calculated using mean temperature and humidity over one night, week or combination of days. These temperature and relative humidity variables are presented on a map of Leuven and its surrounding sub-municipalities. The background cover represents a 1m resolution landcover image acquired from Geopunt (Agentschap Informatie Vlaanderen, 2019a).

3.3.2 Urban green infrastructure (UGI)

3.3.2.1 Object-based image analysis (OBIA)

In section 2.3.3 we stated that an OBIA uses both the signatures of the individual pixels and the spatial measurements to characterize the shape of a region. OBIA follows a two-step process involving (1) the segmentation of the imagery into discrete objects based on spectral and shape (dis)similarities, followed by (2) the classification of those objects. Here we will use OBIA to classify the urban green infrastructure into two classes: high and low green. This process is performed by dr. Jingli Yan (Division Forest, Nature & Landscape, KU Leuven) using the eCognition Developer 9.0 software.

During the (1) image segmentation process we applied a multi-resolution segmentation (MRS) algorithm, which is embedded in eCognition Developer. MRS is a bottom-up segmentation, starting with one-pixel objects, that consecutively merges pixels or existing image objects into

bigger objects based on a relative heterogeneity criterion (Benz et al., 2004; Yan et al., 2018). In each step, those pixels or image objects are merged which give the smallest growth in heterogeneity (Benz et al., 2004). This heterogeneity is controlled by three key parameters: scale, shape and colour. The scale parameter is the stop criterium for the segmentation process. Because visual inspection of this scale parameter is subjective, we used an automated process created by Drăguţ et al. (2014); estimation of scale parameter (ESP). The ESP automatically segments the image using fixed increments of the scale parameter. For each object level obtained though segmentation, ESP calculates the Local Variance (LV) as the mean Standard Deviation (SD) of the objects. The dynamics of LV are assessed using a measure called Rate of Change (ROC). The peaks in the ROC-LV graph (figure 3.6) indicate the object level at which the image can be segmented in the most appropriate manner (Drăguţ et al., 2014). The values for shape and color determine the weight placed on these parameters when generating segmented objects. A relatively small value is generally recommended for shape (Zhou et al., 2009) so that more weight can be put on color and spectrum. Finally, we generated an object layer using optimal scale parameters as suggested by ESP (25, 55) and assigning a higher weight to the color parameter (0.9) than the shape parameter (0.1). An equal weight was given to compactness and smoothness (0.05), two subsets of shape.

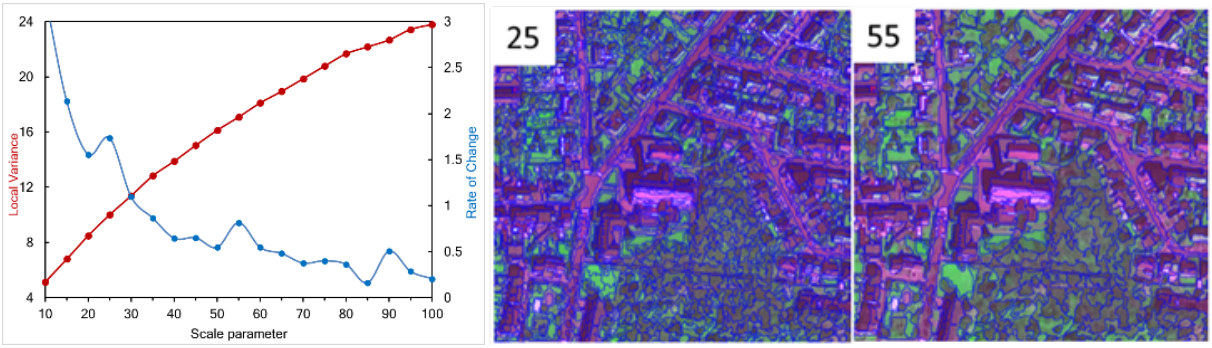

Figure 3.6: The ROC-LV graph (left) and segmented examples using the scale parameters indicated by ESP.

After establishing the image objects, (2) these objects are classified using a rule-set approach. First, we separated spectrally and texturally different shaded and unshaded objects using thresholds for mean brightness and mean red. Next, vegetated objects, indicated by NDVI and mean blue, were extracted from unshaded objects (see table 3.5). Subsequently high and low green were separated from unshaded vegetation by average height of vegetated objects (CHM). The vegetated objects higher than 3m were classified as high green, other objects as low green. For shaded areas, we first separated shadow objects into tree shadow (shadow caused by trees) and building shadow (shadow caused by buildings). This was necessary because the two types of shadow are too distinct in spectrum and shape characteristics to apply the same thresholds

for identifying shaded greenspace, e.g. building shadows are generally much darker and bigger than tree shadows. Therefore, the shaded objects with an area greater than 400 pixels (100 m^2) and brightness lower than 24 were classified into building shadows, the others were classified as tree shadows. Additionally, the more boundaries of an object shared with greenspace, the higher possibility of the object belonging to greenspace. Then shaded greenspace was extracted from the two shadow types with a combinative use of NDVI (0.11 for tree shadow, 0.08 for building shadow), brightness (24) and relative border to greenspace (0.5). Afterwards the shaded greenspace was separated into two green functional types using the same features (3m of CHM) as for unshaded vegetation.

Table 3.5: Features and threshold values used during the classification.

Class name (object level)	Feature (threshold)	Class name (object level)	Feature (threshold)
Unshaded area (25)	Brightness (33); Mean Red (372)	Shaded area (25)	Brightness (33); Mean Red (372)
-	-	Tree + building shadow (55)	Area (100 m^2); Brightness (24); Relative border to green (0.5)
Unshaded green (25)	NDVI (0.22); Mean Blue (435)	Shaded green (55)	NDVI (0.11) in tree shadow; NDVI (0.08) in building shadow
High & Low green (55)	CHM (3m)	High & Low green (55)	CHM (3m)

3.3.2.2 Accuracy assessment

We randomly collected more than 3900 ground samples from 30 plots of 100x100 m^2 in public space in 2015, additionally 183 private gardens throughout the Leuven city were collected in 2019 for the classifier training and classification validations. After the field campaigns, all the plots and gardens were digitalized to land cover patches (3916 patches) based on the 25 cm spatial resolution orthophotos mentioned in section 3.2.3. For classification validations, we first removed the digitalized patches used or partially used as training samples (1500 patches), then we converted all the left patches into points (2416 points). The majority of samples locate in central region of Leuven city, which leads to an aggregation of validation samples in central Leuven. In addition, 800 validation points are enough considering the size of the study area. Next, we divided the points in terms of classified land cover classes and stratified selected one of three points for each classified class. Finally, we obtained 800 validation points to generate the confusion matrixes in ERDAS Image 2020 (Hexagon, 2020).

Accuracy parameters used to validate the accuracy of the image include the overall accuracy, producer's accuracy, user's accuracy and kappa head and can be computed from the confusion matrix (Stehman & Wickham, 2011). The overall accuracy is the overall proportion of pixels classified correctly (Stehman, 1997). User's accuracy for a cover type *i* is the probability that a pixel classified as category *i* by the map is classified as category *i* by the reference data. Producer's accuracy for a cover type *j* is the conditional probability that a pixel classified as category *j* by the reference data is classified as category *j* by the map. The kappa head tells how accurate the map is in comparison with a total random map (Stehman, 1997).

3.3.2.3 Describing the spatial patterns of Leuven's UGI using landscape metrics

The composition and configuration of the urban green infrastructure in Leuven will be assessed using multiple landscape metrics. The composition refers to the abundance and variability of urban green, while the configuration refers to the spatial arrangement or distribution of urban green (Zhou et al., 2011).

The most complete set of landscape metrics is gathered by FRAGSTAT, the program that will be used for this analysis (McGarigal et al., 2002). During this analysis we will neglect the non-urban green landscape classes and focus on both low and high green within Leuven. Percentage cover (PLAND) will be calculated for each urban green class to quantify the effect of urban's green composition. To assess the effect of urban green's configuration multiple configuration metrics of the UGI are calculated; largest patch index (LPI), patch density (PD), edge density (ED), mean patch size (AREA_MN) and mean shape index (SHAPE_MN). The definition and equation of these landscape metrics are listed in table 3.6 (McGarigal et al., 2002). Previous studies have shown that these metrics could potentially affect urban air temperatures (Fan et al., 2015; Xiao et al., 2018; Zhou et al., 2011, 2017).

Table 3.6: The landscape metrics used in this analysis (McGarigal et al., 2002).

Metrics	Description [units]	Equation
Percentage cover (PLAND)	sum of the areas (m^2) of all patches of the corresponding patch type i, divided by total landscape area (m^2), multiplied by 100 (to convert to a percentage) [%]	$\frac{100}{A} x \sum_{j=1}^{n} a_{ij}$

Largest patch index (LPI)	the area (m^2) of the largest patch of the corresponding patch type i divided by total landscape area (m^2), multiplied by 100 (to convert to a percentage) [%]	$\frac{\mathrm{Max}(a_i)}{A} x\ 100$
Patch density (PD)	the number of patches of the corresponding patch type i divided by total landscape area (m^2), multiplied by 10,000 and 100 (to convert to 100 hectares) [n/100ha]	$\frac{n_i}{A} x\ 10^6$
Edge density (ED)	sum of the lengths (m) of all edge segments involving the corresponding patch type, divided by the total landscape area (m^2), multiplied by 10,000 (to convert to hectares) [m/ha]	$\frac{10000}{A} x \sum_{k=1}^{n} e_{ik}$
Mean patch size (AREA_MN)	mean value of the area, which equals the area (m^2) of the patch, divided by 10,000 (to convert to hectares) [ha]	$\frac{1}{10000\ x\ n} x \sum_{j=1}^{n} a_{ij}$
Mean shape index (SHAPE_MN)	mean value of the shape index, which equals patch perimeter (m) divided by the square root of patch area (m^2), adjusted by a constant to adjust for a square standard. [-]	$\frac{1}{n} x \sum_{j=1}^{n} \frac{0.25 x e_{ik}}{\sqrt{a_{ij}}}$

a_{ij} = area of patch ij, e_{ik}= total length of edge in landscape involving patch type i, A = total landscape area [m^2], n = number of patches in the landscape of patch type i

3.3.3 Relationship between UAT and UGI

3.3.3.1 Spatial patterns of UGI around weather station

The relationship between urban air temperatures and the urban green infrastructure is examined for different spatial scales. By looking at only the garden, the neighbouring surroundings or the bigger building block the cooling distance of urban green can be assessed. In practice, ten circular buffers around each weather station are drawn with a radius of 10m, 20m, 30m, 50m, 80m, 100m, 130m, 180m, 250m and 500m. Within each of these buffer regions the landscape metrics described in table 3.6 are calculated for each urban green class and each weather station separately.

Each of these buffers can be seen as a landscape of its own, made up of patches of different landcover classes. The landscape metrics used in this thesis are defined as class metrics. Class metrics are computed for every patch type or class within the landscape. A class is defined as a set of patches of the same landcover type within a single buffer. The green map produced in section 3.3.2.1 counts two classes; high green and low green. There are two basic types of

metrics at class level: (1) class metrics that simply calculate the amount and spatial configuration of a certain class (e.g. PLAND, LPI, PD, ED), and (2) class distribution statistics which measure aggregate properties of all the patches belonging to a single class. Here we only use the mean (MN) statistic, which calculates the mean of the patch metrics for the patches that comprises each class (e.g. AREA_MN, SHAPE_MN).

3.3.3.2 The weather station's micro-environment

Because we believe that not only urban green but also the station's micro-environment will influence the air temperatures, the statistical analyses described below are used to find a relationship between the air temperatures and both the landscape metrices of urban green and the station's environment. The four environmental variables, used to describe the station's micro-environment, are explained below.

Firstly, the station's environment is characterized by the garden's or public space's (1) enclosure, quantified using the sky view factor (SVF). The SVF is defined as the fraction of visible sky from the ground and equals a number between 0 and 1. An increased height and density of buildings will decrease the SVF, resulting in a number close to zero. An open lawn on the other hand has a high SVF, quantified by a number close to one. This SVF is calculated using LiDAR data described in section 3.2.3.2 and the *Sky view factor SAGA tool* in QGIS (Conrad, 2008). Following the recommendations of Dirksen et al. (2019), we used a maximum search distance of 100m and set the number of search directions equal to 16. The number of directions (or sky hemisphere sectors) equals the number of sectors in which the sky hemisphere is divided for calculation purposes. When the number of search directions is too low, not all obstacles will be detected, the same is true for the search distance (Dirksen et al., 2019).

Also the garden's or public space's (2) area and (3) perimeter are included, these values are derived from the inventory data described in section 3.2.3.1. Lastly the garden's or public space's (4) compactness is used to describe the station's micro-environment. The compactness is calculated using the Polsby-Popper (PP) measure which computes the ratio of the area of the garden/public space (A) to the area of a circle whose circumference is equal to the perimeter of the garden/public space (P) (Polsby & Popper, 1991). The formula of the PP measure is given below.

$$PP = 4\pi \frac{A}{P^2}$$

A Polsby-Popper score falls within the range of [0,1], here a score closer to 1 indicates a more compact garden/public space.

3.3.3.3 Correlation matrix

A Pearson correlation matrix is calculated to examine the strength of the bivariate associations between urban air temperatures/discomfort indexes and both the variables of composition and configuration of the urban green classes within each of the buffers and the station's environment.

The Pearson correlation test, also known as a parametric correlation test, can be used only when (1) the covariation between the two variables (x, y) is linear and (2) the data from each of the two variables follows a normal distribution. The formula for the Pearson correlation test can be found below.

$$r = \frac{\sum(x - m_x)(y - m_y)}{\sqrt{\sum(x - m_x)^2 \sum(y - m_y)^2}}$$
$$where\ m_x = mean\ of\ x\ variables, m_y = mean\ of\ y\ variables$$

When these assumptions are not met, a non-parametric correlation test (e.g. Spearman rank correlation) should be used. The Spearman rank correlation method computes the correlation between the ranks of the x and y variables. The formula of the Spearman correlation test is given below.

$$rho = \frac{\sum(x' - m_{x'})(y' - m_{y'})}{\sqrt{\sum(x' - m_{x'})^2 \sum(y' - m_{y'})^2}}$$
$$where\ x' = rank(x), m_{x'} = mean\ rank(x), y' = rank(y), m_{y'} = mean\ rank(y)$$

Practically, the correlation coefficients between the minimum temperature, maximum temperature, mean temperature, sum of the temperature difference, discomfort index and the landscape metrics for urban green are calculated for both night and day. Additionally, the correlations between minimum temperature, maximum temperature, mean temperature, sum of the temperature difference, discomfort index and the variables of the station's environment are calculated. Such correlation matrixes are only show for the summer UHI, this because we only have a summer green map created with images acquired during the spring/summer of 2019. Finding correlations between winter temperatures and summer green would not make a lot sense. For the calculation of the correlation matrix we used the R studio package *stats v3.6.2*,

which deletes missing values in pairs rather than deleting all rows of x containing any missing values. The results are plotted using the R studio package *corrplot*.

3.3.3.4 Simple linear regression model

Simple linear regressions are calculated to determine the relationship between urban air temperatures/discomfort indexes and the composition and configuration metrics of high and low green. By calculating these regressions for multiple spatial and temporal scales, we can assess the cooling distance and cooling efficiency of different urban green types for the different temporal scales.

Practically, a simple regression model is computed between the minimum temperature, maximum temperature, mean temperature, sum of the temperature difference, discomfort index and the landscape metrics of low and high green for day and night within each of the 10 buffer zones. For the calculation and presentation of the regression model we used the R studio *ggmisc extension* to the *ggplot2* package.

4 Results

4.1 Sampling design

In total 280 private gardens were made available for our research. Roughly 180 gardens were visited in order to assess their suitability within the field. In 2019, 82 weather stations were installed, the distribution pattern is presented in figure 4.1. The 82 stations are divided among 60 private gardens and 22 (semi-)public terrains. A more detailed overview of the Garmon network can be found in appendix 8.4.

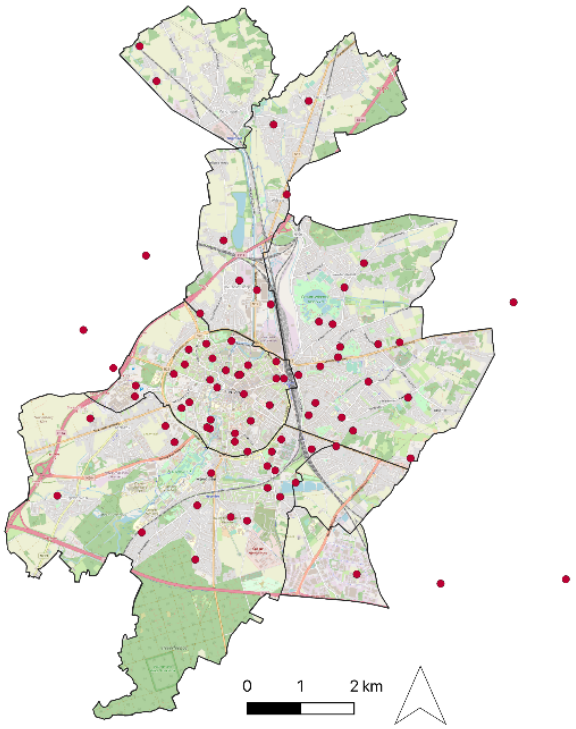

Figure 4.1: Current distribution of the weather stations. Red points represent the installed weather stations.

Table 4.1 shows the distribution of the installed weather stations according to their LCZ class ID. The empty LCZ classes (111, 121, 211) were almost absent within the study area, as a consequence no suitable locations were found.

Table 4.1: Distribution of weather stations among LCZ classes.

LCZ class ID	# of stations	LCZ class ID	# of stations
111	0	211	0
112	8	212	7
113	14	213	8
121	0	221	9
122	13	222	10
123	5	223	8

4.2 Urban air temperature (UAT)

4.2.1 Data quality analysis

4.2.1.1 The temperature bias

The temperature bias between the oldest reference station GarmonR01 and the official RMI station in Uccle is calculated using a 1.5 yearlong dataset for both stations ranging from September 2018 until January 2020. Histograms of this temperature bias are shown in figure 4.2

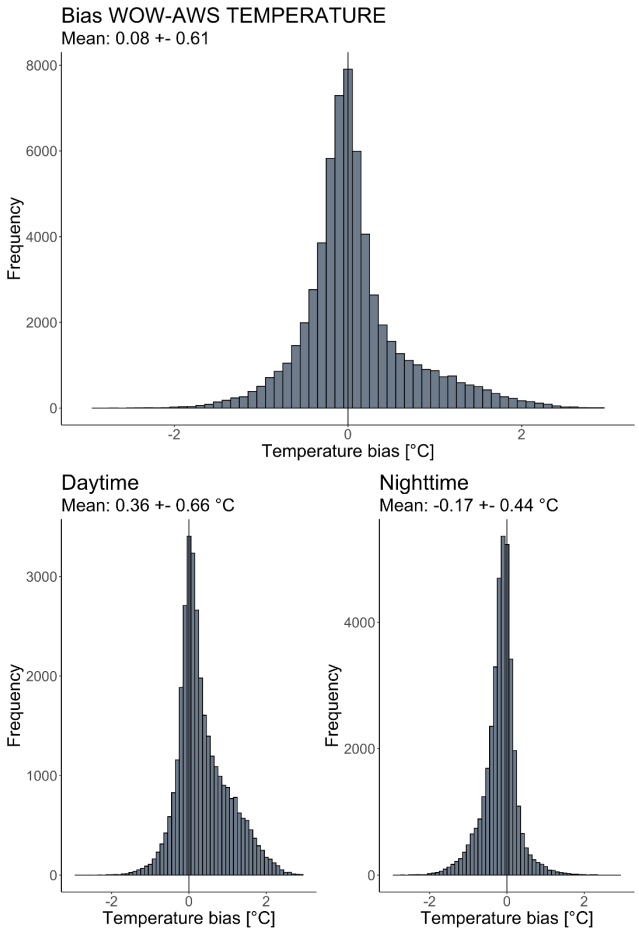

Figure 4.2: Histograms of the temperature bias between reference station GarmonR01 and the official RMI station in Uccle for day and night (top panel), daytime defined by a radiation > 0 (bottom left panel) and nighttime defined by a radiation ≤ 0 (bottom right panel). Mean biases and their standard deviations are given above the graphs.

The temperature bias between the oldest reference station GarmonR01 and the official RMI station in Uccle has a mean value of 0.08°C and a standard deviation of 0.61°C. When this temperature bias is split up for day night, we obtain a positive mean temperature bias during daytime (0.36°C) and a negative mean temperature bias during night-time (-0.17°C). Figure 4.1 also indicates a higher standard deviation during daytime (0.66 °C) than nighttime (0.44 °C).

To better understand the temperature bias, figure 4.3 shows the mean temperature bias in function of month and 'hour of the day'. This figure shows clear diurnal and seasonal patterns and confirms the positive temperature bias during daytime and negative temperature bias during nighttime seen in figure 4.1. In general, we see a positive bias that peaks around midday and is more pronounced during the summer months, lasting for more hours of the day. The night-time temperatures bias is low for all months. It should be mentioned that a temperature bias of 0°C is reached for every month, at which hour of the day this minimal temperature bias occurs, depends on the season.

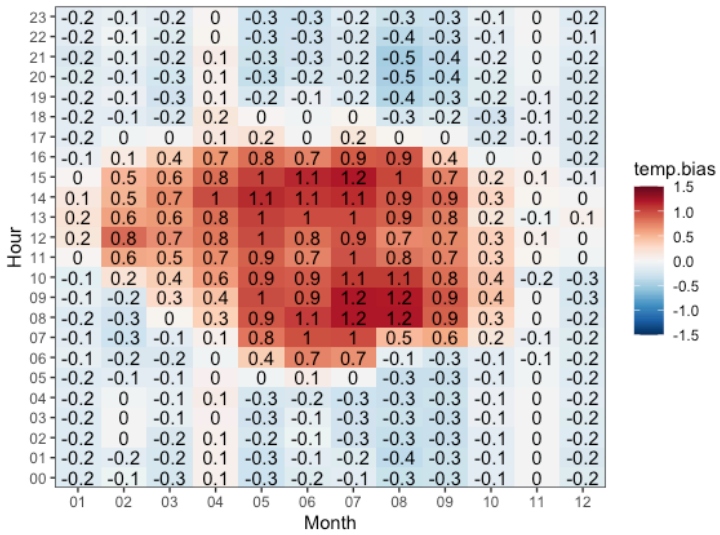

Figure 4.3: The mean temperature bias at different hours of the day (UTC) and months of the year. The values written in each cell are the mean bias of each cell.

Figure 4.4 shows the mean temperature bias in function of windspeed and radiation measured by the GarmonR01 station. The positive temperature bias for high solar radiation increases when the windspeed is low. Related figure 8.4 in the appendix shows the sample size of each cell.

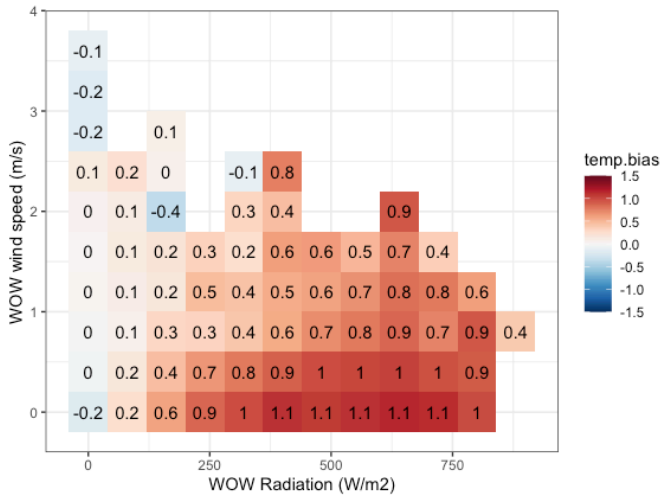

Figure 4.4: The mean temperature bias as function of windspeed and radiation measured by the GarmonR01 station. The values written in each cell are the mean bias of each cell.

4.2.1.2 Building a predictor for the temperature bias

To understand which meteorological observations measured by the low-cost weather station mostly influence the temperature bias, a correlation matrix between this temperature bias and the variables is calculated. This correlation matrix is presented in table 4.2.

Table 4.2: Correlation matrix of temperature bias with meteorological variables measured by the low-cost station.

Temperature [°C]	Dew point temperature [°C]	Humidity [%]	Radiation [W/m^2]	Wind speed [m/s]	Radiation60 [W/m^2]
0.43	0.20	-0.53	0.61	0.09	0.67

The most correlated variable is radiation (0.61) followed by humidity (-0.53), temperature (0.43), dew point temperature (0.20) and wind speed (0.09). Pressure measurements are not included because they were measured inconsistently. When past radiation measurements are taken into account the correlation is further improved, and it reaches a maximum value when considering the last 60 minutes (0.67). We used an exponential weighting, giving a higher importance to the radiation measurements closer to the temperature measurement. This variable is further denoted as Radiation60 (Rad60).

Using these variables, we tried to build a predictor for the temperature bias. For this purpose, multiple models were calibrated in which the temperature bias is described as a function of only one or multiple meteorological variables. Below (table 4.3 and figure 4.5) an overview of only the most promising models is shown. Figure 4.5 shows the uncorrected temperature bias (a) as well as the corrected temperature biases after validation with five different models; a simple linear regression with the past radiation (b), a multiple linear regression with the past radiation and windspeed (c), with the past radiation and humidity (d), with the past radiation, windspeed and humidity (e) and a random forest model including temperature, dew point temperature, humidity, radiation, radiation60, windspeed, month and hour (f). Their coefficient of determination (R^2) and root mean square error (RMSE) are summarized in table 4.3.

Table 4.3: The coefficient of determination (R^2) and root mean square error (RMSE) of the different models.

Model	R^2	RMSE
Rad60 (b)	0.432	0.462
Rad60 & windspeed (c)	0.457	0.451
Rad60 & humidity (d)	0.465	0.448
Rad60 & humidity & windspeed	0.485	0.440
Random forest	0.761	0.286

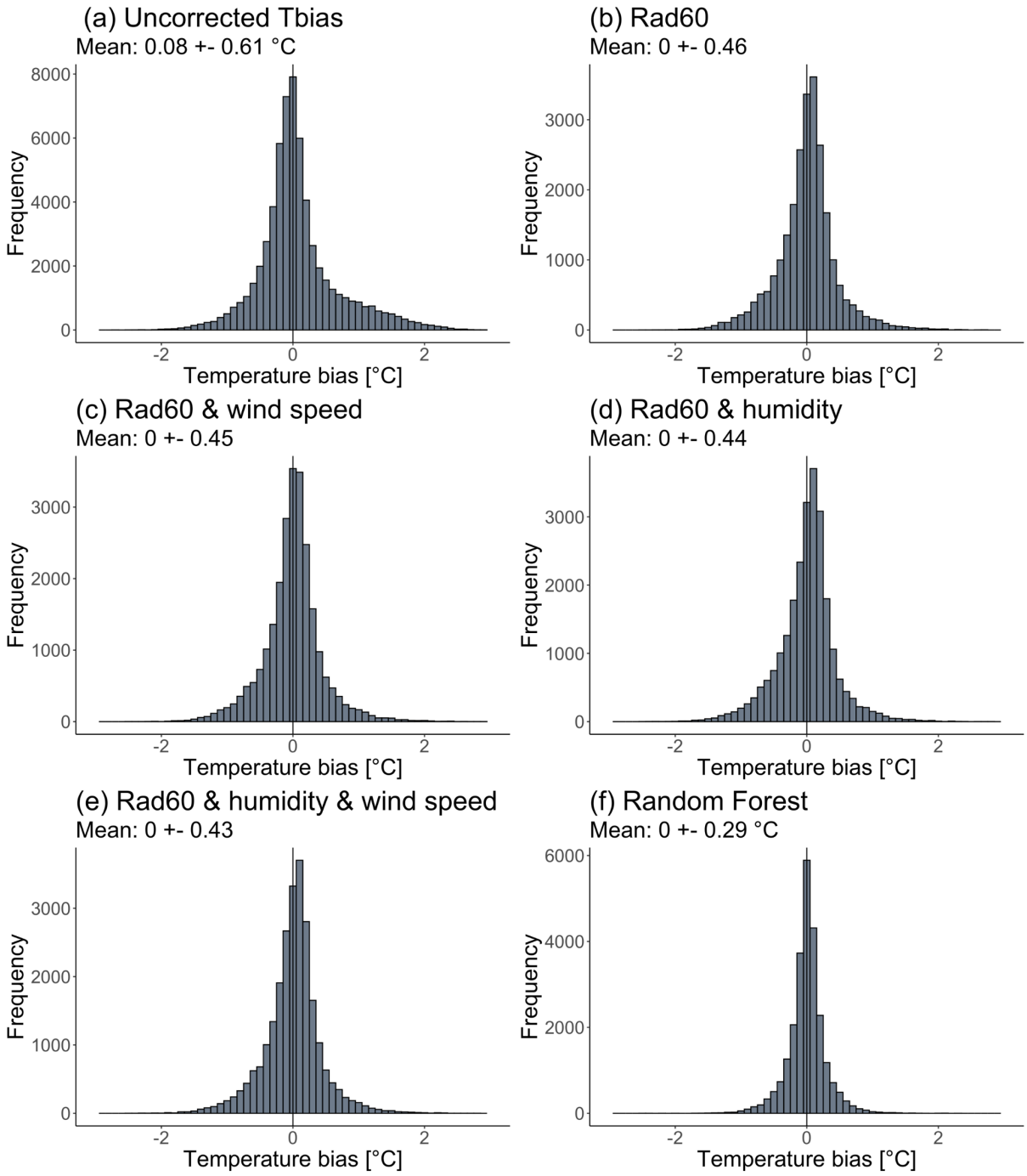

Figure 4.5: The uncorrected temperature bias (a) and the corrected temperature bias after validation with a simple linear regression with the past radiations (b), a multiple linear regression with the past radiations and windspeed (c), a multiple linear regression with the past radiations and humidity (d), a multiple linear regression with the past radiations, humidity and windspeed (e) and a random forest model including temperature, dew point temperature, humidity, radiation, radiation60, windspeed, month and hour (f). Mean biases and their standard deviations are given above the graphs.

Using a simple linear regression using the past radiations is already sufficient to suppress the mean temperature bias. Adding additional variables to the model, such as wind speed, humidity or both is statistically significant but only decreases the RMSE by one percentage. The random forest model results in an RMSE of 0.2868 and R^2 of 0.7614, indicating a better precision and more robust model.

4.2.1.3 Validating the random forest predictor for temperature bias

The random forest prediction of temperature bias showed decent results. When these results are presented for day and night separately (figure 4.6), we obtain a smaller standard deviation of the bias during nighttime (0.26) than daytime (0.31). The statistical details of the random forest model are summarized in table 4.4.

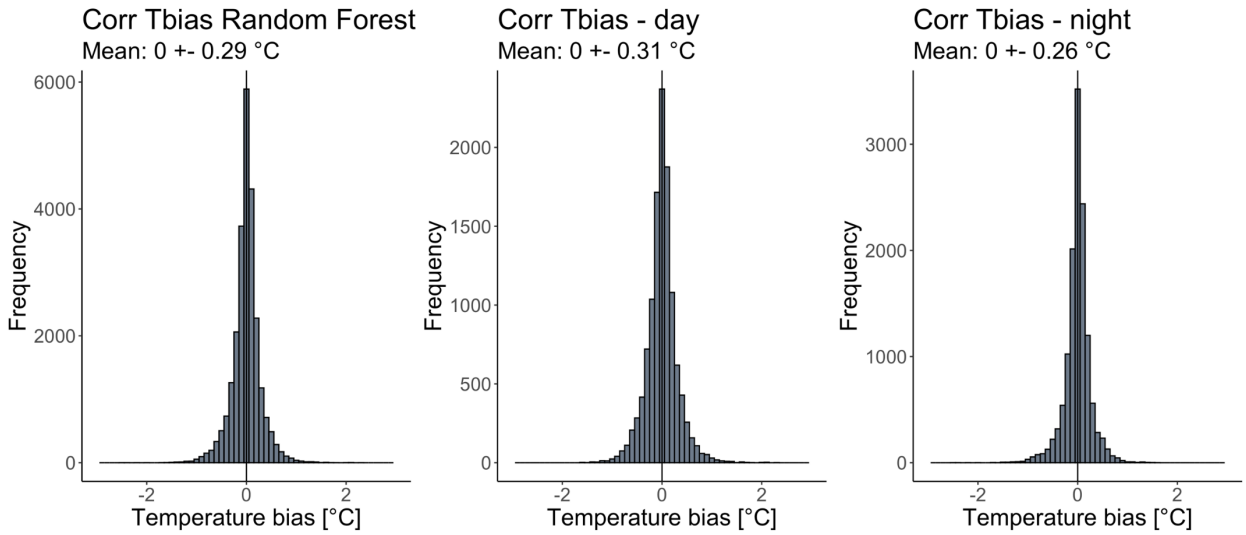

Figure 4.6: The corrected temperature bias (Tbias) after validation with the random forest model for day and night (left), for daytime (center) and for nighttime (right). Mean biases and their standard deviations are given above the graphs.

Table 4.4: Statistical details of the random forest prediction model for temperature bias.

Formula	Tbias ~ Temperature + Humidity + Dew point temperature + Radiation + Radiation60 + Windspeed + Month + Hour
Number of trees	500
Number of variables tried at each split	2
Mean of squared residuals	0.089
% variance explained	76.14
RMSE	0.287

To check whether this prediction model, designed for Uccle, is applicable for stations located on a different location we applied this model to the other reference stations. The results are illustrated in figure 4.7. On the left side the uncorrected temperature biases, the differences between the uncorrected temperature measured by the reference stations and the temperature measured by the official RMI stations in Uccle and Diepenbeek, are shown. On the right side you can find the corrected temperature biases, calculated as the differences between the corrected temperatures given by the predictor model and the temperatures measured by the official RMI stations. For GarmonR02 we see a reduction of the standard deviation from 0.41 to 0.28. The mean bias has however shifted from 0.09 to 0.15. The standard deviation of both GarmonR03 and GarmonR04 has increased from 0.25 to 0.28. The mean bias of GarmonR03

shifted from 0.12 to 0.17, while the mean bias of GarmonR04 show a small decrease from -0.08 to -0.03.

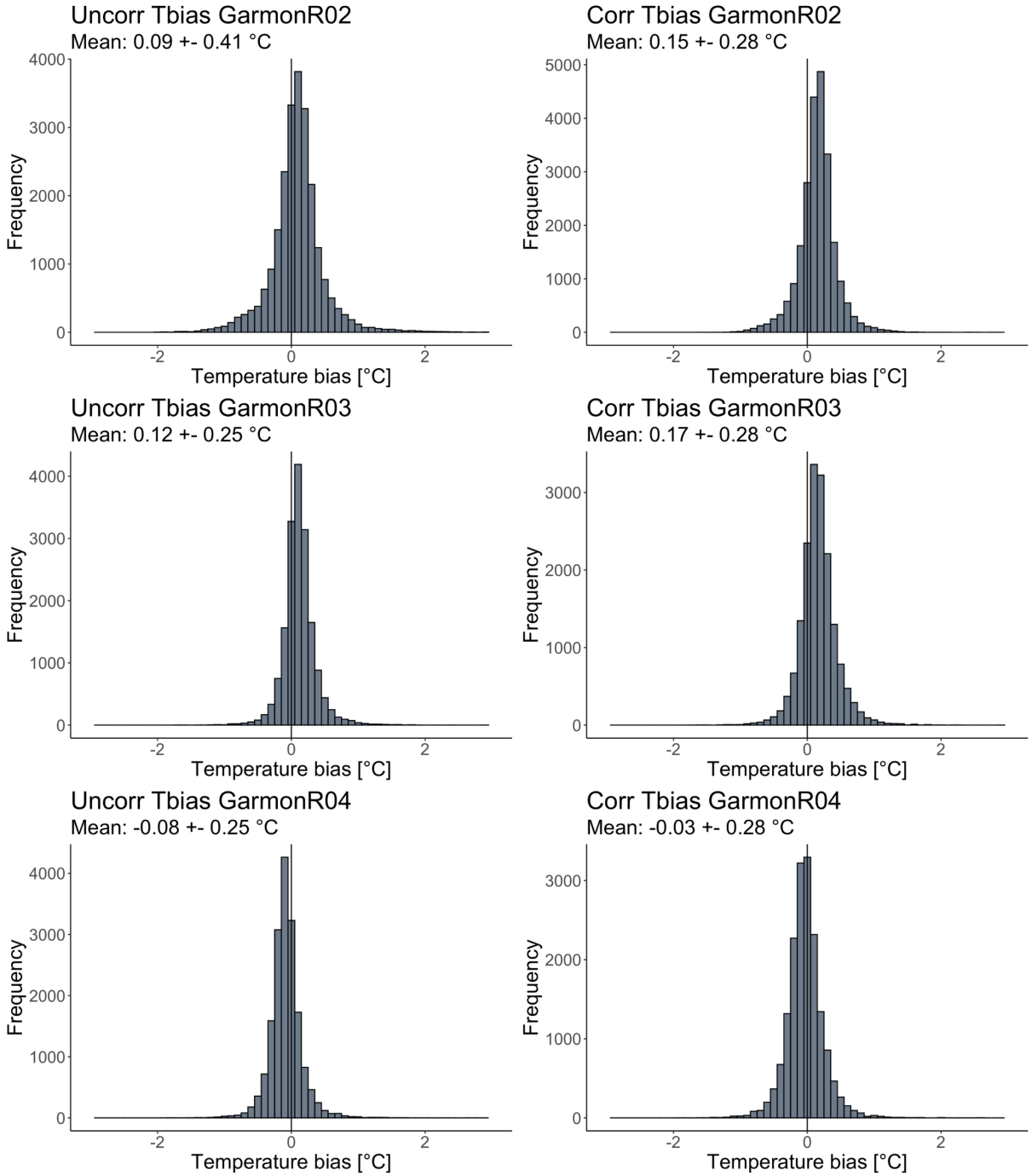

Figure 4.7: The uncorrected (left) and corrected temperature biases (right) of the reference stations GarmonR02, GarmonR03 and GarmonR04. Mean biases and their standard deviations are given above the graphs.

The random forest correction model is used to predict the temperature bias of every low-cost weather station located in Leuven. After adding this temperature bias to the measured temperature, you obtain a corrected temperature for every station in function of its local climatic conditions. These corrected temperatures are used for further analyses.

4.2.2 Spatio-temporal maps of Leuven's UHI

After performing the gap analysis, in which stations that did not record any measurements for at least 30 minutes were removed, only a limited number of weather stations remained. Since stations were continuously installed during the summer of 2019, this number differs for different temporal scales. Table 4.5 summarizes the number of stations for each temporal scale.

Table 4.5: The number of stations remaining after the gap analysis for multiple temporal scales: two heatwave days, two heatwave weeks, the five hottest nights/days and the most extreme and five most extreme clear nights during the measuring period.

Temporal scale	Date	# of stations	Date	# of stations
SUMMER URBAN HEAT ISLAND				
Heatwave day	August 28th night	54	August 28th day	55
Heatwave week	August 23th -28th nights	41	August 23th -28th days	40
5 hottest days	July 24th, 25th, 26th and August 27th, 28th nights	32	July 24th, 25th, 26th and August 27th, 28th days	27
WINTER URBAN HEAT ISLAND				
1 clear night	February 7th morning			68
5 clearest nights	January 16th, 19th, February 7th, 21th and March 3rd mornings			61

Because stations were continuously installed during the summer and autumn of 2019, we see an increase in number of stations from July to March. Looking at an entire week or combination of days decreases the number of active weather stations.

4.2.2.1 Absolute minimum temperatures

The absolute minimum temperatures observed during a heatwave night, a heatwave week (nights) and the five hottest nights during the measuring period are illustrated in figure 4.8. Figure 4.9 shows the minimum temperatures observed during the morning(s) followed by the clearest night and five most clear nights of the measuring period.

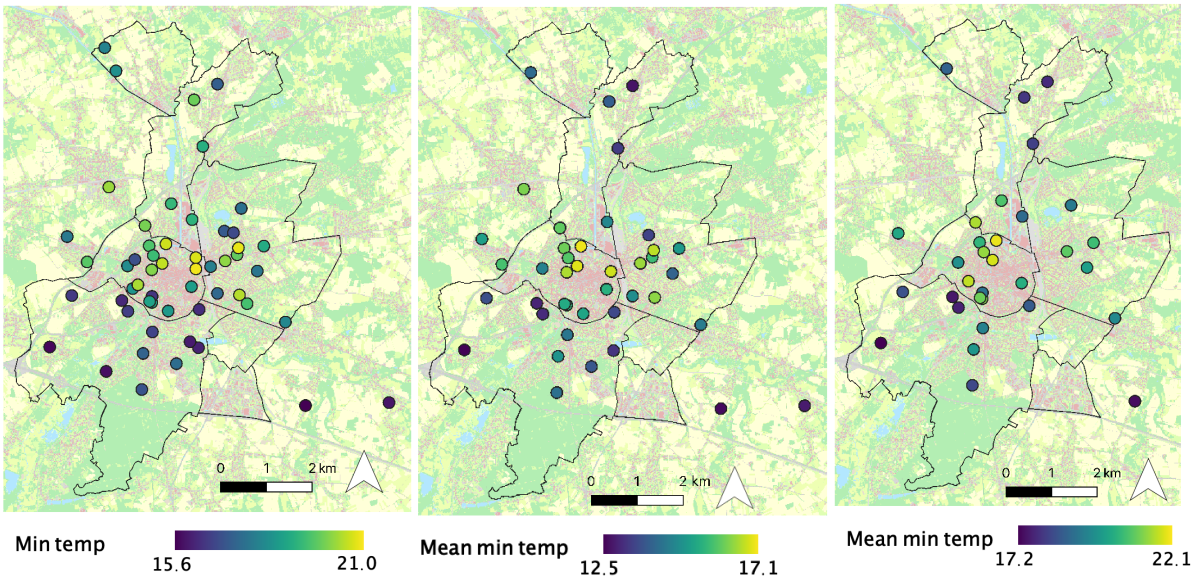

Figure 4.8: Minimum temperatures observed during August 28th (left), the week of August 23th – 28th (center) and the five hottest nights during the measuring periods (right).

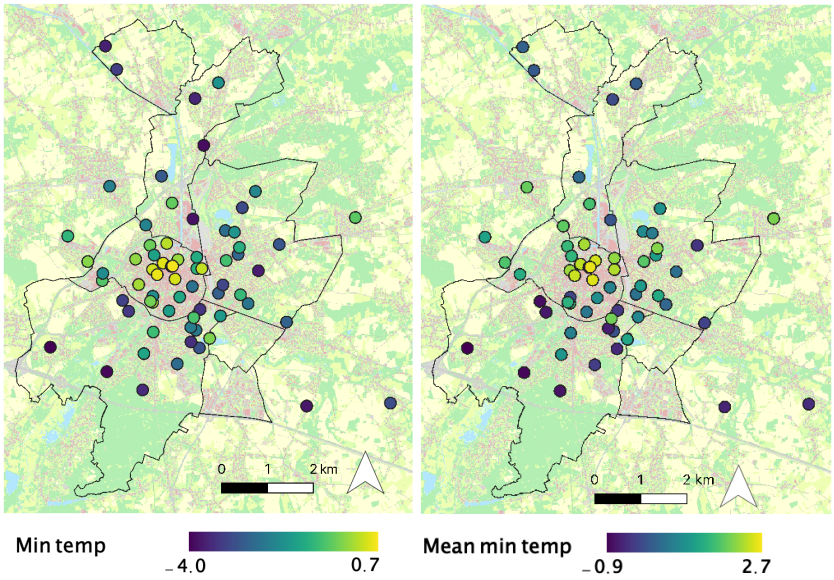

Figure 4.9: Minimum temperatures observed during the morning of February 7th (left) and during the mornings the five clearest nights during the measuring periods (right).

As, expected the highest minimum temperatures occur in the city centre of Leuven as well as in the densely built-up neighbourhoods of Kessel-Lo, while the lowest temperatures occur in the suburban municipalities surrounding the city centre. During summer we see the same temperature range of 5°C for all temporal scales, but the minima and maxima temperatures vary in between them. During winter the same temperature range of 5°C is noticed for 1 morning, when looking at a combination of mornings a temperature range of 3°C is noted. The gradual decrease in minimum temperature from the urban region towards to suburban and more natural surroundings is more clearly visible during winter.

4.2.2.2 Absolute maximum temperatures

Figure 4.10 presents the absolute maximum temperatures observed during a heatwave day, a heatwave week (days) and the five hottest days during the measuring period.

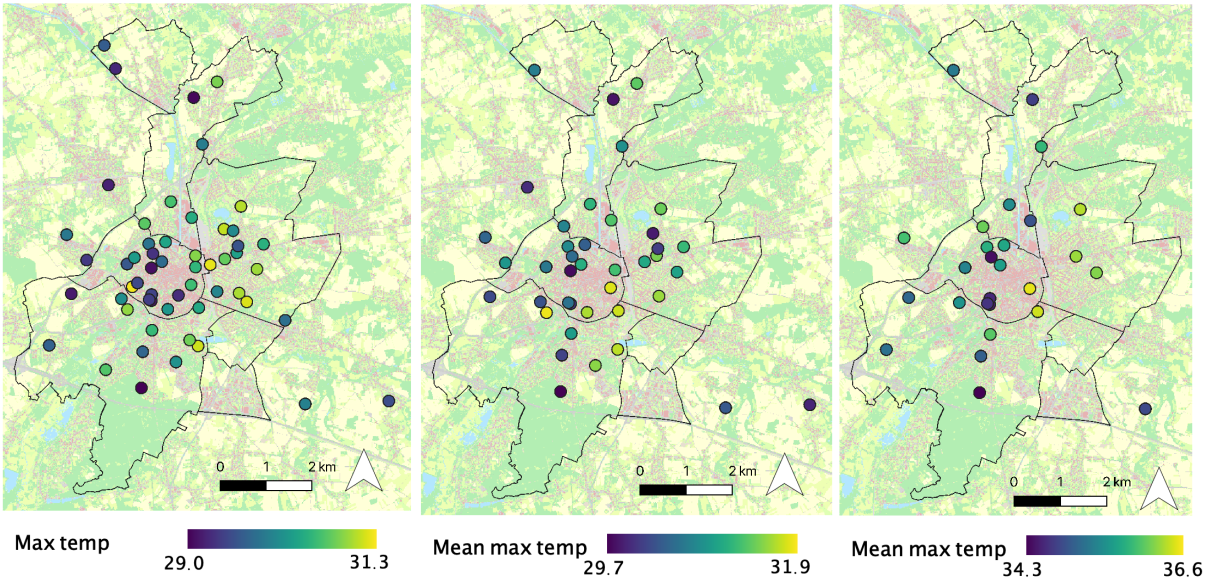

Figure 4.10: Maximum temperatures observed during August 28th (left), the week of August 23th – 28th (center) and the five hottest days during the measuring periods (right).

The maximum temperature range equals 2.3°C, which is only half as wide as the temperature range observed for minimum temperatures during night-time (figure 4.8). The distribution of cooler and warmer stations shows a more random pattern compared to figure 4.8, lacking the gradual decrease in temperature from the urban environment to the rural surroundings.

4.2.2.3 Changing temperature difference

A temperature profile, showing the corrected temperatures of a rural station (Garmon030) and urban station (Garmon049) as well as the mean temperature of all stations during August 27-28th is illustrated in figure 4.11.

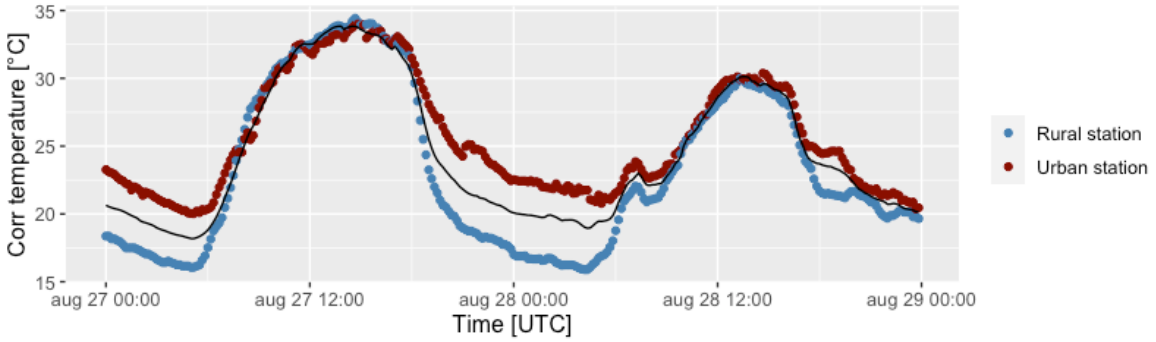

Figure 4.11: Temperature profile of two Garmon stations, a rural station (blue dots) and an urban station (red dots), next to the mean (black line) temperature of all stations active during August 28th.

After sunrise, around 06h00, air temperatures start to increase. They reach their maximum value around 14h00. This peak is followed by a decrease in temperature, just before sunrise (around 05h00) minimum temperatures are obtained. During daytime (06u00 - 17h50) no clear difference between the two weather stations is found, during night-time (18h00 - 05h50) the opposite is true. After 18h00 the rural station shows a steeper decrease in temperature compared to the urban station, the temperature difference between both stations reaches a maximum value just before sunrise.

For each station, the difference between its temperature and mean temperature is calculated at every timestep (every 10 minutes). To summarize these results for all stations, the differences are summed up for all timesteps and divided by the number of timesteps. This gives the mean temperature difference between a certain station and the mean of all stations. The mean temperature differences overnight during a heatwave night, a heatwave week (nights) and the five hottest nights during the measuring period are illustrated in figure 4.12. The graphs presenting this difference during daytime are given in figure 4.13. In figure 4.14 the mean temperature difference in winter are presented.

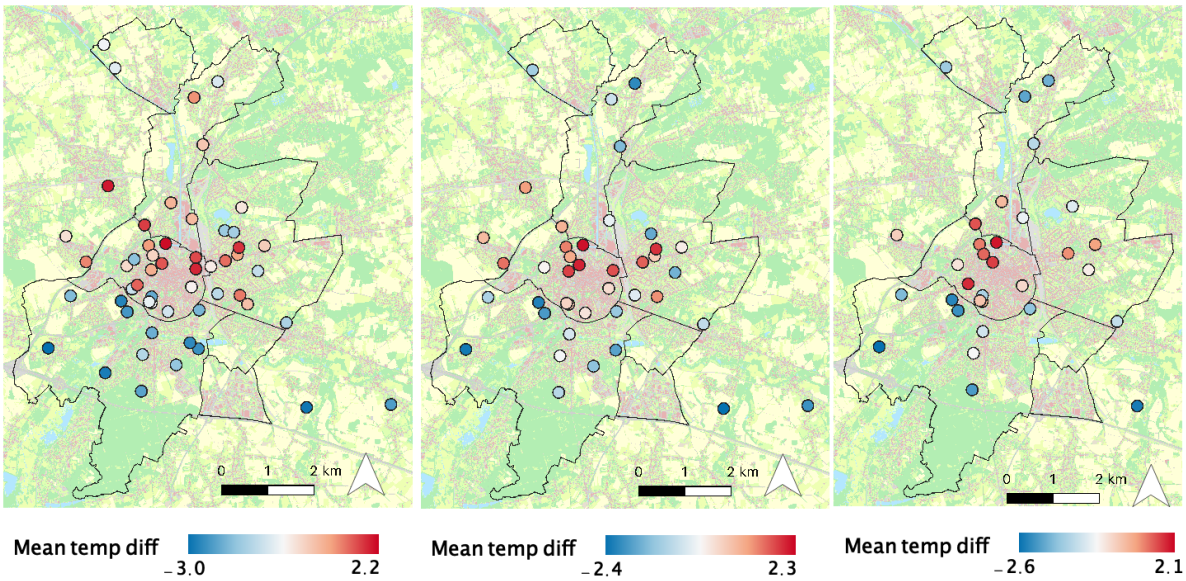

Figure 4.12: Mean temperature difference (night) observed during August 28th (left), the week of August 23th – 28th (center) and the five hottest nights during the measuring periods (right).

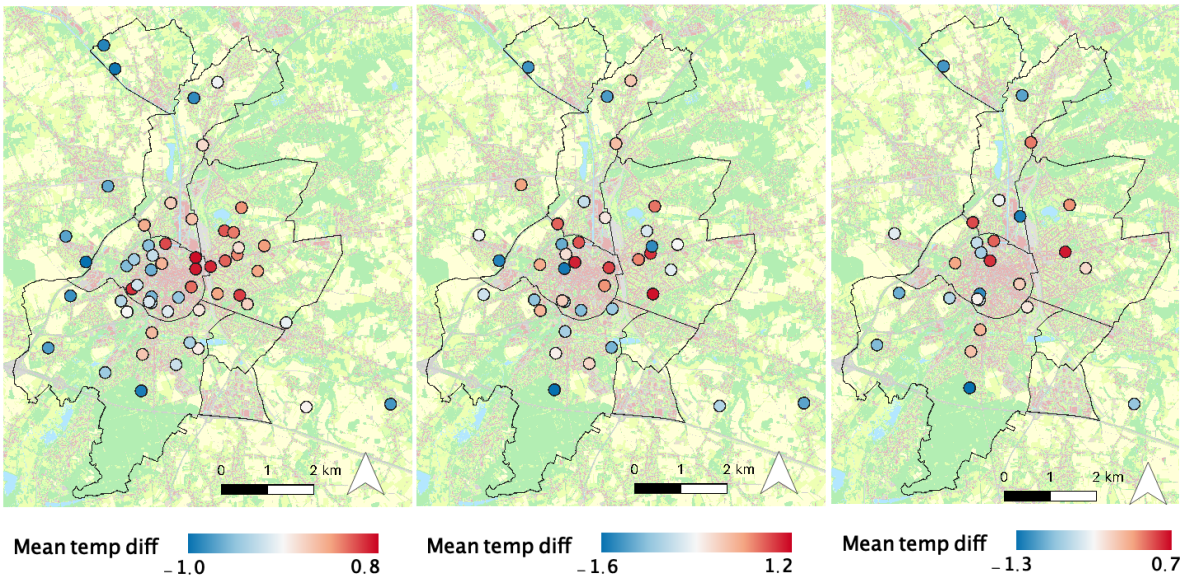

Figure 4.13: Mean temperature difference (day) observed during August 28th (left), the week of August 23th – 28th (center) and the five hottest days during the measuring periods (right).

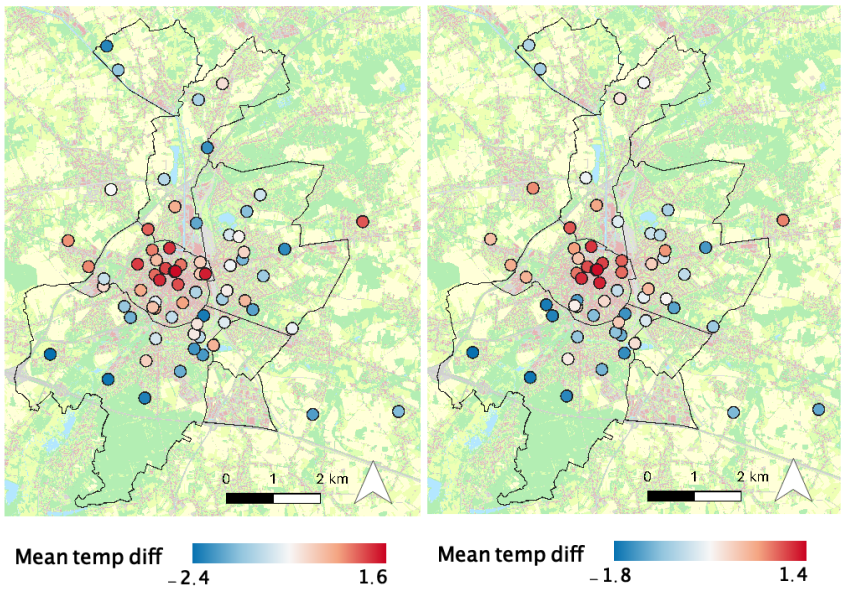

Figure 4.14: Mean temperature difference observed during the morning of February 7th (left) and during the mornings the five clearest nights during the measuring periods (right).

Weather stations with a negative value observe lower temperatures compared to the mean temperature of all stations, a positive value indicates stations observing higher temperatures than the mean temperature of all stations. Figures 4.12 and 4.14 are in concordance with figures 4.8 and 4.9, they show positive values in the city centre of Leuven and in Kessel-Lo, while the negative values are situated in the less densely populated municipalities Oud-Heverlee, Bierbeek, Wijgmaal and Wilsele. Neutral values are located in between both of these extremes. During daytime (figure 4.13) a different and more random patterns occurs.

4.2.2.4 Thom's discomfort index

The Thom's discomfort index calculated using mean night temperatures and relative humidity's observed during one heatwave night, a heatwave week (nights) and the five hottest nights are illustrated in figure 4.15.

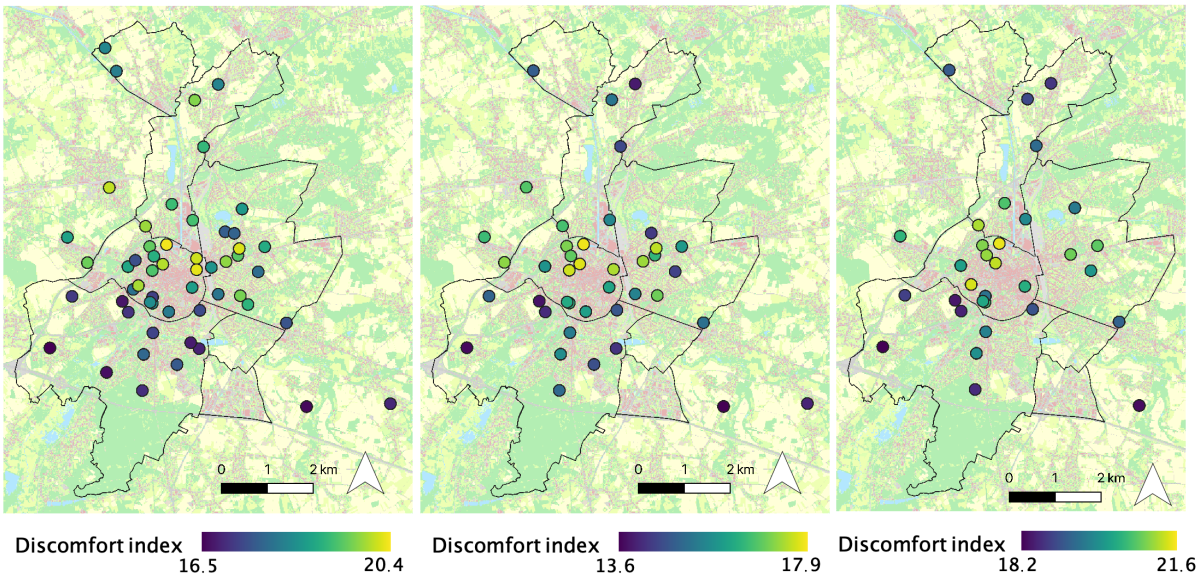

Figure 4.15: The Thom's discomfort index calculated using mean night temperatures and humidity's observed during August 28th (left), the week of August 23th – 28th (center) and the five hottest nights during the measuring periods (right).

The discomfort indexes reach their maximum values within the city centre, lower values occur towards the surrounding suburban regions. The highest discomfort indexes are noted when using observations from the five hottest nights, looking at an entire heatwave week lowers the discomfort indexes. All temporal scales show a similar range of discomfort indexes around 4.

Figure 4.16 illustrates the mean temperature and relative humidity observed during August 28th (night) followed by the resulting Thom's discomfort index. Higher mean temperatures are observed in the city centre and northern sub-urban municipalities, while lower temperatures are registered in the southern sub-urban municipalities. The opposite is true for the mean humidity measurements. We can even confirm that the station with the highest mean temperature has the lowest mean relative humidity and vice versa.

Figure 4.17 represents the Thom's discomfort index calculated using the mean day temperatures and relative humidity's for the three temporal scales; one heatwave day, a heatwave week (days) and the five hottest days during the measuring period.

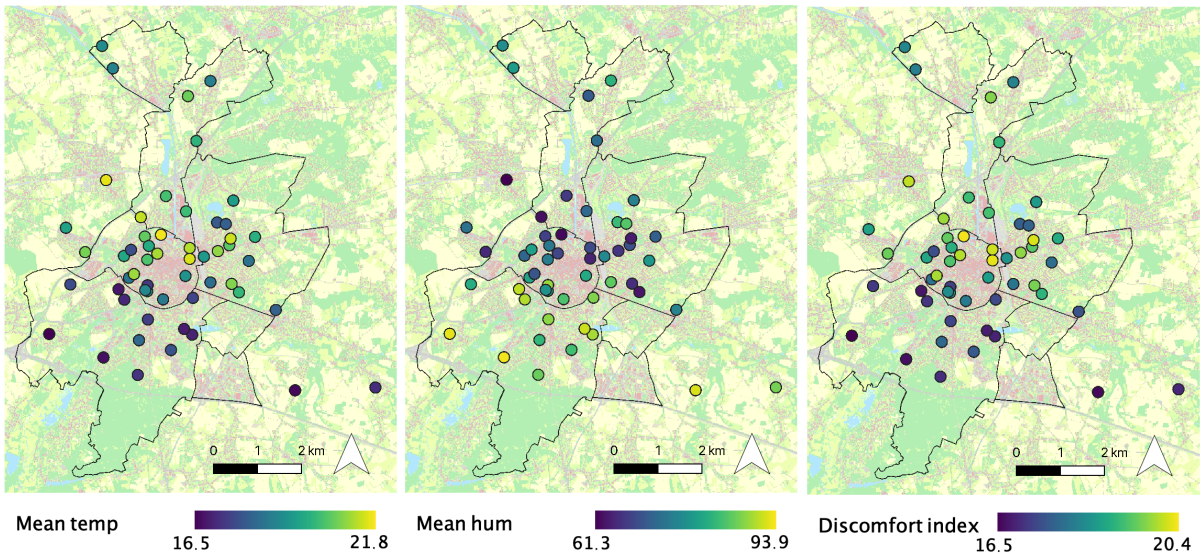

Figure 4.16: The observed mean temperature (left) and mean humidity (center), followed by the calculated Thom's discomfort index during the night of August 28th.

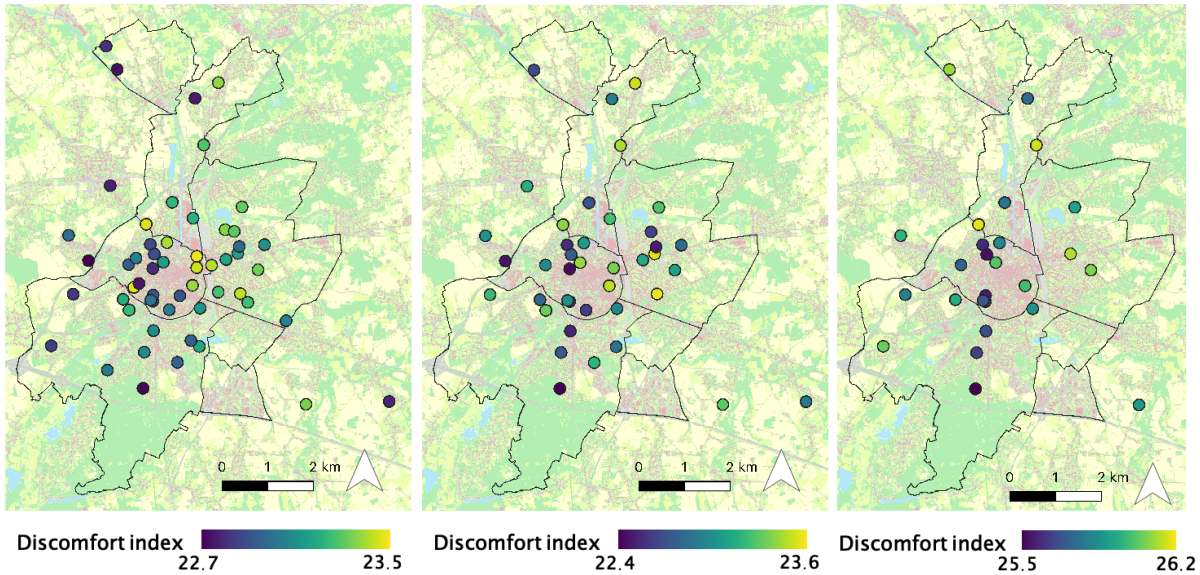

Figure 4.17: The Thom's discomfort index calculated using mean day temperatures and humidity's observed during August 28th (left), the week of August 23th – 28th (center) and the five hottest nights during the measuring periods (right).

The decrease in discomfort index from the urban centre towards the suburban regions is less clear during day time (figure 4.17) compared to night time (figure 4.15). The highest discomfort indexes are noted when looking at the five hottest days, looking at an entire heatwave week again lowers the discomfort indexes. The range of discomfort indexes during daytime (figure 4.17) is much smaller compared to night time (figure 4.15) and differs for different timescales. When observations of the five hottest day or one heatwave day are taken into account, the indexes only range over 0.7 and 0.8 respectively. The discomfort index over an entire heatwave week range show a range of 1.

4.3 Urban green infrastructure (UGI)

4.3.1 Green map of Leuven's UGI

A detailed green map of Leuven is created using an object-based image analysis, hereby classifying the urban green in both high and low green. The resulting green map is presented in appendix 8.4.

The confusion matrix is presented in table 4.6. The overall, producer's and user's accuracy as well as the Kappa head are calculated from the confusion matrix. High green shows the highest producer's and user's accuracy followed by low green and others. The green map has an overall accuracy 91.25% and a Kappa head equal to 0.862.

Table 4.6: The error matrix of the green map using a minimum distance algorithm.

		Reference			User accuracy
		High	Low	Other	
Classified	High	**511**	29	17	91.74 %
	Low	35	**465**	11	91.01 %
	Other	10	13	**223**	90.65 %
Producer accuracy		91.91 %	91.72 %	88.84 %	

4.3.2 Spatial patterns of Leuven's UGI

The mean values and kernel probability densities of the calculated landscape metrics for August 28th in each buffer region are illustrated in figure 4.18. More detailed tables, including the minimum, maximum, mean and standard deviation values of each landscape metric for every buffer are included in appendix 8.6 (table 8.4 to table 8.9).

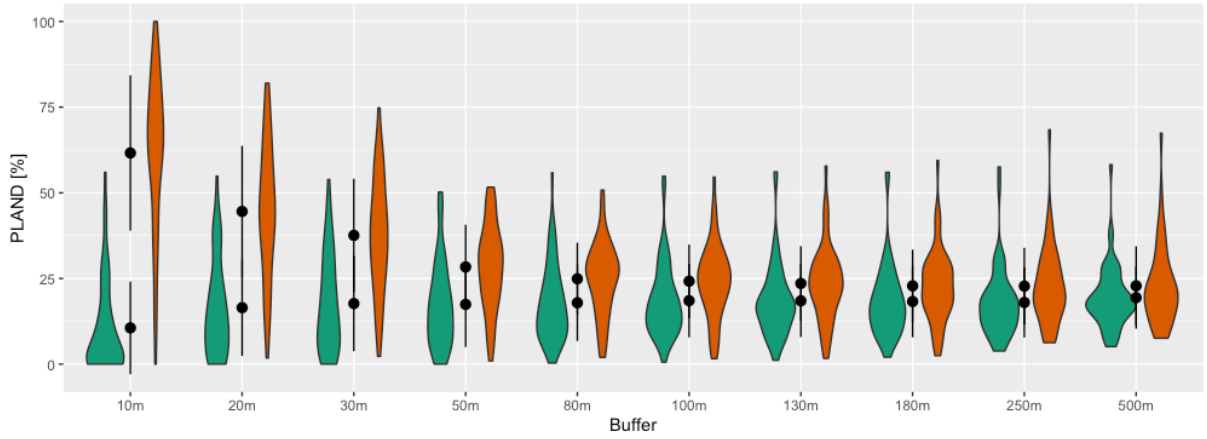

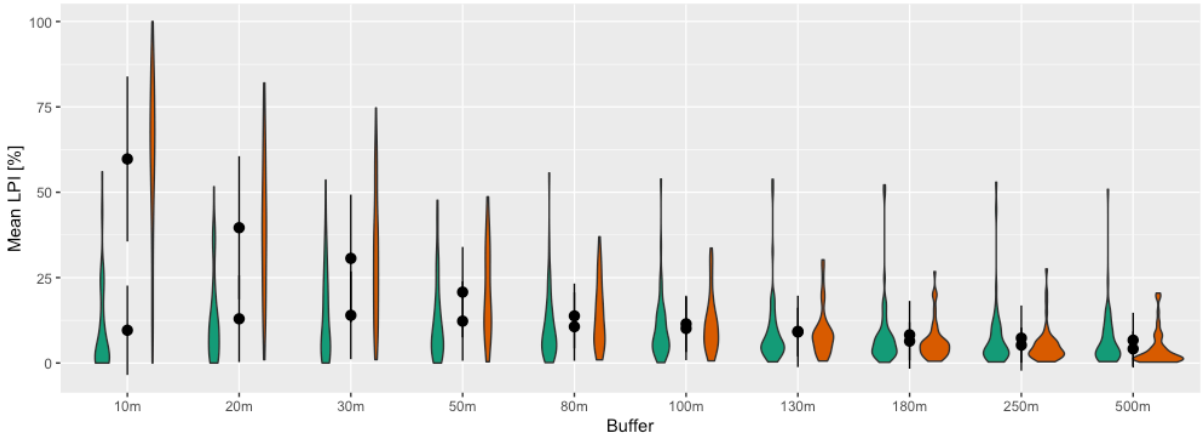
Mean LPI [%]
100
75
50
25
0
10m
20m
30m
50m
80m
100m
130m
180m
250m
500m
Buffer

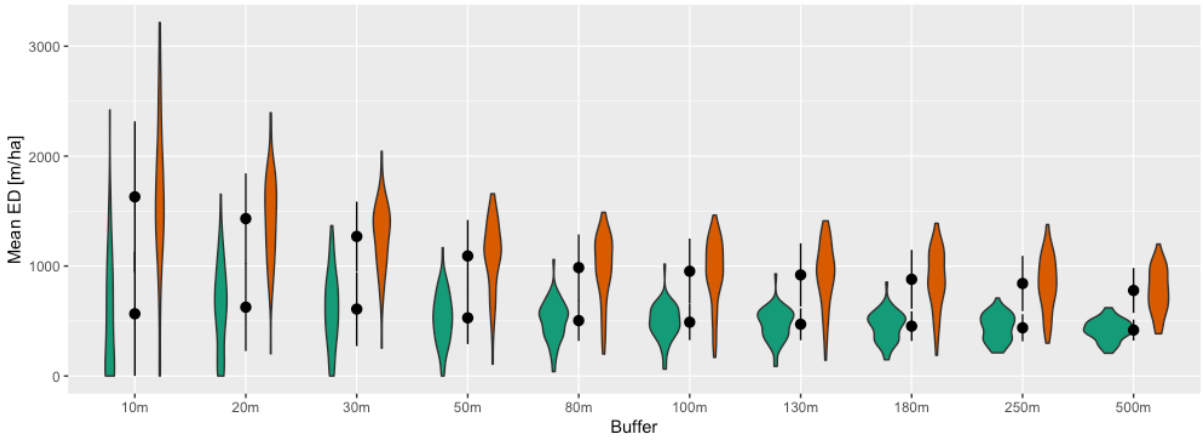
Mean ED [m/ha]
3000
2000
1000
0
10m
20m
30m
50m
80m
100m
130m
180m
250m
500m
Buffer

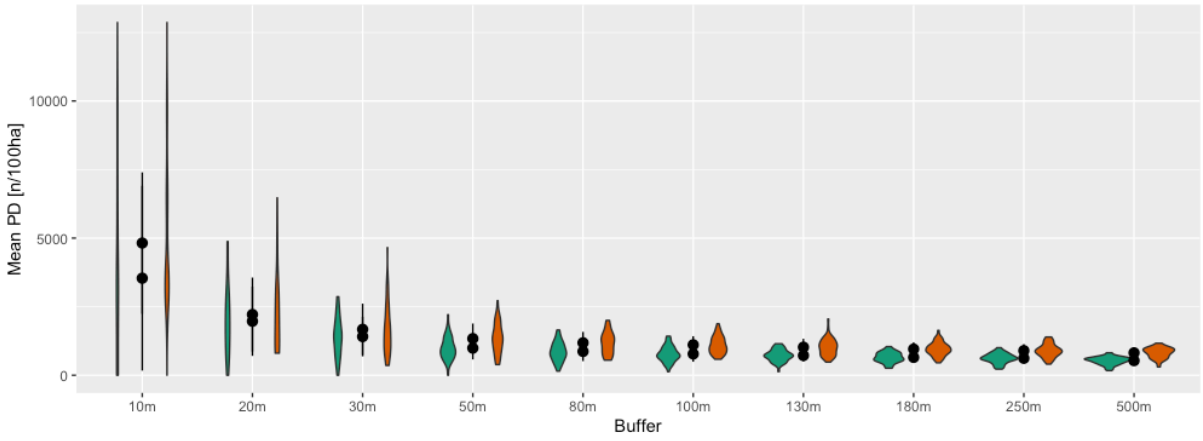
Mean PD [n/100ha]
10000
5000
0
10m
20m
30m
50m
80m
100m
130m
180m
250m
500m
Buffer

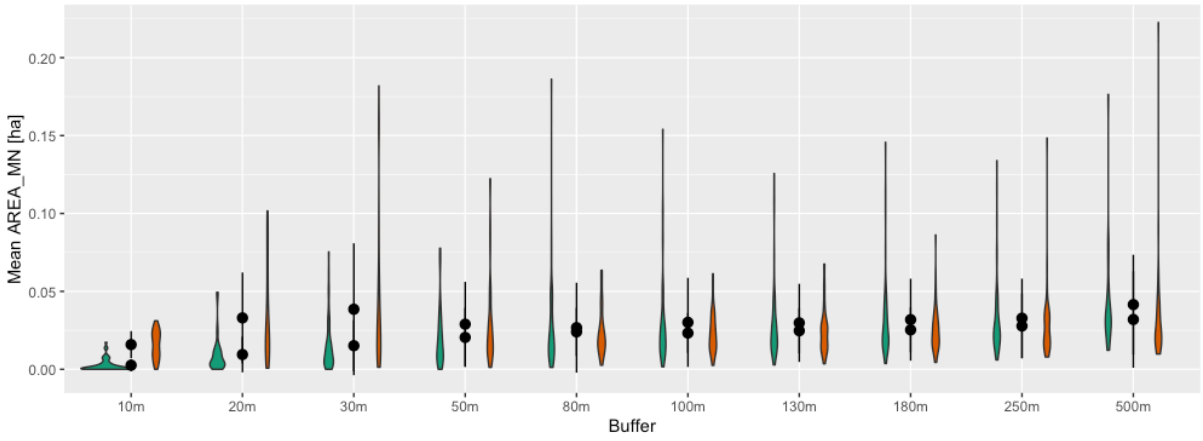
Mean AREA_MN [ha]
0.20
0.15
0.10
0.05
0.00
10m
20m
30m
50m
80m
100m
130m
180m
250m
500m
Buffer

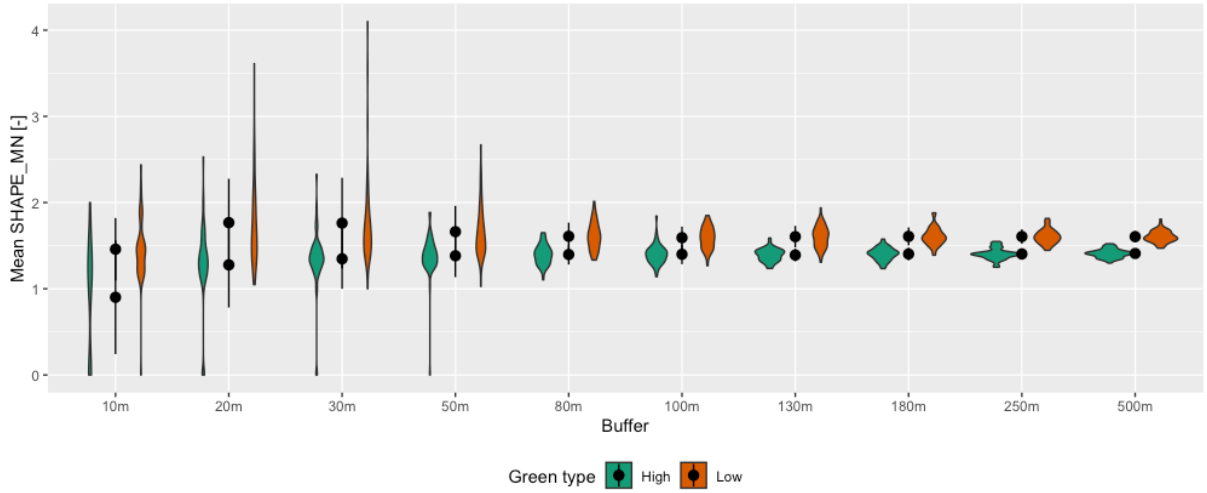

Figure 4.18: The mean values and kernel probability density of the landscape metrics, PLAND, LPI, PD, ED, AREA_MN and SHAPE_MN, for both high and low green in the 10 buffer zones.

The mean percentage cover (PLAND) of low green clearly decreases along the buffers, while the cover of high green only slightly increases. Low green shows an equal data distribution, high green shows a right-skewed distribution. For low green, the mean largest patch index (LPI) shows similar results, while this landscape metric remains almost constant for high green. High green's largest patch index has a right-skewed distribution for all buffers, for low green this is only the case for the larger buffer zones. The mean edge density (ED) shows similar patterns as the largest patch index, a decrease for low green while high green remains almost constant. The data distribution of high green is right-skewed for the smallest buffer but looks symmetrical for the larger buffer zones. The data distribution of low green is however symmetrical for the smallest and largest buffers but becomes left-skewed for the medium buffers. The mean patch densities (PD) of both high and low green decrease for bigger buffer regions. Both green types seem to have a right-skewed distribution for the smaller buffers, afterwards more symmetrical data distributions occur. The mean patch size (AREA_MN) slightly increases along the buffers for both high and low green but obtains its maximum value for low green in the 30m buffer. The distributions for both green types are highly right-skewed. The mean shape index (SHAPE_MN) shows only a slight increase for both urban green types between the 10m and 20m buffers, for larger buffer regions the values remain constant. The distributions of both low and high green remain symmetrical along all buffers, in the smaller buffers there are some big outliers present.

4.4 Relation between UAT and UGI

4.4.1 Spearman correlation matrix

Because the assumptions for a parametric correlation test mentioned in section 3.3.3.3 did not hold, a spearman correlation test is used to calculate the correlations between the temperature variables and urban green's composition and configuration.

4.4.1.1 Temperature variables vs landscape metrics

In figure 4.19 the pairwise correlations between the night (left) and day (right) air temperature variables of August 28th (one heatwave day) and the landscape metrics for high and low green are illustrated. The temperature variables include minimum temperature (a), maximum temperature (b), mean temperature (c) and the sum of the temperature differences (d).

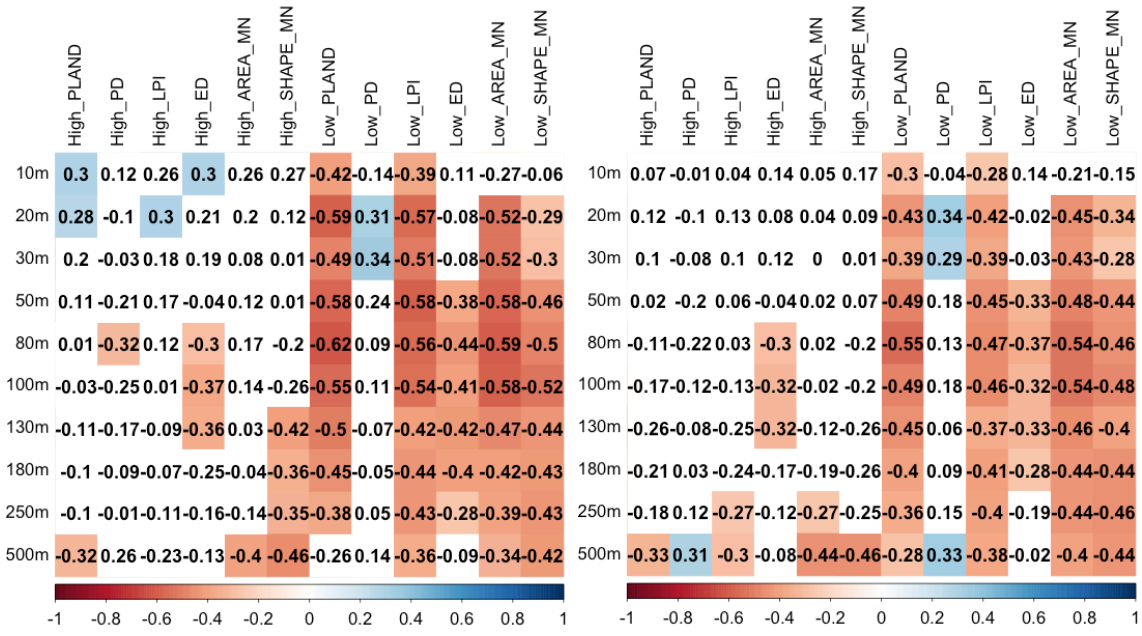

(a) Min temp – August 28th night

(a) Min temp – August 28th day

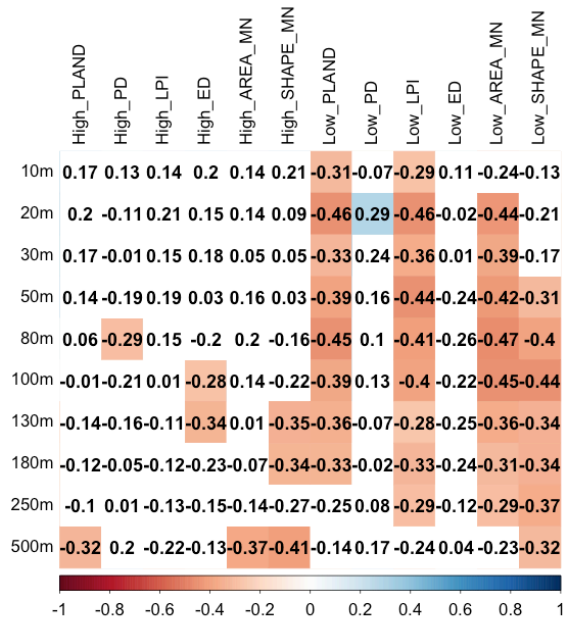

(b) Max temp – August 28th night

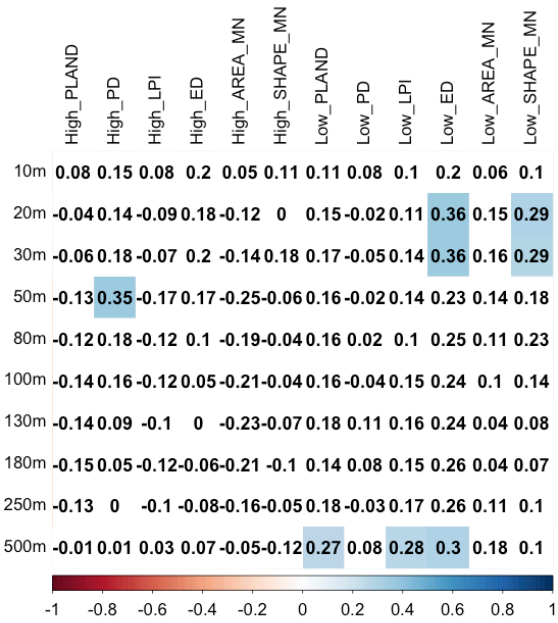

(b) Max temp – August 28th day

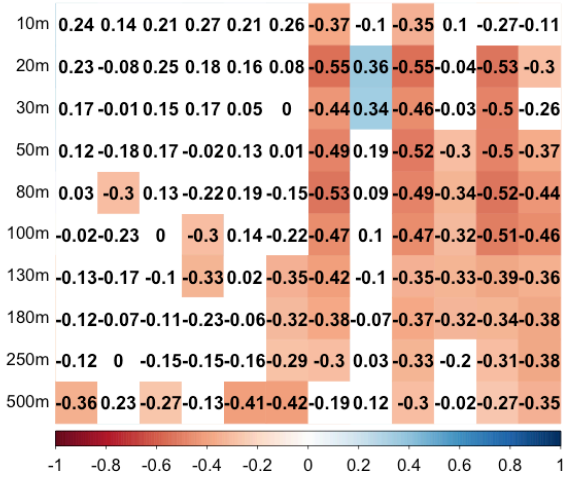

(c) Mean temp – August 28th night

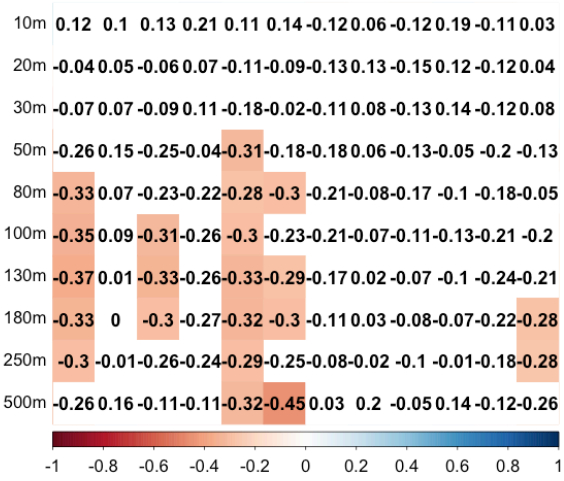

(c) Mean temp – August 28th day

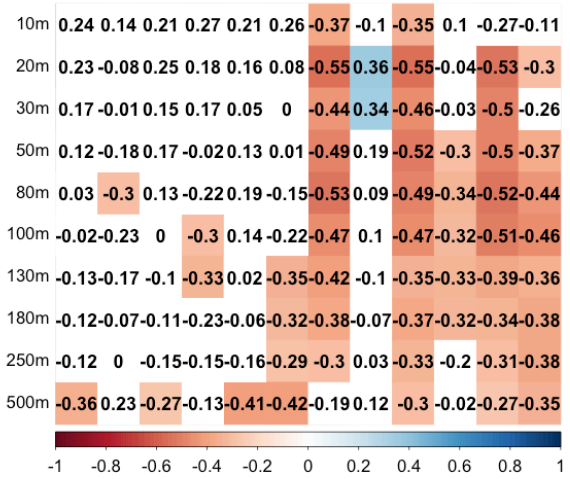

(d) Sum temp diff – August 28th night

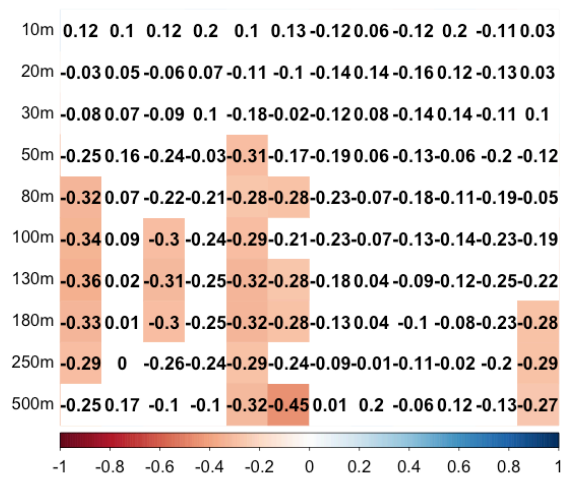

(d) Sum temp diff – August 28th day

Figure 4.19: The pairwise correlations between the night (left) and day (right) minimum temperature (a), maximum temperature (b), mean temperature (c) or the sum of the temperature difference (d) of August 28th and the landscape metrics of high and low green. The colored cells indicate significant correlation (significance level = 0.05).

Minimum temperatures give the most significant results, followed by the mean temperature and sum of the temperature difference which give similar results. The maximum temperature returns the most insignificant results, especially during daytime. The minimum temperature shows more extreme correlations during night time compared to daytime. We obtain negative correlations between minimum temperatures and the PLAND, LPI, ED, AREA_MN and SHAPE_MN of low green for almost all buffer regions. For PD almost no significant correlations are found. Negative correlations for high green are only found at larger buffer regions (≥ 80m). The mean temperature and sum of the temperature difference show similar but less extreme results compared to the minimum temperature during night time, during daytime a completely different pattern is found. Here negative correlations for PLAND, LPI and AREA_MN for high green and SHAPE_MN for both low and high green are present in the buffer zones larger or equal to 50m. For all temperature variables, the most extreme correlation between air temperature and urban green's composition and configuration are found in the 20m and 80m buffer.

Figure 4.20 shows the pairwise correlations between the night (left) and day (right) mean minimum temperature (a), mean maximum temperature (b), mean temperature (c), sum of the temperature differences (d) of August 23th – 28th (one heatwave week) and the landscape metrics for high and low green.

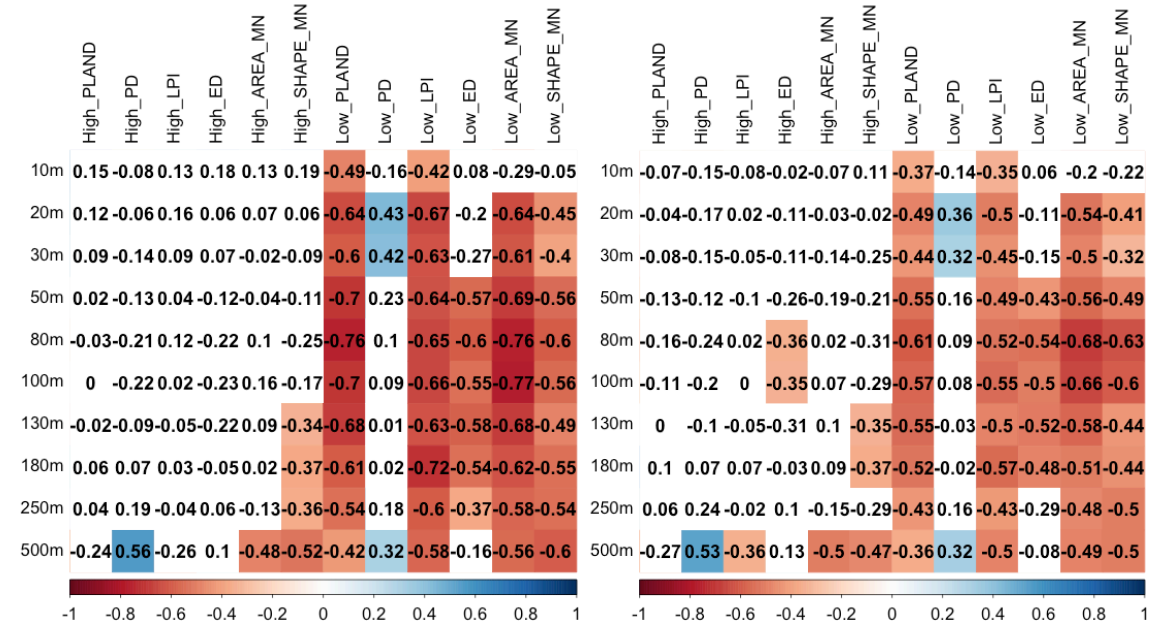

(a) Min temp – August 23-28th nights

(a) Min temp – August 23-28th days

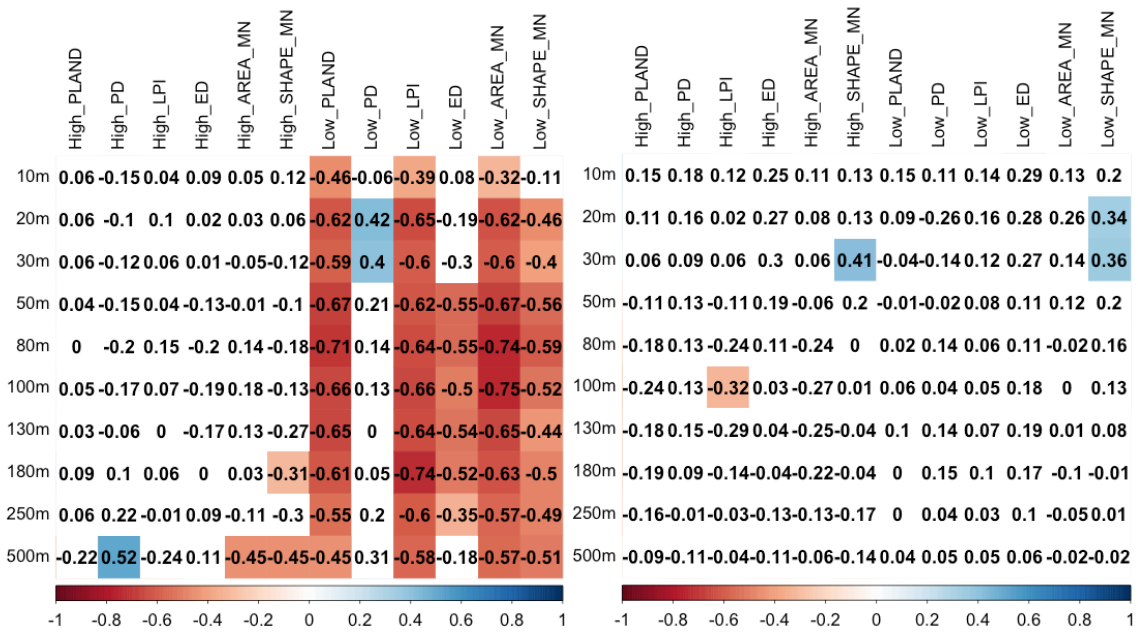

(b) Max temp – August 23-28th nights

(b) Max temp – August 23-28th days

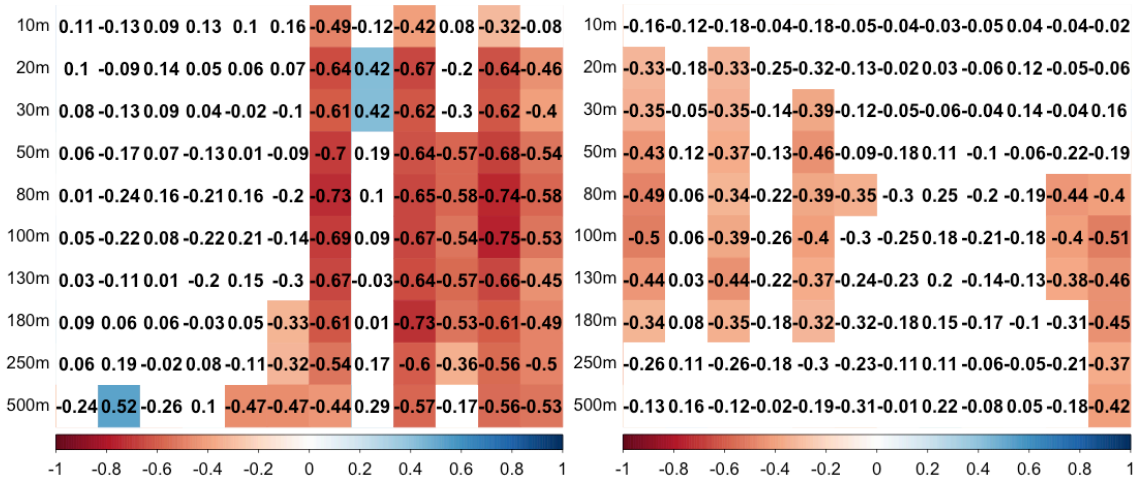

(c) Mean temp – August 23-28th nights

(c) Mean temp – August 23-28th days

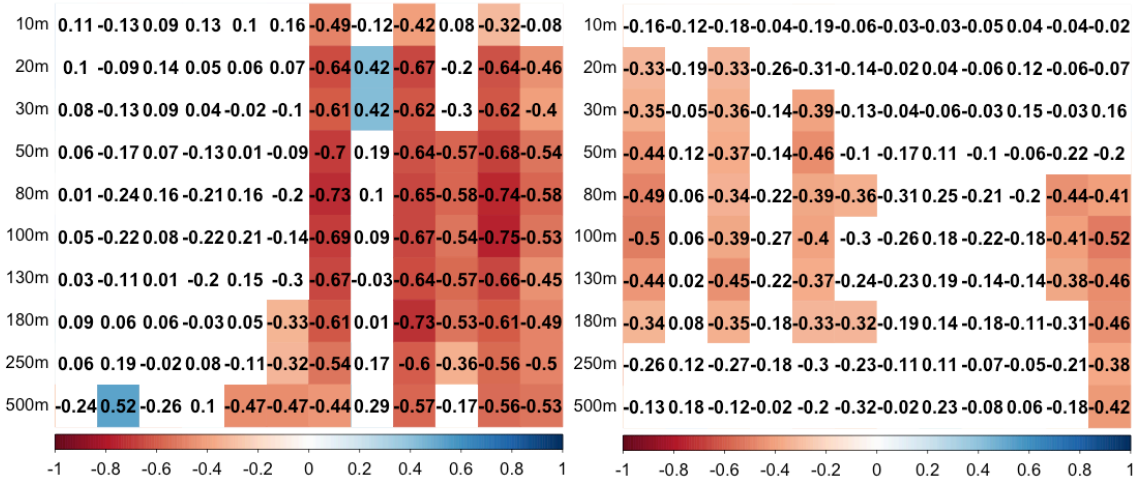

(d) Sum temp diff – August 23-28th nights

(d) Sum temp diff – August 23-28th days

Figure 4.20: The pairwise correlations between the night (left) and day (right) minimum temperature of August 23th – 28th and the landscape metrics of high and low green. The colored cells indicate significant correlation (significance level = 0.05).

The night- and daytime correlations are very similar to the results we obtained for just one heatwave. Generally, we can see the temperature variables for one week result in more extreme correlations. During night time PLAND, LPI, ED, AREA_MN and SHAPE_MN of low green are highly negatively correlated with all temperature variables. In contradiction with the results for one day, here negative correlations of high green are only found at buffer zones ≥ 130m and only for AREA_MN and SHAPE_MN. During daytime more significant correlations for high green are obtained, especially for the mean temperature and the sum of the temperature differences. Negative correlations for high green's PLAND, LPI and AREA_MN are found for all buffer zones between 20m and 180m. For low green figure 4.20 shows negative correlations for AREA_MN and SHAPE_MN in the larger buffer regions (≥ 80m).

4.4.1.2 Thom's discomfort index vs landscape metrics

The pairwise correlation coefficients between the night (left) and day (right) thermal discomfort indexes for one heatwave day (August 28th) and one heatwave week (August 23th-28th) and the landscape metrics for high and low green are graphically presented in figure 4.21.

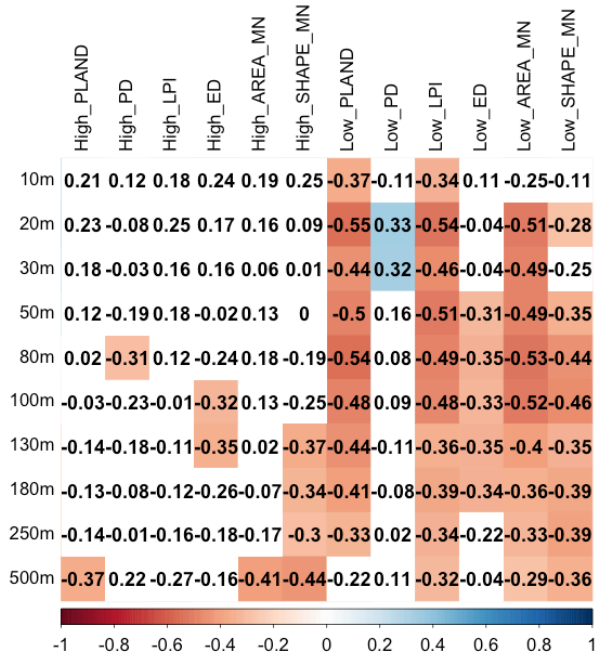

(a) Discomfort index – August 28th night

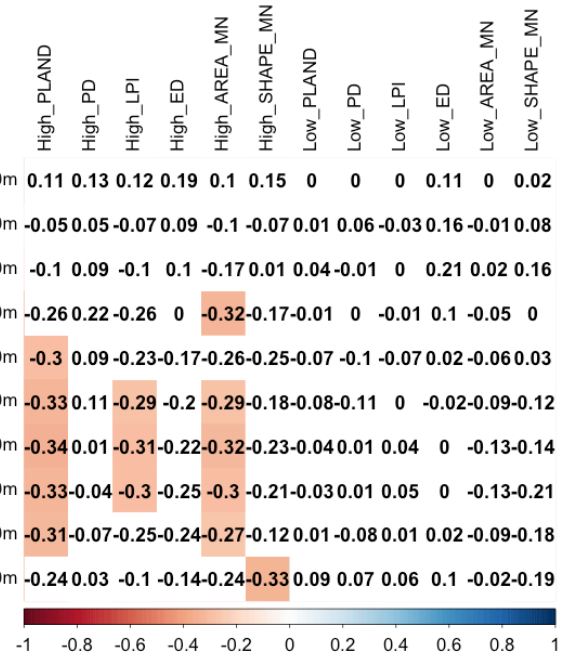

(a) Discomfort index – August 28th day

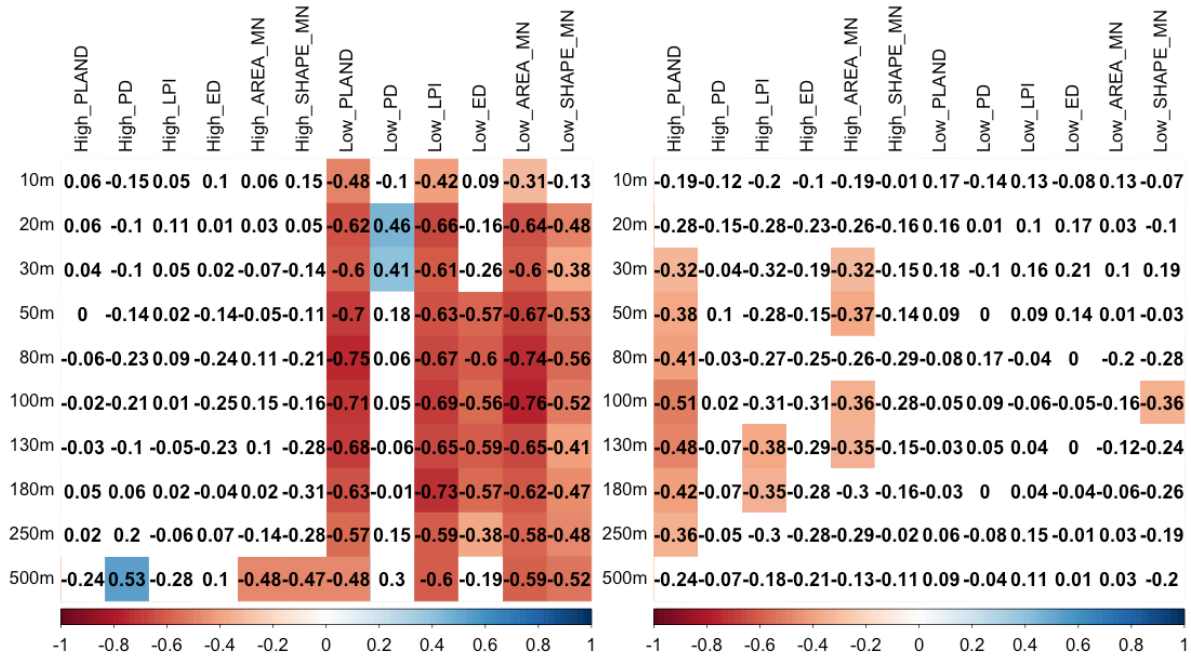

(b) Discomfort index – August 23-28th nights (b) Discomfort index – August 23-28th days

Figure 4.21: The pairwise correlations between the night (left) and day (right) discomfort indexes of August 28th (a) and August 23th – 28th (b) and the landscape metrics of high and low green. The colored cells indicate significant correlation (significance level = 0.05).

The correlation coefficients for one heatwave day or a complete heatwave week are quite similar. During nighttime more extreme correlation coefficients are obtained for a heatwave week compared to a heatwave day, during daytime we see a shift in significant buffers when the two timeframes are compared. For one day the 80m to 250m buffer are the dominant buffers, for one week this range is enlarged from the 30m to 250m buffer. In general, we can see more negative correlations for low green during nighttime and more negative correlations for high green during daytime. The values for the DI index resemble those of the mean temperature and sum of the temperature differences in figures 4.19 (c)/(d) and 4.20 (c)/(d).

4.4.1.3 Temperature variables and discomfort index vs environmental factors

Figure 4.22 shows the pairwise correlation between the night (left) and day (right) temperature variables and discomfort indexes of August 28th (one heatwave day) and August 23th-28th (one heatwave week) and the station's environmental factors. The station's environmental factors include the area, perimeter, compactness and SVF. Since these variables do not differ between different buffers, they can be shown in one matrix for day or night.

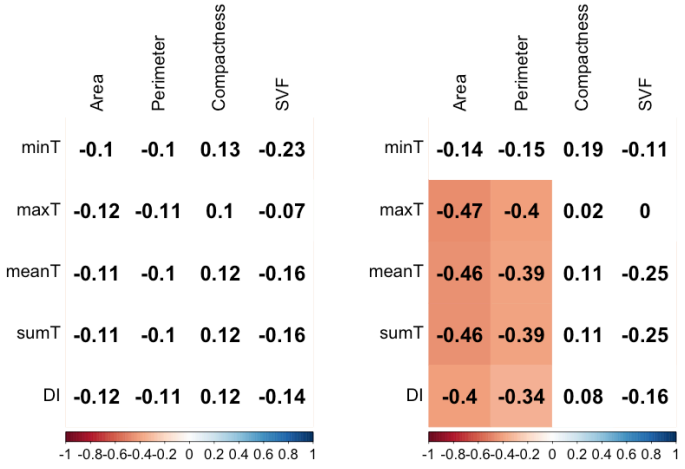

(a) August 28th night (a) August 28th day

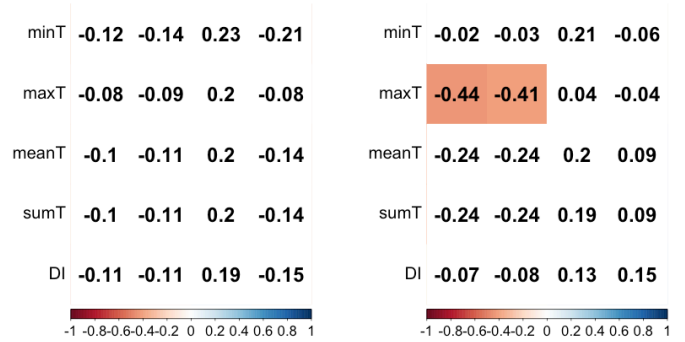

(b) August 23-28th nights (b) August 23-28th days

Figure 4.22: The pairwise correlations between the night (left) and day (right) minimum temperature, maximum temperature, mean temperature, sum of the temperature difference and discomfort index of August 28th and August 23th – 28th and the station's environmental factors.

During night-time we do not notice any significant correlations. During daytime no significant correlations for minimum temperatures are found. The other temperature variables show negative correlations with area and perimeter. The same is true for the discomfort indexes. Even though the correlation between temperature and both compactness and SVF are not significant, we still notice positive and negative correlation coefficients for the environmental variables respectively. For one week only the maximum day temperature shows significant correlations.

4.4.2 Simple linear regression model

Figures 8.5 to 8.34 in appendix 8.7 show scatterplots between a specific temperature variable and landscape metric of high and low green for multiple spatial and temporal scales. The plots can easily be used to compare different spatial extents for one temporal scale or vice versa. Additionally, they show the range of each landscape metric for the different green types and the 10 spatial extents. Just as the correlation coefficients, one heatwave day or a complete heatwave week generally give the same results.

In figure 4.23 the scatterplots between the minimum and mean temperature and PLAND, AREA_MN and SHAPE_MN are shown, they present the most important patterns described below.

Figures 8.8, 8.14, 8.18, 8.26 and 8.32 show only a small range for PD values. As a consequence, no clear relationship between PD and urban green is found, this is in concordance with the insignificant correlation coefficients obtained before. An in-depth investigation of the other scatterplots shows that all T/RH variables have the same patterns for night-time. During the night low green's PLAND has a negative relation with the T/RH variables for all extents, high green only in the 500m buffer. The same patterns are visible for LPI. ED shows for both green types only negative relations within the median buffer zones. For low green both AREA_MN and SHAPE_MN show negative relationships for all extents, for high green this relationship in only visible in the larger buffer zones. Differences in low green's landscape metrics results in a maximum temperature difference of 3-4.5°C. Within the 500m buffer differences in high green's landscape metrics result in a maximum temperature difference of 2.5-3°C at night.

The minimum temperature gives similar day and night results for all landscape metrics. The other variables (max, mean, sum temperature and DI) have however a different pattern for daytime, this daytime pattern is nonetheless the same for all. During daytime low green's PLAND is neutral for all extents, while high green shows negative relationships for buffers ≥ 50/80m. These patterns are again true for LPI. ED shows neutral relationships with T/RH variables both low ang high green. The AREA_MN shows the same results as PLAND, this landscape metrics is neutral for all extents of low green and shows negative relationships for buffers ≥ 50/80m for high green. SHAPE_MN shows small negative relationships for both low

and high green at buffers ≥ 80m. During the day, differences in high green's landscape metrics give a maximum temperature difference of 1-2°C.

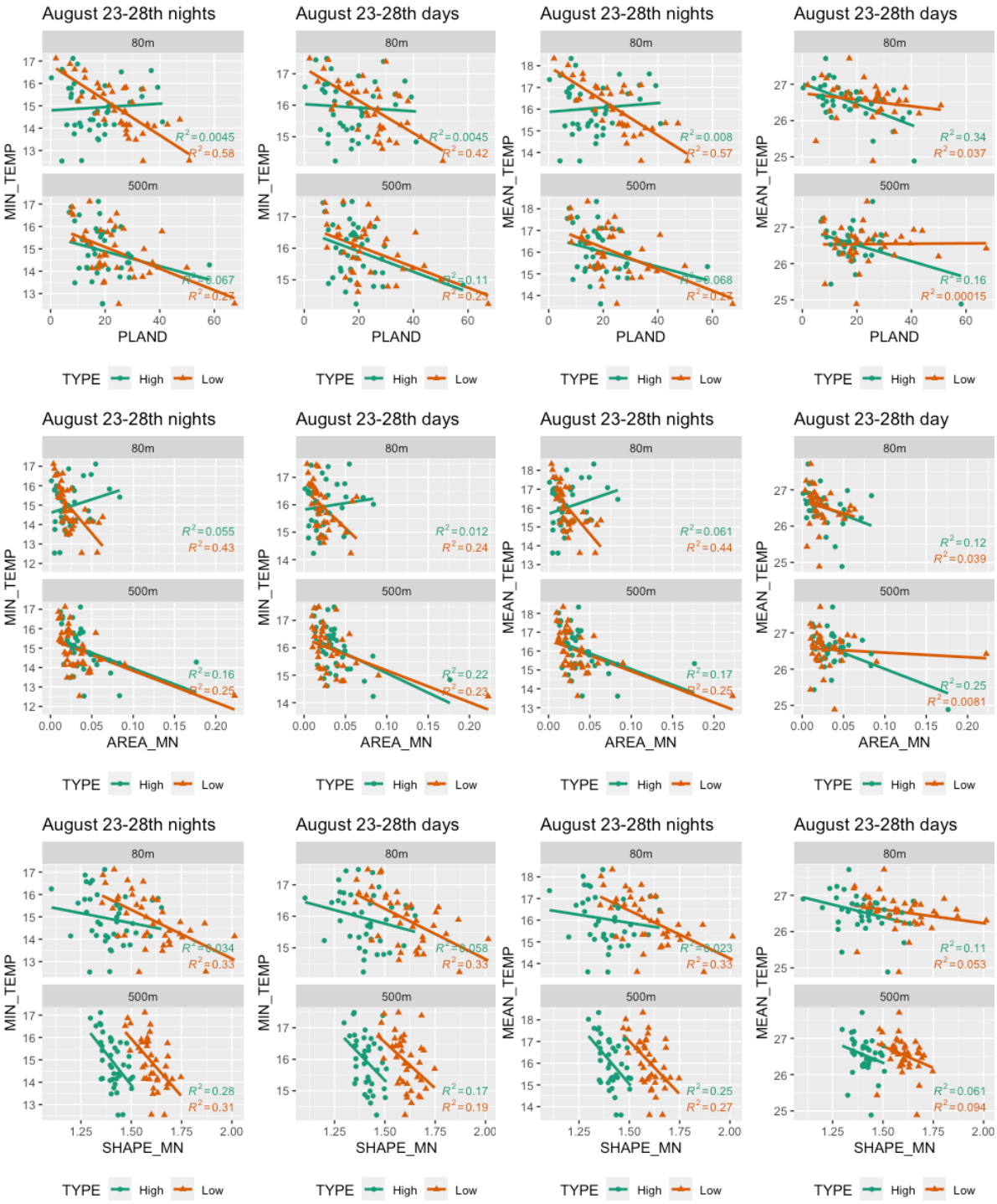

Figure 4.23: Scatterplots between minimum (left) and mean temperature (right) and the percentage cover, mean patch size and mean shape index of high and low green for two spatial (80m and 500m) and two temporal scales (August 23-28th nights/days).

5 Discussion

5.1 Sampling design

The sampling design has no optimal distribution among the LCZ classes, stations are especially lacking in areas defined by a high building height (1xx) and/or a high building density (x1x) in combination with a high vegetation cover (xx1). Quite logically, these classes were uncommon within the study area. To ensure that enough stations are installed within the vicinity of a high vegetation cover, we should have installed an additional amount of stations within the low building height, low building density and high vegetation cover (221) LCZ class. If the sampling design can be updated for further research, this needs to be taken into account.

We mentioned before that public stations are installed at a height of 3-4m compared to the 2m standard height in private gardens. No direct effects of this height difference were noticed but additional research is needed to confirm that the difference creates no offset in observed meteorological parameters.

5.2 Urban air temperature (UAT)

5.2.1 Data quality analysis

Basic statistics show that the reference station GarmonR01 on average overestimates the temperature, shown by a mean temperature bias of 0.08°C. The measurements show a weak accuracy, indicated by a standard deviation of 0.61°C (figure 4.2 top). The temperature bias between GarmonR01 and the official RMI station (figure 4.2 bottom) shows a positive bias (0.36°C) during daytime and a negative bias (-0.17°C) during night-time. This indicates that the low-cost weather station has a tendency to overestimate temperatures by an average 0.36°C during daytime and underestimate temperatures by an average -0.17°C during night-time. We further know that the uncertainty of the measurements is higher during daytime (0.66°C) than nighttime (0.44°C) (figure 4.2 bottom). The positive temperature bias during daytime can be explained by the lack of active ventilation in the low-cost weather stations (Conrad, 2019; Renkforce, n.d.). The weather stations have a radiation shield which should guard the thermometer from direct sunlight (Conrad, 2019; Renkforce, n.d.), but previous research has shown that not all shields are equally effective (Bell et al., 2015). Under sunny conditions this

radiation shield is prone to overheating, hereby warming up the air inside, which will result in higher sensed temperatures.

We could apply a simple regression technique to correct the temperature measurements of GarmonR01 with the reference values of the official RMI station. This would shift the mean temperature bias to zero, but the standard deviation of the error would remain high. However, a simple regression does not fit our needs since the bias between both stations is not constant (figure 4.3, day/night factor) and seems to vary according to other variables (figure 4.4, radiation and windspeed).These fluctuations of the bias indicate that the station is not just incorrectly calibrated, poor ventilation and siting will probably play a major role (Bell et al., 2013). The higher positive temperature biases during daytime and summer are intuitively related with extended hours of solar radiation (figure 4.3). This hypothesis is confirmed when the impacts of radiation and windspeed are taken into account (figure 4.4), the highest temperature biases occur under intense solar radiation in combination with low wind speed. These findings are confirmed by previous research (Bell et al., 2015; Jenkins, 2014).

To maximally reduce the standard deviation error and ultimately build a predictor for the temperature bias, we correlated the bias with other observations from the GarmonR01 station (table 4.2). This analysis indicates that high observations of past radiations and temperature will positively influence the temperature bias, while high humidity observations will have a negative effect on the temperature bias. Intuitively we would expect a negative correlation coefficient for wind speed, the slightly positive correlation coefficient could be explained by the limited number of observations for high windspeed (figure 8.4). Using a simple linear regression with the past radiations only is already sufficient to suppress the mean temperature bias and results in an RMSE of 0.46 (figure 4.5 b). Adding additional variables to the model, such as wind speed, humidity or both is statistically significant but only decreases the RMSE by one percentage (figure 4.5 c/d/e). These simple multivariate regression models using past radiation observations were previously mentioned in the literature as correction models (Bell et al., 2015). The random forest model including temperature, dew point temperature, humidity, radiation, radiation60, windspeed, month and hour results in an RMSE of 0.29 and R^2 of 0.76 (figure 4.5 f), indicating a better precision and more robust model. As a disadvantage, this model has a longer computation time and lacks interpretability at the end, additional tests are needed to determine the most important variables.

When validating the transferability of the random forest model to other Garmon stations and thus other locations the results are not optimal. For GarmonR02 we see a reduction of the standard deviation from 0.41 to 0.28, indicating a higher accuracy for the corrected temperatures. The mean temperature bias has however increased from 0.09 to 0.15, which could be explained by the offset in meteorological observations between both stations. Even though GarmonR01 and GarmonR02 are installed on the same location with a distance of only one meter, a shift in the measured variables is noticed (figure 8.1 and 8.2). The fact that the stations were bought one year from each other and are probably from a different production batch could be a potential explanation. The unexpected results for GarmonR03 and GarmonR04 can be explained by the small dataset, both stations were only installed in November 2019 and have yet to experience the warmer summer months. A possible solution would be to incorporate the data of all four reference stations into the random forest model, the expected results would be worse for GarmonR01 but better for the other stations within the Garmon network. Or if you are only interested in heatwaves, you could build a random forest model solely trained for heatwave data. Additional research is needs to investigate these hypotheses. If you would only be interested in night temperatures, you could consider using the original (uncorrected) night time temperature measurements which show only small temperature biases. Because we wanted to look at both the day and night UHIs, we used to random forest predictor model to calculate corrected temperatures for each station in function of its local climatic conditions.

5.2.2 Spatio-temporal maps of Leuven's UHI

Since all temporal scales – i.e. one heatwave day, a complete heatwave week and the five hottest days during the measuring period - show similar patterns for the different quantitative temperature (and humidity) variables, we may conclude that the observed patterns are not just incidental and can be trusted as general patterns. Future research using a larger and more complete dataset, including additional summer months and associated heatwaves, can confirm this theory.

Diurnal variations of UHIs

When the absolute minimum (figure 4.8) and absolute maximum temperatures (figure 4.10) in summer time are compared, we notice a higher UHI intensity for minimum temperatures compared to maximum temperatures. The minimum temperatures show a UHI intensity ranging over 5°C between the hottest and coolest station and indicate a gradual decrease in minimum

temperature from the urban region towards their suburban and more natural surroundings. The maximum temperatures show a range of only 2.3°C and do not show the same gradual decrease, both the hottest and coolest station are located within the city centre. The literature generally confirms our findings by reporting higher UHI intensities during the solar off-peak time (i.e. when solar radiation is not the dominant source of heating; night-time or early morning) (Memon et al., 2009; U.S. EPA, 2008). The U.S. EPA (2008) describes daytime UHI intensities between -1 to 3°C, while night-time intensities can range between 7 to 12°C. These values are in concordance with previous studies in Europe showing UHI intensities fluctuating between 2.6 and 12 °C (Memon et al. , 2009). When comparing urban locations to a rural reference site in Rotterdam, The Netherlands, van Hove et al. (2015) found a larger temperature difference between both sites for minimum temperatures (0.5 to 2.6 °C) compared to maximum temperatures (-0.1 to 1.3 °C). A similar study in Basel, Switzerland from 2002 reported a difference of 5°C at night, during the day the UHI intensity reached a maximum of only 2°C (Hamdi & Schayes, 2008).

When these absolute minimum (figure 4.8) and maximum temperatures (figure 4.10) are related to night and day temperatures respectively, these findings can be explained by the diurnal variations of UHIs. Previous research has shown that the UHI is often weak in the morning but further develops during the day as the build environment absorbs solar radiance (Bassett et al., 2016; van Hove et al., 2015). During night-time subsequent heat release takes place. Because the urban environment is characterized by a reduced longwave radiation loss and lower albedo, the cooling of cities will be delayed compared to their rural surroundings, resulting in a maximum UHI intensity at night (Bassett et al., 2016; Hamdi & Schayes, 2008; Nichol et al., 2009; U.S. EPA, 2008). As previously stated, this phenomenon is typical for atmospheric UHIs, while the opposite is true for surface UHIs (Oke, 1995; Roth et al., 1989; Zhou et al., 2011). The temporal temperature profile (figure 4.11), which compares a rural and urban station with the mean temperature of all stations, follows this diurnal pattern. The profile shows a weak UHI in the morning and during the day, only after sunrise a clear temperature difference between the city and its rural surroundings is obtained.

To summarize the results of the temporal temperature profiles for all stations, we calculated the differences between the temperature of a specific station and the mean temperature of all stations for every timestep (every 10 minutes). By summing this difference over all timesteps and dividing this sum with the number of timesteps, you obtain a mean temperature difference

between a specific station and the mean of all stations. The mean temperature differences over day- (figure 4.13) and night-time (figure 4.12) in summer further confirm our previous statement that the maximum UHI intensity is reached at night. At daytime the mean difference between the coldest and hottest station only covers 1.8°C, while a range of 5.2°C is found for one night. Also the distribution of the cooler and hotter stations seems more random during the day (figure 4.13) than night (figure 4.12).

Seasonal variations of UHIs

The minimum temperatures in wintertime (figure 4.9) show a similar UHI intensity compared to those in summertime (figure 4.8) indicated by a range of 4.7°C and 5.5°C between the hottest and coldest station respectively. For the mean temperature difference, summer time (figure 4.12) shows a higher UHI intensity (5.2°C) than winter (4.0°C) (figure 4.14). In contradiction with our results, Sheng et al., (2017) found more extreme UHI intensities in winter compared to summer when comparing the hottest and coldest station. The gradual decrease in temperatures starting in the city centre towards the sub-urban regions is however very clear during winter (figure 4.9 and figure 4.14). Only the city centre of Leuven has minimum temperatures above freezing point, outside the ring road no values above zero are measured. This can be explained by the installation of extra stations within the city centre during autumn 2019. The fact that such a UHI can also be observed during wintertime is however confirmed by the literature. Some studies even suggest that atmospheric UHIs are more intense during wintertime, while surface UHIs are more severe during summer time (Roth et al., 1989; Sheng et al., 2017; U.S. EPA, 2008).We cannot confirm this theory at this time due to the different number of installed weather stations and limited number of observations, but it would be an interesting focus for future research.

Diurnal variations of Thom's discomfort index

The Thom's discomfort index is based on both temperature and relative humidity measurements and gives an idea of the thermal discomfort people encounter (Thom, 1959). The mean temperature and mean relative humidity used to calculate the discomfort index (figure 4.15) tells us that high discomfort indexes are related to high temperature and low humidity measurements. The formula of the Thom's discomfort index however indicates that both temperature and relative humidity will have a positive effect on the resulting DI values. Since a station with a high temperature, but low relative humidity value gives a high discomfort index, we can conclude that the resulting DI values in and around Leuven are mainly driven by the

temperature values. The inverse pattern of temperature and humidity observations is quite intuitively. Since relative humidity measures the amount of water vapor in the air relative to the air temperature, the humidity will decrease as the air temperature increases while the amount of water vapour stays constant (Britannica Online Academic Edition, 2020).

The DI values for one heatwave day or a complete heatwave week found during night-time (figure 4.15 left/center) all remain below 21, indicating people do not encounter any discomfort. The DI values in the city centre are however higher, indicating relative more discomfort within the city centre compared to sub-urban regions. For the five hottest days, three urban stations do obtain values above 21, indicating discomfort expressed by <50% of the population. During daytime (figure 4.17) more discomfort is present. For one heatwave day or a complete heatwave discomfort is expressed by < 50% of the population. For the five hottest days during the measuring period discomfort is expressed by > 50% of the population. More extreme values were found during the period 2001-2010 in Athens. During all heatwave days no values below 27 were found, indicating that most of the population suffered discomfort. For 54% of the heatwave days, the citizens even felt severe heatwave stress, indicated by DI values between 29 and 32 (Papanastasiou et al., 2015). Because both urban and sub-urban regions in Leuven fall within the same range of discomfort feelings, no clear conclusion between different locations can be made. In concordance with the temperature variables discussed in the previous paragraphs, a larger range of DI and clearer decrease in DI from urban to sub-urban regions is found during night-time compared to daytime. Again, leading us to conclude that the UHI intensity is higher during night time.

Limitations and suggestions for further research

In this thesis no statistical tests were performed to confirm the existence of an urban heat island in Leuven, the UHI maps (figure 4.9 – 4.17) do however suggest such a phenomenon. Future research can use the predefined local climate zone classes to check whether a significant difference in air temperatures exists for weather stations installed in a high/low building height, high/low building density and high/medium/low vegetation cover context.

5.3 Urban green infrastructure (UGI)

5.3.1 Green map of Leuven's UGI

The confusion matrix (table 4.6) of the urban green map indicates a high overall accuracy of 91.25% and Kappa head of 0.862. High green is the best classified landcover indicated by the highest producer's (91.91%) and user's accuracy (91.74%) but is closely followed by low green (91.72% and 91.01%) and other (88.84% and 90.65%). These values are in accordance with the literature (Myint et al., 2014; Zhou et al. , 2009). Zhou et al. (2009) compared three methods to classify the landcover in Baltimore County. Their first method mostly resembles our methodology. They first segment the image into objects of homogeneous pixels using a scale parameter of 20, color and shape weight of 0.9/0.1 and equal weights for compactness and smoothness (0.05), the following image classification first separates shaded from non-shaded objects, eventually resulting in an overall accuracy of 81.5% and Kappa head of 0.74. High green resulted in the best producer's and second-best user's accuracy.

Previous papers have stated the importance of separating the classification of shaded and non-shaded areas. This is needed because high spatial resolution imagery is frequently affected by shadows, especially in urban environments with variations in surface elevation (Zhou et al., 2009). Apart from classifying the shaded areas using spatial information, you could use multisource data fusion to aid the classification of shaded areas which has shown promising results in the past (Zhou et al., 2009). The fact that the spectral images and LiDAR data used in the creation of the urban green map are acquired in different years (2019 and 2015) could result in sub-optimal classification results. Our accuracy assessment however indicates that this does not cause too much problems.

5.3.2 Spatial patterns of Leuven's UGI

Even though the green map has a high overall accuracy (91.25%), we should note that this accuracy is calculated for the entire green map, which covers an extent of 6556m to 10790m. Needless to say the overall accuracy will decrease when looking at the smallest buffer region and further increase for larger buffer zones. We can thus state that the resulting values of the landscape metrics within the smallest buffer will probably be less accurate compared to those in the larger buffer zones. A possible solution could be to directly calculate the metrics from the inventory data collected around each weather station. This possibility was examined but

excluded from this thesis due to insufficient quantity of the inventory data. Because the inventories were digitalized using low resolution orthophotos, only landcover patches that could be identified correctly were included. This methodology resulted in smaller patches not covering the entire 10m buffer around every station. Further research is thus needed to confirm this hypothesis.

Following the station's guidelines, weather stations were never installed underneath or in the near vicinity of trees, which probably explains the low percentage (PLAND) of high green in the smallest buffers (figure 4.18). Additionally, the LCZ classes with a high vegetation cover were highly under sampled (see table 4.1 and section 5.1). As the buffers increase, more high green is found. The right skewed data distribution indicates that only a few stations are surrounded by a high green cover > 50%, the majority is not. The highest percentage cover (PLAND) of low green in the 10m buffer can be explained by the fact that most stations are installed in gardens, as the buffers increase respectively more sealed surfaces (housing, road infrastructure, …) appear. The largest patch index (LPI) gives the percentage cover of only the largest patch and is thus a measure of dominance (McGarigal et al., 2002). The LPI is always smaller or equal to the PLAND. When these metrics equals percentage cover of a certain land cover type, we know that the landscape only contains one patch of this land cover type (McGarigal et al., 2002). The growing LPI for high green and declining one for low green for increasing buffers have the same explanation as above. The patch density (PD) equals the number of patches of a certain patch type divided by the total landscape area and is thus constraint by cell size of the green map (McGarigal et al., 2002), in our case 1mx1m. There can only be as many patches as there are cells within the raster image. The high PD in the 10m buffer indicates a fragmented landscape, which seems logical for individual gardens. As the buffers increase the number of patches decreases while the area increases, resulting in a strong decrease in PD. Looking at larger buffers will thus result in a less fragmented landscape. The edge density (ED) presents the sum of lengths of all edge segments divided by the total landscape area and can grow without limit. ED can be zero when there is no class edge in the landscape (McGarigal et al., 2002). Just as for PD, the large ED in the smaller buffer zones indicate a fragmented landscape. Based on both PD and ED, we can say that low green is more fragmented compared to high green in all buffer zones. Within the smaller buffers (10m- 50m) the mean patch size (AREA_MN) of high green is lower than low green, for larger buffers (80m-500m) the opposite is true. These results are in concordance with those for the percentage cover and largest patch index. The mean shape index (SHAPE_MN) shows irregular results for

the 10m-80m buffers, indicating both irregular and complex (SHAPE_MN > 1) and square-like simple (SHAPE_MN = 1) patches for low and high green, above 80m a constant value is kept. The mean shape index is related to the edge density, since more irregular patches will have larger edge densities, this relation is visible in figure 4.18.

5.4 Relation between UAT and UGI

5.4.1 Spearman correlation matrix and simple linear regression models

Generally speaking, we can see that the impacts of the urban green infrastructure on urban air temperatures follow the same patterns for one heatwave day (figure 4.19) or one heatwave week (figure 4.20), indicating that the results are not incidental but rather show a general pattern. The same is true for the discomfort index (figure 4.21). The scatterplots in figures 8.5 to 8.34 further confirm this hypothesis.

Mitigating effects of urban green's composition and configuration

The correlation matrices (figures 4.19 - 4.21) and the scatterplots (figures 8.5 - 8.34) presenting the relationship between temperature/humidity variables and landscape metrics of urban green indicate that both composition and configuration of urban green matter in the mitigation of urban heat islands. Not only a bigger percentage cover of urban green but also a larger size and more complex shape of urban green patches will significantly lower urban air temperatures and subsequently mitigate heat stress. This can be explained by the fact that an increased edge density and shape complexity of urban green will increase shade and enhance the interaction between urban green and the build-up area, hereby influencing the flow of energy between these land cover features (Zhou et al, 2011). The negative correlations obtained over multiple extents suggest that increasing the percentage cover (PLAND), largest patch index (LPI), edge density (ED), mean patch size (AREA_MN) and mean shape index (SHAPE_MN) of urban green will all result in lower air temperatures and discomfort indexes. The correlations show that percentage cover (-0.30 to -0.76) is the most important landscape metrics but is closely followed by mean patch size (-0.27 to -0.77) and largest patch index (-0.28 to 0.74) (figures 4.19 - 4.21). The insignificant and positive correlations for patch density (PD) could be due to the small range of possible PD values found around the stations.

The fact that not only the composition but also the configuration of urban green matters in the mitigation of heat was already regularly found for studies focussing on the effect of UGI on

LST (e.g. Connors et al., 2013; Li et al., 2013; Zhou et al., 2011, 2017) but only more recently a study focussing on air temperatures (e.g. Qian et al., 2018) obtained the same conclusion. Also the relative importance of different landscape metrics found here is consistent with the literature (Li et al., 2013; Rhee et al., 2014; Zhou et al., 2011; Zhou et al., 2017). Li et al. (2013) found negative correlation coefficients between LST and PLAND, AREA_MN and SHAPE_MN ranging between -0.70 and -0.41. Zhou et al. (2011, 2017) obtained negative correlations between LST and all landscape metrics except for PD. The correlations between air temperatures and landscape metrics found in the past are however less significant and no correlations for PD and SHAPE_MN were found (Qian et al.,2018).

Multiple studies state that configuration metrics can be highly correlated with composition metrics or the percentage cover of urban green (Qian et al., 2018; Zhou et al., 2011). To make sure no incorrect relationships are found, it is important to control for the effects of urban green's percentage cover when quantifying the effects of the spatial configuration of urban green on air temperatures (Qian et al., 2018; Zhou et al., 2011, 2017). In the future the correlation between all landscape metrics should be checked. If needed, a partial correlation analysis, using PLAND as the controlled variable, should be performed to make sure no spurious relationships are found (Qian et al., 2018).

Different effects of urban green for different T/RH variables

During night-time all temperature and relative humidity variables - minimum temperature, maximum temperature, mean temperature, temperature sum and the discomfort index - show the same relations between T/RH variables and the landscape metrics of high and low green. During daytime both minimum and maximum temperatures show different results compared to the similar patterns of the mean temperature, temperature sum and discomfort index (figures 4.19 - 4.20 right). This can be explained by the fact that minimum day temperatures are highly affected by the definition of daytime. Because no absolute minimum temperature is reached during the day, new minimum variables are found when this timeframe is extended, which makes these results not easy to interpret. The high amount of insignificant correlations for the maximum day temperature can be linked to section 5.1.2. Here we discussed that absolute maximum temperatures show only a limited temperature range, not indicating a clear UHI. These similar air temperatures would not able to explain the variations in urban green.

Diurnal variations of the effects of low and high green on T/RH variables

During night-time the percentage cover, largest patch index, mean patch size and mean shape index of low green show a negative relation with all T/RH variables for all extents, indicating that an increased relative and absolute patch size as well as a more irregular shaped patch of low green will decrease urban air temperatures. To illustrate, an increase in percentage cover of 50% will lower minimum and mean temperature by 4°C (figure 4.23). The negative correlations between low green's landscape metrics and air temperature range from -0.4 to -0.76 (figures 4.19 and 4.20). For high green these negative relationships are only found within the largest extent (500m) and they are less extreme. An increase of high green's percentage of 50% cover will reduce minimum and mean temperatures by only 2°C (figure 4.23), correlations ranges from -0.27 to -0.52 (figures 4.19 and 4.20). The other buffer zones result in a neutral relationship. During daytime a different pattern is found. Now high green shows negative relations between percentage cover, largest patch index, mean patch size and mean shape index and the maximum temperature, mean temperature, temperature sum and the discomfort index for buffers ≥ 50/80m, while low green shows a neutral relationship for all extents. The same increase in percentage cover (50%), gives a temperature decrease of only 1.5°C during daytime (figure 4.23). Correlations between high green's landscape metrics range from -0.28 to -0.50 (figures 4.19 and 4.20). Based on these results we can conclude that high and low green have different mitigating effects during day and night. The differences in spatial extents will be discussed further on.

These findings were also confirmed by the literature (Yan & Dong, 2015; Yan et al., 2014). Yan et al. (2014) obtained no significant correlations for the percentage cover of low green during daytime, while negative correlations (-0.604 to -0.401) for high green were found in buffers ≤ 50m and ≥ 150m. Yan & Dong (2015) used simple regressions to present the relation between air temperature and tree and lawn cover at day and night. During the day, tree cover showed a small negative relation (-0.026) with air temperature, while lawn cover resulted in a neutral relationship. The opposite pattern was true for night-time (-0.056 for lawn cover) (Yan & Dong 2015).

Hamada & Ohta (2010) have previously suggested that the cooling processes can differ for day and night. During night-time differences in the sky view factor and thermal properties regarding heat storage are important factors in the cooling process, while differences in radiation and evapotranspiration cause the differences in cooling during the day (Hamada et al., 2010). These

suggestions are line with our results. Low green has a high albedo, low specific heat capacity and high sky view factor, leading to an effortless heat loss at night. High green, on the other hand, also has a high albedo and low specific heat capacity but has a limited sky view factor which reduces the longwave radiation loss at night. Because of this low green could potentially be more effective in mitigating heat at night. During the day the canopy of high green will intercept the incoming solar radiation, a process known as the shading effect, hereby directly cooling its environment. Because of its smaller volume, the shading effect of low green is however smaller, as a consequence these areas are constantly exposed to higher solar radiation. We additionally know that trees show a higher evaporation efficiency than grass, especially during summer (Satchithanantham et al., 2017; Stan et al., 2014). High green could thus be the more effective tool for heat mitigation during daytime. The literature confirms that both individual trees (Georgi & Zafiriadis, 2006) and clusters of trees (Cohen et al., 2012; Streiling & Matzarakis, 2003) will lower air temperatures during the day, here the specific amount of shading was an important cooling factor (Shashua-Bar & Hoffman, 2000). Other studies however demonstrate that tree canopies can retain heat at night (Bowler et al., 2010; Huang et al., 2008).

Both the correlation matrices as the scatterplots indicate that low green has a higher mitigating effect than high green. This is shown by the more negative correlation coefficients (figure 4.19 - 4.21) and higher R^2 values (figure 4.23) for night-time low green compared to daytime high green. This result is however contradicted by the literature (Rushayati et al., 2018; Yan et al., 2014). A possible explanation for this result could be the relatively smaller range of high green's landscape metrics, due to the under sampling in the high vegetation cover LCZ classes (see section 5.1). Especially in the smaller buffer zones, where the direct cooling effects of shading and evapotranspiration of high green are most important (Yan et al., 2014), we see an under sampling of locations with lots of high green. This is due to the fact that stations were never installed underneath or in the near vicinity of trees (see section 5.3.2).

As stated in the materials and methods section, no relation between winter air temperatures and urban green's composition and configuration is presented here. This would however be an interesting perspective for further research since other studies have shown that both the effective radii at which UGI patterns affect air temperatures (Qian et al., 2018) and the relative importance of high and low green (Cohen et al., 2012; Yan et al., 2014) vary by season .

Spatial variations of the effects of low and high green on T/RH variables

At night the mitigation impact of low green is highest within the 20m and the 50m to 180m buffer zones (figure 4.20). Yang (2014) found a contrasting result, here the 300m buffer showed the highest mitigating effects. During night-time high green shows negative relations with temperature variables and discomfort index for the 500m buffer only (figure 4.20). This leads to the suspicion that high green could potentially be more significant at larger scales (> 500m). High green at larger extents could consist of more closed dense forests ecosystems instead of solitary street trees. This should be visible by a high percentage cover, high largest patch index, high mean patch size and low patch density within the large extents. Such a dense forest cover has a high albedo and low specific heat capacity, lowering the amount of solar radiation captured during daytime, which will in turn result in a more efficient heat loss and lower air temperatures at night. Previous research has also shown that there is a positive relation between the area of a greenspace and its cooling effect into the surrounding areas (Shashua-Bar & Hoffman, 2000; Yan et al., 2014), studies have shown that these cooling effects can extend for several hundred meters (Hamada & Ohta, 2010). When these forest ecosystems have an irregular shape (high mean shape index), these cooling effects are even further extended (Zhou et al, 2011). We should highlight that this is just a hypothesis, further research using larger buffer zones is needed to confirm this theory.

During the day, the 50m to 130m buffers show the highest mitigating impacts of high green, the mitigating impacts of low green are minimal for all extents. These findings are partly contradicted by the literature. We already stated that low green has no significant impact during the day (Yan & Dong, 2015; Yan et al., 2014), but the most significant buffers for high green obtained here are not as easy to interpret. Since the influence of tree canopy shading and evapotranspiration are the most important factors during daytime (Hamada & Ohta, 2010), we would expect the highest relation between air temperature and high green within the smallest buffer zone. A possible explanation is again the fact that stations were not installed in the near vicinity of trees, resulting in a low range of possible landscape metric values for the smaller extents.

Importance of environmental variables

Even though our temperature bias correction model is used to correct for incorrect calibrations, poor ventilation and siting in general, we still expect that environmental variables could influence the air temperature measurements.

During daytime, area and perimeter are crucial environmental factors for the maximum temperature, mean temperature, temperature sum and discomfort index (figure 4.22). A bigger area and larger perimeter will lower air temperatures and decrease human heat stress. The insignificant results for minimum temperatures could be due to the fact that minimum day temperatures are highly affected by the definition of daytime, as explained before. The insignificant results for the sky view factor (SVF) are however unexpected and not as easy to interpret. SVF is closely related to both the incoming solar radiation during the day and the long wave radiation loss at night and could thus have sincere impacts on day and night air temperatures.

The fact that the environmental variables are crucial parameters during daytime rather than night-time is a bit surprising. Area, perimeter, compactness and SVF all say something about the enclosure of the weather stations, which has important consequences for the longwave radiation loss at night-time. This suggest that other factors are at stake. Previous research mentions orientation as an important factor which could affect air temperatures, solar exposure and ventilations conditions (Oliveira et al., 2011). The importance of considering such confounding variables, either by correcting the temperature measurements or by incorporating them into the model, has been stated by the literature (Bowler et al., 2010; Oliveira et al., 2011). Not incorporating these variables could bias the result of the cooling potential of urban green (Bowler et al., 2010).

Limitations and suggestions for further research

The correlation matrices and simple regression models used to estimate the relationship between air temperatures and the composition and configuration of urban green only portray the bivariate relation between air temperature and a specific composition or configuration metric.The use of a stepwise multiple regression analysis (Yan et al., 2014) or multiple linear regression incorporating different combinations of only composition/configuration metrics or a combination of both (Zhou et al., 2011) is recommended for further research. These models can be used to describe air temperature as a combination of different landscape metrics at different temporal and spatial scales.

In this thesis the relation between urban green and air temperatures was investigated for all weather stations together. We now have a general idea of the amount, shape and type of urban green needed to lower urban air temperatures and mitigate heat stress. We did not make a

distinction between urban or rural stations and can thus not answer questions regarding the ideal composition and configuration of urban green needed to mitigate heat in an urban or rural context. Further research can use the predefined local climate zone classes to assess the mitigating impacts of urban green for these contexts separately.

6 Conclusion

This thesis studied the spatio-temporal variations of urban air temperature and the Thom's discomfort index in and around Leuven. Subsequently, the impact of urban green's composition and configuration on air temperature and human discomfort were examined for multiple spatial and temporal scales.

The urban heat island and related human discomfort during the 2019 heatwaves showed clear diurnal variations for multiple temporal scales. At night, higher urban heat island intensities, defined as the temperature difference between the hottest and coldest stations, and larger ranges in discomfort index values were found than during daytime.

We additionally found that both composition and configuration of high and low green matter in the mitigation of urban heat islands. Not only a bigger percentage cover of high and low green but also a larger size and more complex shape of these urban green patches will significantly lower urban air temperatures and subsequently mitigate heat stress. This mitigating impact of different urban green types, high and low green, did however vary for different spatial and temporal scales. At night, the composition and spatial configuration of low green was found to be the most important mitigating factor along all spatial extents. This can be explained by its thermal properties and high sky view factor, which both favour longwave radiation loss at night. Increasing low green's percentage cover by 50%, lowers night-time temperatures with 4°C. During daytime, high green was more effective in reducing urban air temperatures and human discomfort through direct shading and evapotranspiration. The resulting temperature decrease was however smaller, a 50% increase in high green's percentage cover decreased air temperature with only 2°C.

These outcomes have important implications for urban green planning and design. In order to ameliorate the outdoor thermal environment within urban centres, planners and designers must consider both the composition and the spatial configuration of the urban green infrastructure. Different urban green types, shapes and sizes at multiple spatial scales are needed to improve thermal comfort of citizens during both night and day.

7 References

Agentschap Informatie Vlaanderen. (2019a). Bodembedekkingskaart (BBK), 1m resolutie, opname 2015. Retrieved April 4, 2020, from http://www.geopunt.be/catalogus/datasetfolder/0230a22f-51c0-4aa5-bb5d-0d7eeeaf0ce8

Agentschap Informatie Vlaanderen. (2019b). Voorlopig referentiebestand gemeentegrenzen, toestand 16/05/2018 (geldig vanaf 01/01/2019). Retrieved December 27, 2019, from http://www.geopunt.be/catalogus/datasetfolder/9ff44cc4-5f16-4507-81a6-6810958b14df

Agentschap voor Natuur en Bos. (2013). Groenkaart Vlaanderen 2012. Retrieved April 17, 2020, from http://www.geopunt.be/catalogus/datasetfolder/a0472f3b-0927-42f5-909b-c765a4fa4721

Airbus Defence & Space Intelligence. (2013). Pléiades: Spot the Detail. Retrieved April 8, 2019, from https://www.intelligence-airbusds.com/files/pmedia/public/r49228_9_pleiades_product.pdf

Airbus Defence & Space Intelligence. (2019). Pleiades-1B Satellite Sensor (0.5m). Retrieved December 28, 2019, from https://www.satimagingcorp.com/satellite-sensors/pleiades-1b/

Arnfield, A. J. (2003). Two decades of urban climate research: A review of turbulence, exchanges of energy and water, and the urban heat island. *International Journal of Climatology*, *23*(1), 1–26. https://doi.org/10.1002/joc.859

Astrium. (2012). Pléiades Imagery User Guide. Retrieved April 8, 2019, from http://satimagingcorp.s3.amazonaws.com/site/pdf/User_Guide_Pleiades.pdf

Bassett, R., Cai, X., Chapman, L., Heaviside, C., Thornes, J. E., Muller, C. L., Warren, E. L. (2016). Observations of urban heat island advection from a high-density monitoring network. *Quarterly Journal of the Royal Meteorological Society*, *142*(699), 2434–2441. https://doi.org/10.1002/qj.2836

Bell, S., Cornford, D., & Bastin, L. (2013). The state of automated amateur weather observations. *Weather*, *68*(2), 36–41. https://doi.org/10.1002/wea.1980

Bell, S., Cornford, D., & Bastin, L. (2015). How good are citizen weather stations? Addressing a biased opinion. *Weather*, *70*(3), 75–84. https://doi.org/10.1002/wea.2316

Benz, U. C., Hofmann, P., Willhauck, G., Lingenfelder, I., & Heynen, M. (2004). Multi-resolution, object-oriented fuzzy analysis of remote sensing data for GIS-ready information. *ISPRS Journal of Photogrammetry and Remote Sensing*, *58*(3–4), 239–258. https://doi.org/10.1016/j.isprsjprs.2003.10.002

Bevolkingsregister Stad Leuven. (2020). Demografie. Retrieved March 22, 2020, from https://leuven.incijfers.be/dashboard

Blaschke, T. (2010). Object based image analysis for remote sensing. *ISPRS Journal of Photogrammetry and Remote Sensing*, *65*(1), 2–16. https://doi.org/10.1016/j.isprsjprs.2009.06.004

Bowler, D. E., Buyung-Ali, L., Knight, T. M., & Pullin, A. S. (2010). Urban greening to cool towns and cities: A systematic review of the empirical evidence. *Landscape and Urban Planning*, *97*(3), 147–155. https://doi.org/10.1016/j.landurbplan.2010.05.006

Britannica Online Academic Edition. (2020). Relative humidity. Encyclopædia Britannica, Inc.

Cao, X., Onishi, A., Chen, J., & Imura, H. (2010). Quantifying the cool island intensity of

urban parks using ASTER and IKONOS data. *Landscape and Urban Planning*, *96*(4), 224–231. https://doi.org/10.1016/j.landurbplan.2010.03.008

Cohen, P., Potchter, O., & Matzarakis, A. (2012). Daily and seasonal climatic conditions of green urban open spaces in the Mediterranean climate and their impact on human comfort. *Building and Environment*, *51*, 285–295. https://doi.org/10.1016/j.buildenv.2011.11.020

Connors, J. P., Galletti, C. S., & Chow, W. T. L. (2013). Landscape configuration and urban heat island effects: Assessing the relationship between landscape characteristics and land surface temperature in Phoenix, Arizona. *Landscape Ecology*, *28*(2), 271–283. https://doi.org/10.1007/s10980-012-9833-1

Conrad. (2019). Renkforce WH2600 Digitaal draadloos weerstation Voorspelling voor 12 tot 24 uur. Retrieved December 28, 2019, from https://www.conrad.nl/p/renkforce-wh2600-digitaal-draadloos-weerstation-voorspelling-voor-12-tot-24-uur-1267654

Conrad, O. (2008). Module Sky View Factor. Retrieved from http://www.saga-gis.org/saga_tool_doc/2.2.0/ta_lighting_3.html

Degerickx, J., Roberts, D. A., McFadden, J. P., Hermy, M., & Somers, B. (2018). Urban tree health assessment using airborne hyperspectral and LiDAR imagery. *International Journal of Applied Earth Observation and Geoinformation*, *73*, 26–38. https://doi.org/10.1016/j.jag.2018.05.021

Dirksen, M., Ronda, R. J., Theeuwes, N. E., & Pagani, G. A. (2019). Sky view factor calculations and its application in urban heat island studies. *Urban Climate*, *30*, 100498. https://doi.org/10.1016/j.uclim.2019.100498

dos Santos, A. R., de Oliveira, F. S., da Silva, A. G., Gleriani, J. M., Gonçalves, W., Moreira, G. L., Mota, P. H. S. (2017). Spatial and temporal distribution of urban heat islands. *Science of the Total Environment*, *605–606*, 946–956. https://doi.org/10.1016/j.scitotenv.2017.05.275

Drăguţ, L., Csillik, O., Eisank, C., & Tiede, D. (2014). Automated parameterisation for multi-scale image segmentation on multiple layers. *ISPRS Journal of Photogrammetry and Remote Sensing*, *88*, 119–127. https://doi.org/10.1016/j.isprsjprs.2013.11.018

European Commission. (2013). Green Infrastructure (GI) — Enhancing Europe's Natural Capital. *Communication from the Commission to the European Parliament, the European Economic Council, The European Economic and Social Committee and the Committee of the Regions*, 13. https://doi.org/10.1017/CBO9781107415324.004

European Commission. (2015). *Towards an EU Research and Innovation policy agenda for Nature-based solutions and re-naturing cities. Final Report of the Horizon 2020*.

Fan, C., Zheng, B., Huang, H., Kaplan, S., Brazel, A., Middel, A., Talen, E. (2015). Does the spatial arrangement of urban landscape matter? examples of urban warming and cooling in phoenix and las vegas. *Ecosystem Health and Sustainability*, *1*(4), 1–15. https://doi.org/10.1890/ehs14-0028.1

GeoBusiness Nederland. (2016). Aerodata Surveys Nederland. Retrieved March 22, 2020, from https://www.geobusiness.nl/leden/aerodata

Georgi, N. J., & Zafiriadis, K. (2006). The impact of park trees on microclimate in urban areas. *Urban Ecosystems*, *9*(3), 195–209. https://doi.org/10.1007/s11252-006-8590-9

Gunawardena, K. R., Wells, M. J., & Kershaw, T. (2017). Utilising green and bluespace to

mitigate urban heat island intensity. *Science of the Total Environment*, *584–585*, 1040–1055. https://doi.org/10.1016/j.scitotenv.2017.01.158

Hamada, S., & Ohta, T. (2010). Seasonal variations in the cooling effect of urban green areas on surrounding urban areas. *Urban Forestry and Urban Greening*, *9*(1), 15–24. https://doi.org/10.1016/j.ufug.2009.10.002

Hamdi, R., & Schayes, G. (2008). Sensitivity study of the urban heat island intensity to urban characteristics. *International Journal of Climatology*, *28*, 973–982. https://doi.org/10.1002/joc.1598 Sensitivity

Hexagon. (2020). ERDAS IMAGINE. Retrieved April 17, 2020, from https://www.hexagongeospatial.com/products/power-portfolio/erdas-imagine

Howard, L. (1833). *The climate of London: deduced from meteorological observations* (3rd ed.). London: Harvey & Darton.

Huang, L., Li, J., Zhao, D., & Zhu, J. (2008). A fieldwork study on the diurnal changes of urban microclimate in four types of ground cover and urban heat island of Nanjing, China. *Building and Environment*, *43*(1), 7–17. https://doi.org/10.1016/j.buildenv.2006.11.025

Jenkins, G. (2014). A comparison between two types of widely used weather stations. *Weather*, *69*(4), 105–110. https://doi.org/10.1002/wea.2158

Jones, H. G., & Vaughan, R. A. (2010). *Remote sensing of vegetation: principles, techniques and applications* (1st ed.). Oxford: Oxford University Press.

KMI. (2019). Klimaat in de wereld. Retrieved December 27, 2019, from https://www.meteo.be/nl/klimaat/klimaat-in-de-wereld

Laben, C., & Brower, B. (1998). Process for Enhancing the Spatial Resolution of Multispectral Imagery Using Pan-Sharpening. https://doi.org/10.1016/j.(73)

Lee, J. S., Kim, J. T., & Lee, M. G. (2014). Mitigation of urban heat island effect and greenroofs. *Indoor and Built Environment*, *23*(1), 62–69. https://doi.org/10.1177/1420326X12474483

Leuven 2030. (2019, June). Onderzoek hitte-eilandeffect. Retrieved December 27, 2019, from https://www.leuven2030.be/verhalen/onderzoek-hitte-eilandeffect

Li, X., Zhou, W., & Ouyang, Z. (2013). Relationship between land surface temperature and spatial pattern of greenspace: What are the effects of spatial resolution? *Landscape and Urban Planning*, *114*, 1–8. https://doi.org/10.1016/j.landurbplan.2013.02.005

Marando, F., Salvatori, E., Sebastiani, A., Fusaro, L., & Manes, F. (2019). Regulating Ecosystem Services and Green Infrastructure: assessment of Urban Heat Island effect mitigation in the municipality of Rome, Italy. *Ecological Modelling*, *392*, 92–102. https://doi.org/10.1016/j.ecolmodel.2018.11.011

McGarigal, K., Cushman, S. A., Neel, M. C., & Ene, E. (2002). FRAGSTATS: spatial pattern analysis program for categorical maps. Computer Software Program Produced by the Authors at the University of Massachusetts, Amherst. University of Massachusetts, Amherst. Retrieved from http://www.umass.edu/landeco/research/fragstats/documents/Metrics/Metrics TOC.htm

Memon, R. A., Leung, D. Y. C., & Liu, C. H. (2009). An investigation of urban heat island intensity (UHII) as an indicator of urban heating. *Atmospheric Research*, *94*(3), 491–500. https://doi.org/10.1016/j.atmosres.2009.07.006

Mohammed, Y., & Salman, A. (2018). Effect of urban geometry and green area on the formation of the urban heat island in Baghdad city. *MATEC Web of Conferences*, *162*, 05025. https://doi.org/10.1051/matecconf/201816205025

Myint, S. W., Zhang, Y., Turner, B. L., Li, X., Zhang, X., & Galletti, C. (2014). Object-based land-cover classification for metropolitan Phoenix, Arizona, using aerial photography. *International Journal of Applied Earth Observation and Geoinformation*, *33*, 321–330. https://doi.org/10.1016/j.jag.2014.04.018

Nichol, J. E., Fung, W. Y., Lam, K. se, & Wong, M. S. (2009). Urban heat island diagnosis using ASTER satellite images and "in situ" air temperature. *Atmospheric Research*, *94*(2), 276–284. https://doi.org/10.1016/j.atmosres.2009.06.011

Oke, T. R. (1976). The distinction between canopy and boundary-layer urban heat Islands. *Atmosphere*, *14*(4), 268–277. https://doi.org/10.1080/00046973.1976.9648422

Oke, T. R. (1995). The Heat Island of the Urban Boundary Layer: Characteristics, Causes and Effects. *NATO ASI Series e Applied Sciences-Advanced Study Institute*, *277*, 81–108. https://doi.org/10.1007/978-94-017-3686-2_5

Oliveira, S., Andrade, H., & Vaz, T. (2011). The cooling effect of green spaces as a contribution to the mitigation of urban heat: A case study in Lisbon. *Building and Environment*, *46*(11), 2186–2194. https://doi.org/10.1016/j.buildenv.2011.04.034

Papanastasiou, D. K., Melas, D., & Kambezidis, H. D. (2015). Air quality and thermal comfort levels under extreme hot weather. *Atmospheric Research*, *152*, 4–13. https://doi.org/10.1016/j.atmosres.2014.06.002

Polsby, D. D., & Popper, R. (1991). The Third Criterion: Compactness as a Procedural Safeguard Against Partisan Gerrymandering. *Yale Law & Policy Review*, *9*(2), 301–353. https://doi.org/10.2139/ssrn.2936284

Putseys, J. (2019a, June 1). Uw tuin: een belangrijk wapen in de strijd tegen gevaarlijke hittegolven in de stad. *Het Nieuwsblad*. Retrieved from https://www.nieuwsblad.be/cnt/dmf20190531_04438998

Putseys, J. (2019b, June 1). Uw tuin in de strijd gegooid tegen gevaarlijke hittegolven. *De Standaard*. Retrieved from https://www.standaard.be/cnt/dmf20190531_04439160?articlehash=17F480D20BF1D35FE052145124977E1EB281A45464E09F9A61BA79E4434310CA912C1C72A89F01C3C6C5BFC9C46526FB6D96329680FC6312DA5803C25AB3E5A1

QGIS Development Team. (2019). QGIS Geographic Information System. Open Source Geospatial Foundation Project. Retrieved November 30, 2019, from http://qgis.osgeo.org

Qian, Y., Zhou, W., Hu, X., & Fu, F. (2018). The heterogeneity of air temperature in urban residential neighborhoods and its relationship with the surrounding greenspace. *Remote Sensing*, *10*(6), 956. https://doi.org/10.3390/rs10060965

Renkforce. (n.d.). *Internet protocol weather station - Operation Manual*. Retrieved from https://www.conrad.nl/p/renkforce-wh2600-digitaal-draadloos-weerstation-voorspelling-voor-12-tot-24-uur-1267654

Rhee, J., Park, S., & Lu, Z. (2014). Relationship between land cover patterns and surface temperature in urban areas. *GIScience and Remote Sensing*, *51*(5), 521–536. https://doi.org/10.1080/15481603.2014.964455

ROB-TV. (2019, June 26). Onderzoekers KU Leuven plaatsen 70 weerstations om Leuven te

wapenen tegen de warmte. *ROB-TV*. Retrieved from https://www.robtv.be/nieuws/onderzoekers-ku-leuven-plaatsen-70-weerstations-om-leuven-te-wapenen-tegen-de-warmte-80686

Roth, M., Oke, T. R., & Emery, W. J. (1989). Satellite-derived urban heat islands from three coastal cities and the utilization of such data in urban climatology. *International Journal of Remote Sensing*. https://doi.org/10.1080/01431168908904002

RStudio Team. (2016). RStudio: Integrated Development Environment for R. Boston, MA: RStudio, Inc. Retrieved from http://www.rstudio.com/

Rushayati, S. B., Shamila, A. D., & Prasetyo, L. B. (2018). The Role of Vegetation in Controlling Air Temperature Resulting from Urban Heat Island. *Forum Geografi*, *32*(1), 1–11. https://doi.org/10.23917/forgeo.v32i1.5289

Sajani, S. Z., Marchesi, S., Lauriola, P., Tomozeiu, R., Botarelli, L., Bonafè, G., … Bonazzi, F. (2016). UHI in the metropolitan cluster of bologna-modena: Mitigation and adaptation strategies. In *Counteracting Urban Heat Island Effects in a Global Climate Change Scenario* (pp. 131–200). Springer International Publishing.

Santamouris, M., Cartalis, C., Synnefa, A., & Kolokotsa, D. (2015). On the impact of urban heat island and global warming on the power demand and electricity consumption of buildings - A review. *Energy and Buildings*, *98*, 119–124. https://doi.org/10.1016/j.enbuild.2014.09.052

Satchithanantham, S., Wilson, H. F., & Glenn, A. J. (2017). Contrasting patterns of groundwater evapotranspiration in grass and tree dominated riparian zones of a temperate agricultural catchment. *Journal of Hydrology*, *549*, 654–666. https://doi.org/10.1016/j.jhydrol.2017.04.016

Shashua-Bar, L., & Hoffman, M. E. (2000). Vegetation as a climatic component in the design of an urban street. *Energy and Buildings*, *31*(3), 221–235. https://doi.org/10.1016/s0378-7788(99)00018-3

Sheng, L., Tang, X., You, H., Gu, Q., & Hu, H. (2017). Comparison of the urban heat island intensity quantified by using air temperature and Landsat land surface temperature in Hangzhou, China. *Ecological Indicators*, *72*, 738–746. https://doi.org/10.1016/j.ecolind.2016.09.009

Solecki, W. D., Rosenzweig, C., Parshall, L., Pope, G., Clark, M., Cox, J., & Wiencke, M. (2005). Mitigation of the heat island effect in urban New Jersey. *Environmental Hazards*, *6*(1), 39–49. https://doi.org/10.1016/j.hazards.2004.12.002

Stad Leuven. (2018). Deelgemeenten. Retrieved December 27, 2019, from https://www.leuven.be/deelgemeenten

Stan, F. I., Neculau, G., Zaharia, L., & Ioana-Toroimac, G. (2014). Evapotranspiration variability of different plant types at romanian experimental evapometric measurement stations. *Climatologie*, *11*(Volume 11), 1962–1966. https://doi.org/10.4267/climatologie.603

Stewart, I. D., & Oke, T. R. (2012). Local climate zones for urban temperature studies. *Bulletin of the American Meteorological Society*, *93*(12), 1879–1900. https://doi.org/10.1175/BAMS-D-11-00019.1

Streiling, S., & Matzarakis, A. (2003). Influence of single and small clusters of trees on the bioclimate of a city: A case study. *Journal of Arboriculture*, *29*(6), 309–316.

The World Bank Group. (2017). World Development Indicators : Urbanization. Retrieved March 29, 2019, from https://data.worldbank.org/indicator/SP.URB.TOTL.IN.ZS?locations=BE&year_high_desc=false

The World Bank Group. (2018). Population density - Belgium. Retrieved April 28, 2020, from https://data.worldbank.org/indicator/EN.POP.DNST?end=2018&locations=BE&start=2015

Thom, E. C. (1959). The Discomfort Index. *Weatherwise*, *12*(2), 57–61. https://doi.org/10.1080/00431672.1959.9926960

U.S. Environmental Protection Agency. (2008). Urban Heat Island Basics. *Reducing Urban Heat Islands: Compendium of Strategies*. Retrieved from https://www.epa.gov/heat-islands/ heat-island-compendium.

United Nations. Departemen of Economic and Social Affairs. Population Division. (2018). *World Urbanization Prospects: The 2018 Revision*. New York. Retrieved from https://population.un.org/wup/Publications/Files/WUP2018-KeyFacts.pdf

United Nations. Departemen of Economic and Social Affairs. Population Division. (2019). *World Urbanization Prospects 2018: Highlights*. New York. Retrieved from https://population.un.org/wup/

Uuemaa, E., Antrop, M., Roosaare, J., Marja, R., & Mander, Ü. (2009). Landscape Metrics and Indices: An Overview of Their Use in Landscape Research. *Living Reviews in Landscape Research*, *3*, 61–63. https://doi.org/10.12942/lrlr-2009-1

Van Eetvelde, V. (2007). *Van geografische strekenkaart tot landschapsdatabank: Gebruik van GIS , informatietheorie en karakteriseren van landschappen ,*. Universiteit Gent.

van Hove, L. W. A., Jacobs, C. M. J., Heusinkveld, B. G., Elbers, J. A., Van Driel, B. L., & Holtslag, A. A. M. (2015). Temporal and spatial variability of urban heat island and thermal comfort within the Rotterdam agglomeration. *Building and Environment*, *83*, 91–103. https://doi.org/10.1016/j.buildenv.2014.08.029

Verdonck, M. L., Demuzere, M., Hooyberghs, H., Beck, C., Cyrys, J., Schneider, A., … Van Coillie, F. (2018). The potential of local climate zones maps as a heat stress assessment tool, supported by simulated air temperature data. *Landscape and Urban Planning*, *178*, 183–197. https://doi.org/10.1016/j.landurbplan.2018.06.004

Vidal-Abarca, A., Jimezez, M., Rodrigo, T., & Cabezas, M. (2016). Europe Urbanization Trends. Retrieved from https://www.bbvaresearch.com/wp-content/uploads/2016/12/European-urbanization-trends_.pdf

Voogt, J. A., & Oke, T. R. (2003). Thermal remote sensing of urban climates. *Remote Sensing of Environment*, *86*(3), 370–384. https://doi.org/10.1016/S0034-4257(03)00079-8

Weng, Q., Lu, D., & Schubring, J. (2004). Estimation of land surface temperature-vegetation abundance relationship for urban heat island studies. *Remote Sensing of Environment*, *89*(4), 467–483. https://doi.org/10.1016/j.rse.2003.11.005

White, M. A., Nemani, R. R., Thornton, P. E., & Running, S. W. (2002). Satellite evidence of phenological differences between urbanized and rural areas of the eastern United States deciduous broadleaf forest. *Ecosystems*, *5*(3), 260–273. https://doi.org/10.1007/s10021-001-0070-8

Xiao, X. D., Dong, L., Yan, H., Yang, N., & Xiong, Y. (2018). The influence of the spatial characteristics of urban green space on the urban heat island effect in Suzhou Industrial Park. *Sustainable Cities and Society*, *40*, 428–439. https://doi.org/10.1016/j.scs.2018.04.002

Yan, H., & Dong, L. (2015). The impacts of land cover types on urban outdoor thermal environment: the case of Beijing, China. *Journal of Environmental Health Science and Engineering*, *13*(1), 1–7. https://doi.org/10.1186/s40201-015-0195-x

Yan, H., Fan, S., Guo, C., Hu, J., & Dong, L. (2014). Quantifying the impact of land cover composition on intra-urban air temperature variations at a mid-latitude city. *PLoS ONE*, *9*(7). https://doi.org/10.1371/journal.pone.0102124

Yan, J., Zhou, W., Han, L., & Qian, Y. (2018). Mapping vegetation functional types in urban areas with WorldView-2 imagery: Integrating object-based classification with phenology. *Urban Forestry and Urban Greening*, *31*, 230–240. https://doi.org/10.1016/j.ufug.2018.01.021

Yuhendra, Alimuddin, I., Sumantyo, J. T. S., & Kuze, H. (2012). Assessment of pan-sharpening methods applied to image fusion of remotely sensed multi-band data. *International Journal of Applied Earth Observation and Geoinformation*, *18*(1), 165–175. https://doi.org/10.1016/j.jag.2012.01.013

Zhou, W., Huang, G., & Cadenasso, M. L. (2011). Does spatial configuration matter? Understanding the effects of land cover pattern on land surface temperature in urban landscapes. *Landscape and Urban Planning*, *102*(1), 54–63. https://doi.org/10.1016/j.landurbplan.2011.03.009

Zhou, W., Huang, G., Troy, A., & Cadenasso, M. L. (2009). Object-based land cover classification of shaded areas in high spatial resolution imagery of urban areas: A comparison study. *Remote Sensing of Environment*, *113*(8), 1769–1777. https://doi.org/10.1016/j.rse.2009.04.007

Zhou, W., Wang, J., & Cadenasso, M. L. (2017). Effects of the spatial configuration of trees on urban heat mitigation : A comparative study. *Remote Sensing of Environment*, *195*, 1–12. https://doi.org/10.1016/j.rse.2017.03.043

8 Appendix

8.1 Specifications of the WH2600 digital weather station

Table 8.1: Specifications of the Renkforce digital weather station WH2600

OUTDOOR DATA	
Transmission distance in open field	100m(330 feet)
Frequency	433 MHz / 868 MHz / 915 MHz (option)
Temperature range	-40 °C - 60 °C
Accuracy	+/- 1 °C
Resolution	0.1 °C
Relative humidity range	1% - 99%
Accuracy	+/- 5%
Rain volume display	0 – 9999mm
Accuracy	+/- 10%
Resolution	0.3mm (if rain volume < 1000mm) 1mm (if rain volume > 1000mm)
Windspeed	0-50m/s (0-100mph)
Accuracy	+/- 1m/s (wind speed< 5m/s) +/-10% (wind speed > 5m/s)
Light	0-400k Lux
Accuracy	+/-15%
Measuring interval outdoor sensor WH24	16 sec
INDOOR DATA	
Indoor temperature range	-40 °C - 60 °C
Resolution	0.1 °C
Relative humidity range	1% - 99%
Resolution	1%
Air pressure range	300-1100hPa
Accuracy	+/-3hpa under 700-1100hPa
Resolution	0.1hPa
Alarm duration	120 sec

8.2 Classification code garden inventories

Table 8.2: Classification code for digitizing the garden inventories.

	Green Roof		**Walls & facades**
1.1	extensive Green Roof/grass	7.1	vertical green (gevelgroen)
1.2	intensive Green Roof/woods	7.2	plants on fence (begroeide omheining)
1.3	others and specify	7.3	other and specify
	Sealed/impervious surfaces		**Grass**
2.1	pavement - terrace	8.1	lawn (mowed regularly)
2.2	sand surface	8.2	meadow (not mowed regularly)
2.3	rock surface	8.3	others and specify
2.4	others and specify	8.4	high grass
2.5	wooden terrace		
2.6	gravel		
2.7	fake lawn (fake grass)		
	Water		**Low green (shrubs. flowers <1m)**
3.1	swimming pool (artificial)	9.1	production garden (moestuin)
3.2	pond (natural)	9.2	bedding plants (perkplanten/plantenborder)
3.3	others and specify	9.3	flower meadow
		9.4	brushwood/tall herb vegetation (ruigte)
		9.5	others and specify
	Soil/pervious surface		**Mid green (shrubs and trees at 1-5m)**
4.1	bare soil	10.1	mixture of shrubs and trees (< 1m)
4.2	wood chips	10.2	decidious tree (solitairy)
4.3	others and specify	10.3	conifer tree (solitairy)
		10.4	fruit tree (solitairy)
		10.5	group/row of woods
		10.6	others and specify
	Manmade constructions		**High green (shrubs and trees >5m)**
5.1	buildings	11.1	decidious tree (solitairy)
5.2	trampoline	11.2	conifer tree (solitairy)
5.3	playground	11.3	fruit tree (solitairy)
5.4	others and specify	11.4	group/row of woods
		11.5	others and specify
	Fences		
6.1	wall fence		
6.2	wood fence		
6.3	iron fence		
6.4	others and specify		

8.3 GarmonR01 vs GarmonR02

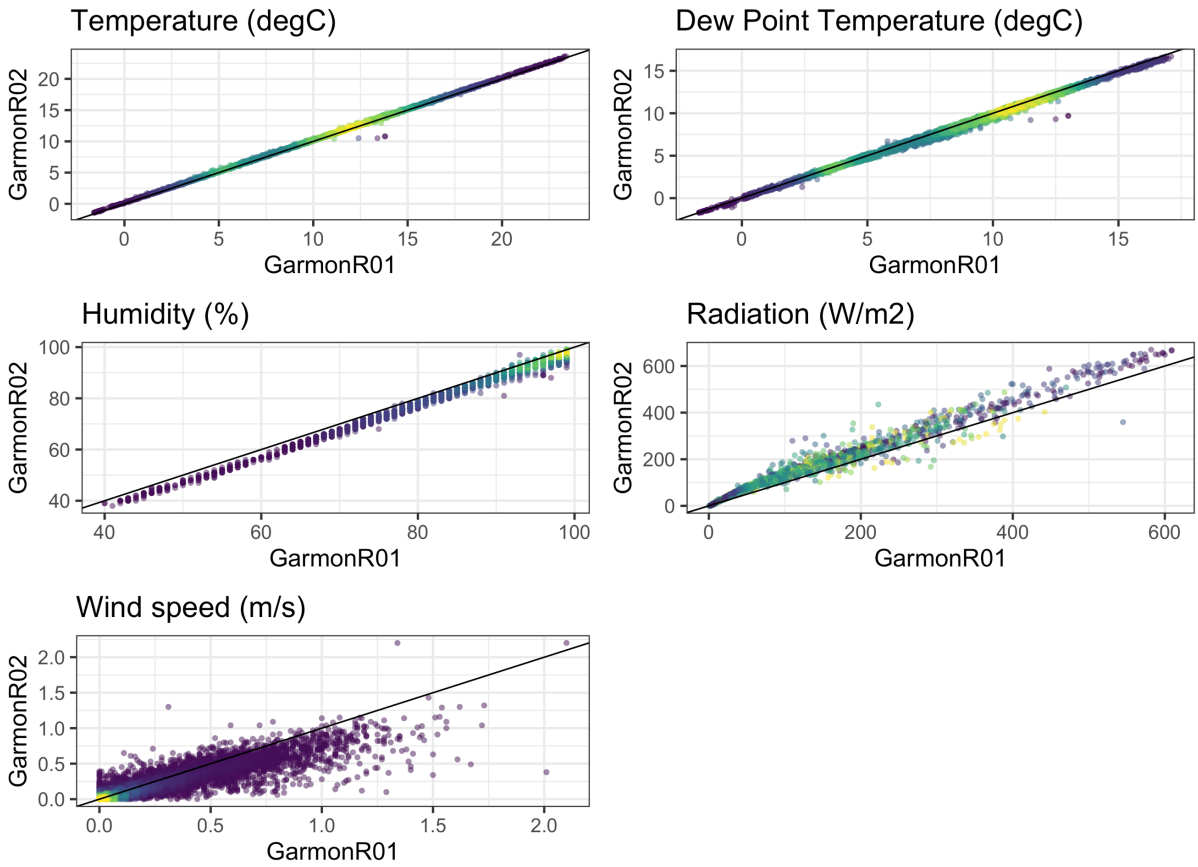

Figure 8.1: Scatterplots comparing temperature, dew point temperature, humidity, radiation and windspeed measured by both GarmonR01 and GarmonR02. The color scale indicates the density of the observations, yellow indicating the highest.

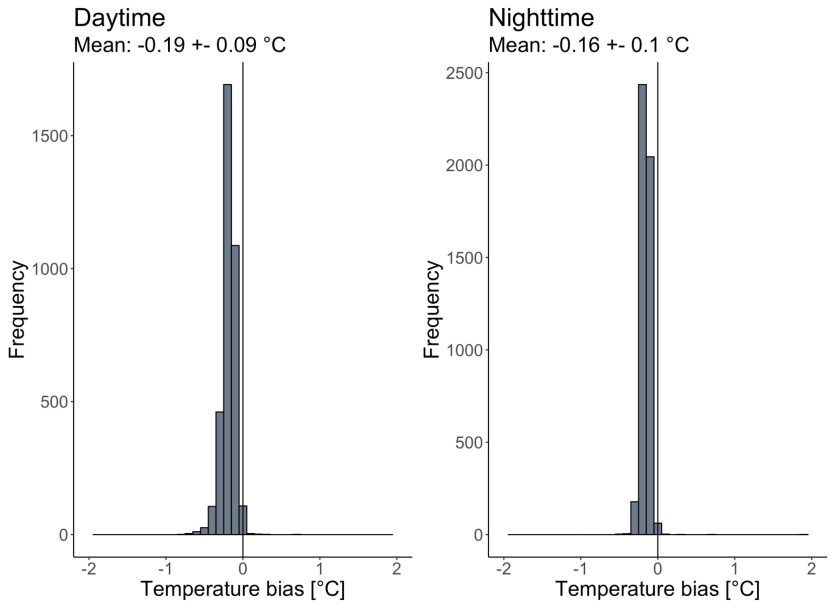

Figure 8.2: Histograms of temperature bias between GarmonR01 and GarmonR02 split up for day (radiation > 0) and night time (radiation ≤ 0). Mean biases and their standard deviations are given above the graphs.

8.4 Garmon network

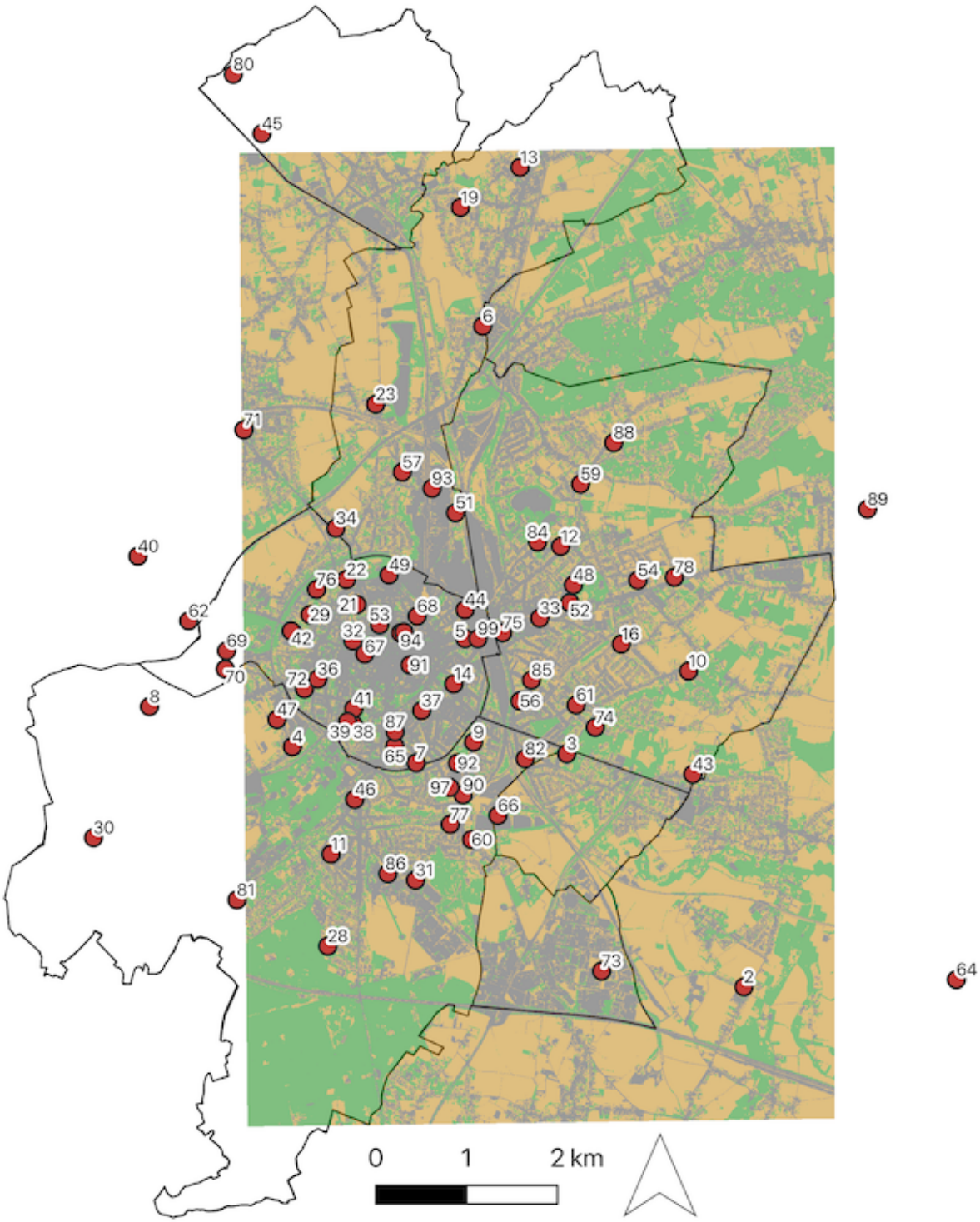

Figure 8.3: Overview of complete Garmon network (2019), each red dot represents a weather station, their labels refer to their specific Garmon ID. The background image presents the green map of Leuven (green=high green, yellow=low green, grey=others).

Table 8.3: Overview table of stations in the Garmon network (2019), after each Garmon ID the LCZ class is mentioned as well whether the station is installed in a private garden or on a (semi-) public terrain.

Station ID	LCZ class ID	Station type	Station ID	LCZ class ID	Station type
Garmon002	223	Private	Garmon053	113	Private
Garmon003	122	Private	Garmon054	212	Private
Garmon004	212	Private	Garmon056	112	Private
Garmon005	113	Private	Garmon057	221	Private
Garmon006	213	Private	Garmon059	221	Private
Garmon007	122	Private	Garmon060	222	Private
Garmon008	222	Private	Garmon061	213	Private
Garmon009	123	Private	Garmon062	221	Private
Garmon010	223	Private	Garmon064	122	Private
Garmon011	112	Private	Garmon065	113	Private
Garmon012	122	Private	Garmon066	221	(Semi-)public
Garmon013	223	Private	Garmon067	113	(Semi-)public
Garmon014	112	Private	Garmon068	113	(Semi-)public
Garmon016	222	Private	Garmon069	123	(Semi-)public
Garmon019	222	Private	Garmon070	122	(Semi-)public
Garmon021	122	Private	Garmon071	213	Private
Garmon022	222	Private	Garmon072	212	Private
Garmon023	213	Private	Garmon073	123	(Semi-)public
Garmon028	222	Private	Garmon074	221	Private
Garmon029	213	Private	Garmon075	212	Private
Garmon030	222	Private	Garmon076	122	(Semi-)public
Garmon031	223	Private	Garmon077	212	Private
Garmon032	113	Private	Garmon078	223	Private
Garmon033	213	Private	Garmon080	221	Private
Garmon034	213	Private	Garmon081	221	Private
Garmon036	222	(Semi-)public	Garmon082	213	Private
Garmon037	113	(Semi-)public	Garmon084	212	Private
Garmon038	113	(Semi-)public	Garmon085	112	Private
Garmon039	112	(Semi-)public	Garmon086	122	(Semi-)public
Garmon040	222	Private	Garmon087	113	(Semi-)public
Garmon041	122	Private	Garmon088	223	Private
Garmon042	112	Private	Garmon089	222	Private
Garmon043	221	Private	Garmon090	122	Private
Garmon044	112	Private	Garmon091	113	(Semi-)public
Garmon045	223	Private	Garmon092	123	(Semi-)public
Garmon046	122	Private	Garmon093	123	(Semi-)public
Garmon047	212	Private	Garmon094	113	(Semi-)public
Garmon048	122	(Semi-)public	Garmon096	122	(Semi-)public
Garmon049	113	(Semi-)public	Garmon097	221	Private
Garmon051	223	Private	Garmon098	113	(Semi-)public
Garmon052	112	Private	Garmon099	113	(Semi-)public

8.5 Temperature bias as function of windspeed and radiation

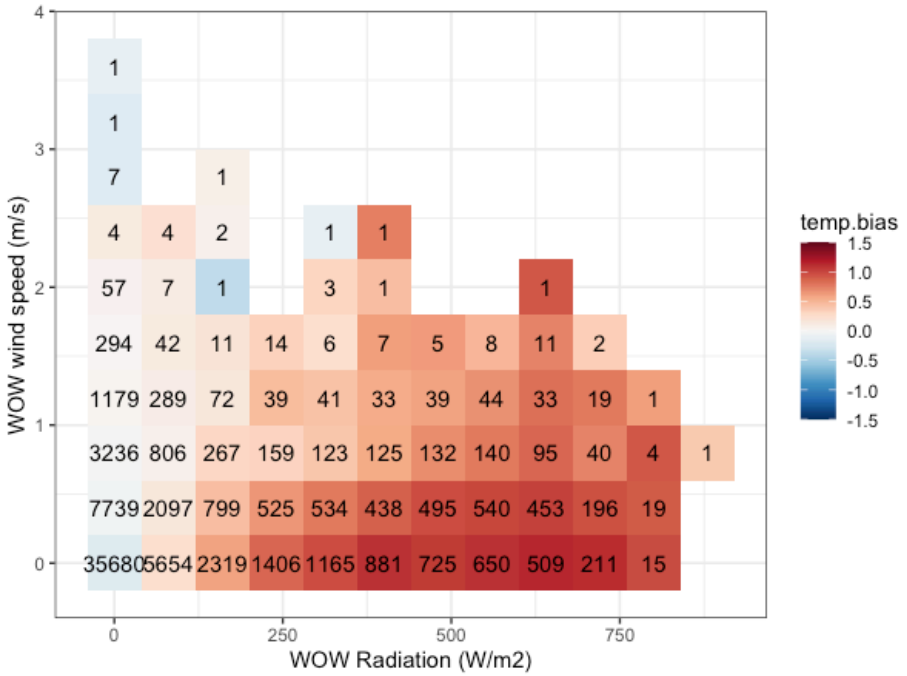

Figure 8.4: The mean temperature bias as function of windspeed and radiation measured by the GarmonR01 station. The values written in each cell signify the sample size.

8.6 Summary tables of landscape metrics

Table 8.4: The minimum, maximum, mean and standard deviation values of PLAND for all Garmon station active during August 28th night (53 stations) and those active during August 23th-28th nights (40 stations).

		High green				Low green			
		Min	Max	Mean	Std dev	Min	Max	Mean	Std dev
10m	Aug 28th	0.00	55.99	10.57	13.52	0.00	100.00	61.62	22.68
	Aug 23-28th	0.00	55.99	11.22	14.56	0.00	95.77	57.68	23.63
20m	Aug 28th	0.00	54.85	16.47	14.08	1.78	82.00	44.56	19.18
	Aug 23-28th	0.00	54.85	16.62	14.37	1.78	82.00	42.31	19.47
30m	Aug 28th	0.00	53.88	17.68	13.9	2.29	74.78	37.58	16.53
	Aug 23-28th	0.00	53.88	17.5	14.3	2.29	74.78	35.75	16.67
50m	Aug 28th	0.00	50.21	17.43	12.48	0.94	51.63	28.36	12.33
	Aug 23-28th	0.00	46.91	16.87	11.76	0.94	51.63	27.01	12.21
80m	Aug 28th	0.31	55.86	17.9	11.16	1.97	50.79	24.90	10.57
	Aug 23-28th	0.31	41.01	16.45	10.09	1.97	50.79	24.29	10.97
100m	Aug 28th	0.57	54.83	18.52	10.71	1.59	54.6	24.2	10.71

	Aug 23-28th	0.57	51.32	16.91	9.71	1.59	54.6	23.80	11.20
130m	Aug 28th	1.13	56.10	18.47	10.59	1.68	57.80	23.55	10.88
	Aug 23-28th	1.13	55.37	16.82	9.47	1.68	57.80	23.59	11.44
180m	Aug 28th	2.02	55.98	18.28	10.46	2.47	59.42	22.83	10.59
	Aug 23-28th	2.02	55.98	16.98	9.49	2.47	59.42	23.12	11.04
250m	Aug 28th	3.82	57.55	18.00	10.22	6.26	68.41	22.75	11.21
	Aug 23-28th	3.82	57.55	17.00	9.54	6.94	68.41	23.22	11.50
500m	Aug 28th	5.12	58.22	19.40	9.08	7.56	67.42	22.83	11.55
	Aug 23-28th	6.83	58.22	18.95	8.84	7.56	67.42	23.34	12.06

Table 8.5 The minimum, maximum, mean and standard deviation values of LPI for all Garmon station active during August 28th night (53 stations) and those active during August 23th-28th nights (40 stations).

		High green				Low green			
		Min	Max	Mean	Std dev	Min	Max	Mean	Std dev
10m	Aug 28th	0.00	55.99	9.59	13.10	0.00	100.00	59.76	24.17
	Aug 23-28th	0.00	55.99	10.24	14.17	0.00	95.77	55.36	25.19
20m	Aug 28th	0.00	51.62	12.94	12.69	0.97	82.00	39.62	20.95
	Aug 23-28th	0.00	51.62	13.33	13.35	0.97	82.00	37.17	21.05
30m	Aug 28th	0.00	53.56	13.97	12.86	1.00	74.71	30.64	18.69
	Aug 23-28th	0.00	53.56	14.11	13.46	1.00	74.71	28.81	18.81
50m	Aug 28th	0.00	47.65	12.26	11.62	0.36	48.67	20.76	13.24
	Aug 23-28th	0.00	42.98	12.03	11.05	0.36	48.67	18.95	12.93
80m	Aug 28th	0.11	55.65	10.64	10.03	0.92	36.97	13.78	9.50
	Aug 23-28th	0.11	34.62	9.48	8.02	0.95	36.97	12.84	9.50
100m	Aug 28th	0.11	53.86	10.12	9.28	0.62	33.63	11.47	8.26
	Aug 23-28th	0.11	34.22	8.63	7.00	0.64	33.63	10.85	8.30
130m	Aug 28th	0.33	53.8	9.26	10.46	0.57	30.22	9.08	7.13
	Aug 23-28th	0.33	50.16	7.90	9.09	0.57	30.22	8.89	7.32
180m	Aug 28th	0.19	52.16	8.26	9.93	0.51	26.76	6.40	5.56
	Aug 23-28th	0.19	52.16	7.48	8.98	0.51	26.76	6.51	5.76
250m	Aug 28th	0.30	52.94	7.29	9.55	0.38	27.54	5.24	5.10
	Aug 23-28th	0.30	52.94	6.89	9.01	0.38	27.54	5.32	5.14
500m	Aug 28th	0.41	50.86	6.69	8.03	0.25	20.46	4.14	5.09
	Aug 23-28th	0.7	50.86	6.79	8.43	0.25	20.46	4.35	5.48

Table 8.6 The minimum, maximum, mean and standard deviation values of ED for all Garmon station active during August 28th night (53 stations) and those active during August 23th-28th nights (40 stations).

		High green				Low green			
		Min	Max	Mean	Std dev	Min	Max	Mean	Std dev
10m	Aug 28th	0.00	2419.35	565.79	565.81	0.00	3215.43	1629.84	686.99
	Aug 23-28th	0.00	2419.35	577.56	590.65	0.00	3215.43	1615.96	702.08
20m	Aug 28th	0.00	1653.16	625.90	399.27	202.27	2394.48	1431.35	412.13
	Aug 23-28th	0.00	1356.21	608.70	395.00	202.27	2394.48	1396.91	422.09
30m	Aug 28th	0.00	1367.22	608.59	337.68	253.57	2044.40	1269.54	317.28
	Aug 23-28th	0.00	1367.22	587.56	338.15	253.57	2044.40	1264.00	323.38
50m	Aug 28th	0.00	1167.03	528.51	238.07	107.42	1657.82	1091.73	328.37
	Aug 23-28th	0.00	1167.03	516.24	250.75	107.42	1657.82	1081.42	346.12
80m	Aug 28th	39.48	1059.08	503.72	184.74	199.42	1488.60	985.73	302.02
	Aug 23-28th	39.48	1059.08	482.73	196.75	199.42	1488.60	967.72	313.08
100m	Aug 28th	62.40	1017.49	489.42	163.51	168.54	1462.82	953.09	296.88
	Aug 23-28th	62.40	1017.49	472.89	176.47	168.54	1462.82	941.50	310.90
130m	Aug 28th	87.63	929.02	470.60	145.53	143.38	1411.59	919.35	287.54
	Aug 23-28th	87.63	929.02	458.43	153.37	143.38	1411.59	913.84	303.68
180m	Aug 28th	147.23	854.27	453.37	135.49	187.90	1388.90	879.32	268.36
	Aug 23-28th	147.23	854.27	448.60	140.55	187.90	1388.90	881.15	281.53
250m	Aug 28th	210.77	709.20	438.42	123.80	298.29	1377.64	841.31	251.37
	Aug 23-28th	217.41	709.20	430.95	121.31	298.29	1377.64	851.06	250.46
500m	Aug 28th	206.78	620.80	417.86	95.73	384.23	1200.15	777.97	204.64
	Aug 23-28th	244.92	620.80	409.03	82.98	384.23	1200.15	783.78	201.09

Table 8.7: The minimum, maximum, mean and standard deviation values of ED for all Garmon station active during August 28th night (53 stations) and those active during August 23th-28th nights (40 stations).

		High green				Low green			
		Min	Max	Mean	Std dev	Min	Max	Mean	Std dev
10m	Aug 28th	0.00	12861.74	3537.75	3369.83	0.00	12861.74	4820.32	2579.88
	Aug 23-28th	0.00	9771.99	3561.82	3181.49	0.00	12861.74	5019.53	2733.57
20m	Aug 28th	0.00	4874.09	1968.46	1263.69	804.51	6467.26	2213.66	1350.32
	Aug 23-28th	0.00	4874.09	1961.97	1306.75	804.51	6467.26	2407.90	1416.54
30m	Aug 28th	0.00	2862.25	1409.53	722.56	357.65	4652.83	1672.67	937.48
	Aug 23-28th	0.00	2862.25	1465.63	753.39	357.65	4652.83	1787.47	936.95
50m	Aug 28th	0.00	2204.93	989.12	412.80	388.10	2717.04	1335.83	552.39

	Aug 23-28th	0.00	1811.59	928.68	380.95	388.10	2717.04	1384.94	569.28
80m	Aug 28th	149.94	1649.51	867.69	354.13	549.75	2000.20	1182.72	400.04
	Aug 23-28th	149.94	1649.51	857.27	348.77	549.78	2000.20	1187.21	394.26
100m	Aug 28th	129.40	1423.76	776.56	285.92	582.86	1878.18	1108.69	315.56
	Aug 23-28th	129.40	1423.76	775.74	274.93	582.86	1878.18	1140.59	328.57
130m	Aug 28th	134.00	1148.57	720.38	218.72	478.59	2049.14	1022.05	306.96
	Aug 23-28th	134.00	1148.57	729.54	217.02	478.59	2049.14	1036.87	320.03
180m	Aug 28th	256.03	1043.64	651.08	189.29	452.98	1634.86	953.39	248.85
	Aug 23-28th	256.05	1043.64	659.81	193.92	521.96	1634.86	970.02	257.30
250m	Aug 28th	222.63	1004.67	618.12	179.53	403.84	1393.13	895.47	241.33
	Aug 23-28th	269.22	1004.67	623.29	181.31	460.93	1393.13	914.16	252.82
500m	Aug 28th	169.56	818.15	531.58	142.00	302.93	1166.21	816.92	194.31
	Aug 23-28th	226.55	818.15	530.24	140.06	302.93	1166.21	823.43	198.56

Table 8.8: The minimum, maximum, mean and standard deviation values of AREA_MN for all Garmon station active during August 28th night (53 stations) and those active during August 23th-28th nights (40 stations).

		High green				Low green			
		Min	Max	Mean	Std dev	Min	Max	Mean	Std dev
10m	Aug 28th	0.00	0.02	0.00	0.00	0.00	0.03	0.02	0.01
	Aug 23-28th	0.00	0.02	0.00	0.00	0.00	0.03	0.01	0.01
20m	Aug 28th	0.00	0.05	0.01	0.01	0.00	0.10	0.03	0.03
	Aug 23-28th	0.00	0.05	0.01	0.01	0.00	0.10	0.03	0.03
30m	Aug 28th	0.00	0.08	0.02	0.02	0.00	0.18	0.04	0.04
	Aug 23-28th	0.00	0.06	0.01	0.01	0.00	0.16	0.03	0.04
50m	Aug 28th	0.00	0.08	0.02	0.02	0.00	0.12	0.03	0.03
	Aug 23-28th	0.00	0.07	0.02	0.02	0.00	0.12	0.03	0.03
80m	Aug 28th	0.00	0.19	0.03	0.03	0.00	0.06	0.02	0.02
	Aug 23-28th	0.00	0.08	0.02	0.02	0.00	0.06	0.02	0.01
100m	Aug 28th	0.00	0.15	0.03	0.03	0.00	0.06	0.02	0.01
	Aug 23-28th	0.00	0.10	0.03	0.02	0.00	0.06	0.02	0.01
130m	Aug 28th	0.00	0.13	0.03	0.03	0.00	0.07	0.02	0.01
	Aug 23-28th	0.00	0.13	0.03	0.02	0.00	0.07	0.02	0.01
180m	Aug 28th	0.00	0.15	0.03	0.03	0.00	0.09	0.03	0.01
	Aug 23-28th	0.00	0.15	0.03	0.02	0.00	0.09	0.02	0.01
250m	Aug 28th	0.01	0.13	0.03	0.03	0.01	0.15	0.03	0.02
	Aug 23-28th	0.01	0.13	0.03	0.02	0.01	0.15	0.03	0.02

500m	Aug 28th	0.01	0.18	0.04	0.03	0.01	0.22	0.03	0.03
	Aug 23-28th	0.01	0.18	0.04	0.03	0.01	0.22	0.03	0.03

Table 8.9: The minimum, maximum, mean and standard deviation values of SHAPE_MN for all Garmon station active during August 28th night (53 stations) and those active during August 23th-28th nights (40 stations).

		High green				Low green			
		Min	Max	Mean	Std dev	Min	Max	Mean	Std dev
10m	Aug 28th	0,00	2.00	0.90	0.66	0.00	2.44	1.46	0.36
	Aug 23-28th	0.00	2.00	0.93	0.66	0.00	2.19	1.41	0.34
20m	Aug 28th	0.00	2.53	1.28	0.50	1.05	3.61	1.77	0.51
	Aug 23-28th	0.00	2.04	1.21	0.51	1.05	3.61	1.72	0.54
30m	Aug 28th	0.00	2.33	1.35	0.35	1.00	4.10	1.76	0.53
	Aug 23-28th	0.00	1.95	1.29	0.34	1.00	4.10	1.73	0.57
50m	Aug 28th	0.00	1.88	1.38	0.25	1.03	2.67	1.66	0.30
	Aug 23-28th	0.00	1.88	1.38	0.28	1.03	2.67	1.65	0.32
80m	Aug 28th	1.10	1.65	1.40	0.12	1.33	2.01	1.61	0.16
	Aug 23-28th	1.10	1.65	1.39	0.12	1.36	2.01	1.59	0.15
100m	Aug 28th	1.14	1.84	1.40	0.12	1.27	1.85	1.59	0.13
	Aug 23-28th	1.14	1.65	1.39	0.10	1.27	1.85	1.57	0.12
130m	Aug 28th	1.24	1.59	1.39	0.07	1.31	1.94	1.60	0.13
	Aug 23-28th	1.24	1.55	1.39	0.07	1.31	1.80	1.59	0.12
180m	Aug 28th	1.23	1.58	1.40	0.07	1.39	1.88	1.61	0.10
	Aug 23-28th	1.23	1.58	1.40	0.08	1.39	1.88	1.60	0.10
250m	Aug 28th	1.25	1.55	1.40	0.07	1.45	1.82	1.61	0.08
	Aug 23-28th	1.26	1.55	1.40	0.07	1.45	1.82	1.60	0.08
500m	Aug 28th	1.30	1.52	1.41	0.05	1.47	1.81	1.60	0.07
	Aug 23-28th	1.30	1.51	1.41	0.05	1.47	1.75	1.60	0.06

8.7 Scatterplots of temperature variable vs landscape metric

8.7.1 Minimum temperature

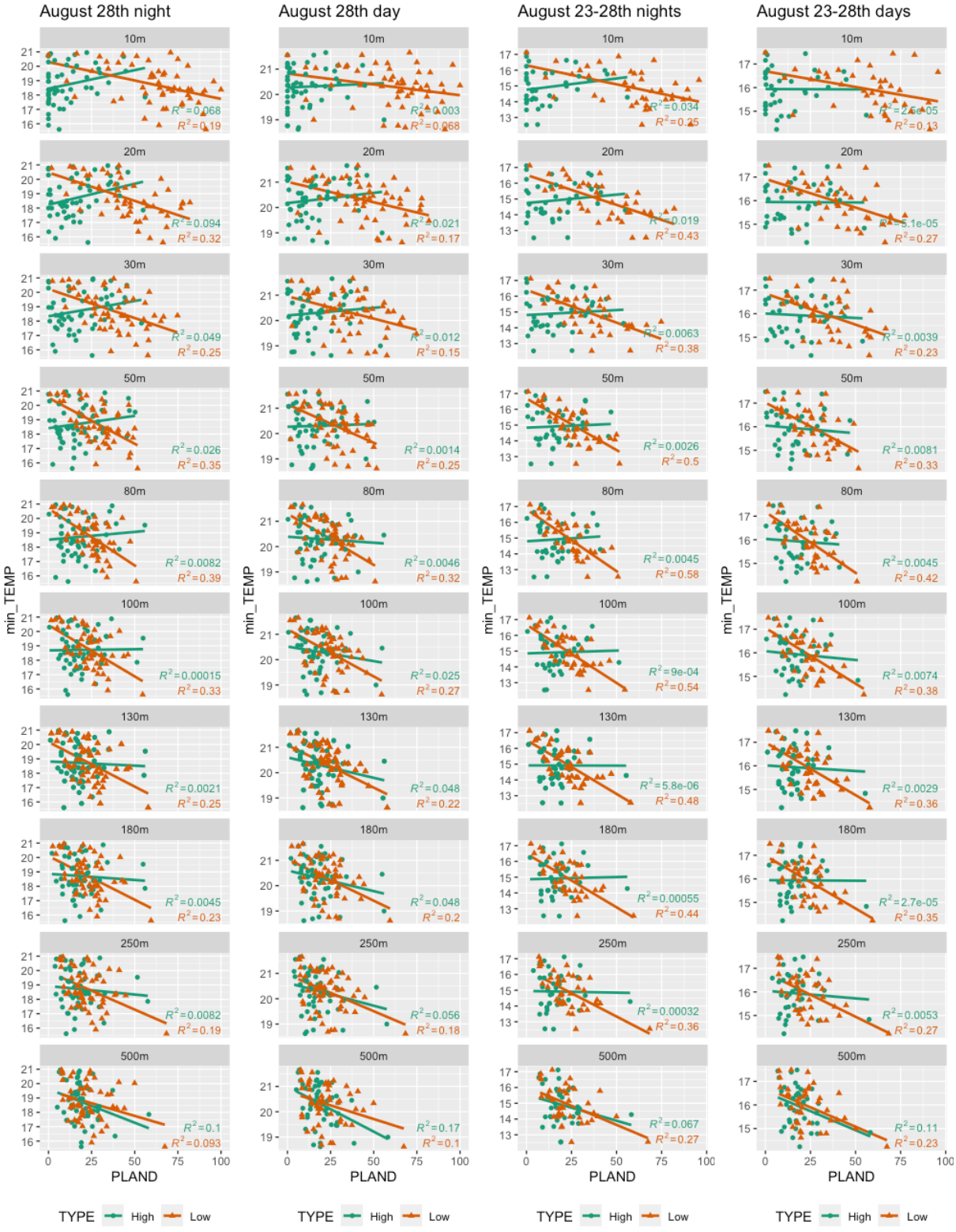

Figure 8.5: Scatterplots between minimum temperature and the percentage cover of high and low green for multiple spatial (10m, 20m, 30m, 50m, 80m, 100, 130m, 180m, 250m and 500m) and temporal scales (August 28th night/day and August 23-28th nights/days).

Figure 8.6: Scatterplots between minimum temperature and the largest patch index of high and low green for multiple spatial (10m, 20m, 30m, 50m, 80m, 100, 130m, 180m, 250m and 500m) and temporal scales (August 28th night/day and August 23-28th nights/days).

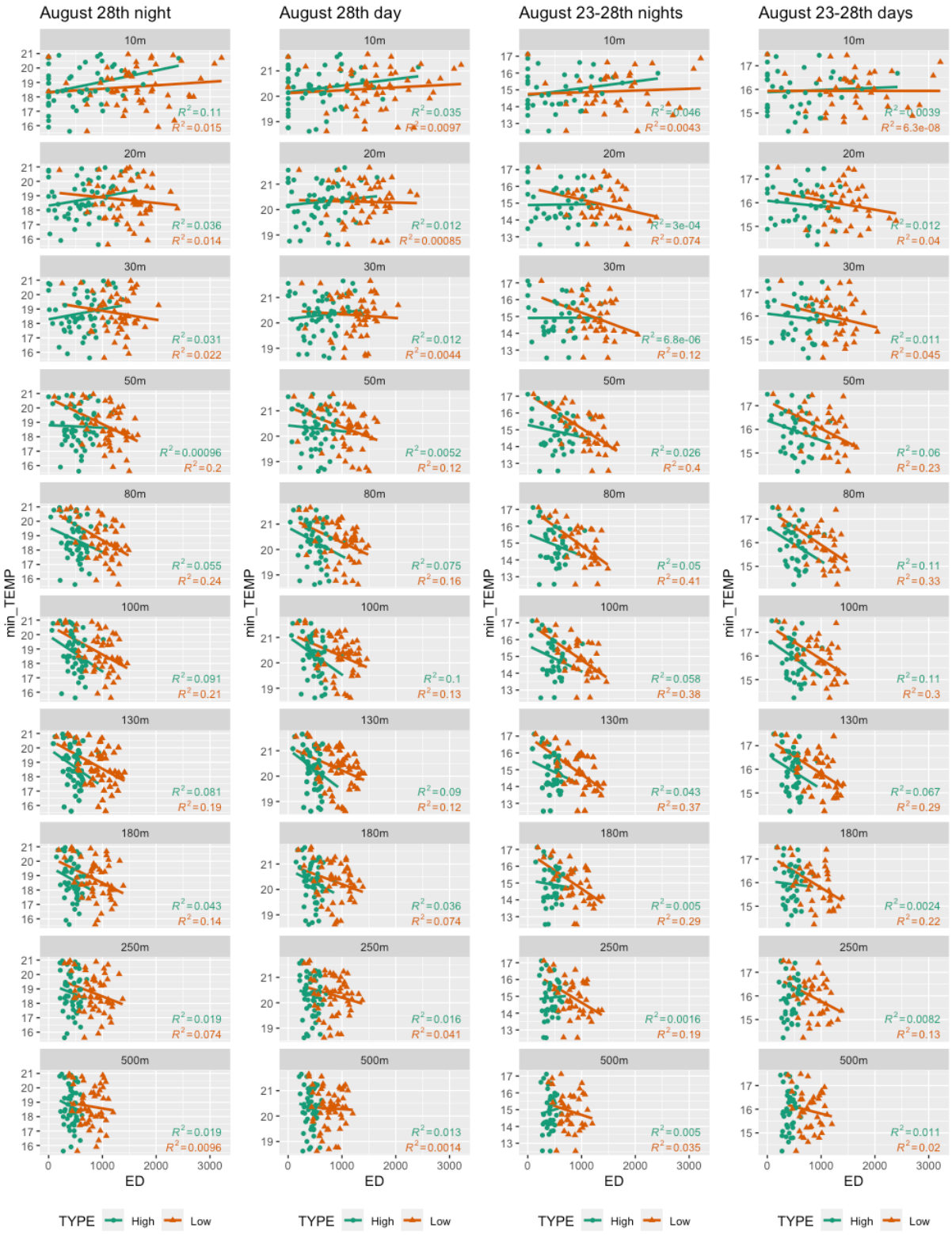

Figure 8.7: Scatterplots between minimum temperature and the edge density of high and low green for multiple spatial (10m, 20m, 30m, 50m, 80m, 100, 130m, 180m, 250m and 500m) and temporal scales (August 28th night/day and August 23-28th nights/days).

Figure 8.8: Scatterplots between minimum temperature and the patch density of high and low green for multiple spatial (10m, 20m, 30m, 50m, 80m, 100, 130m, 180m, 250m and 500m) and temporal scales (August 28th night/day and August 23-28th nights/days).

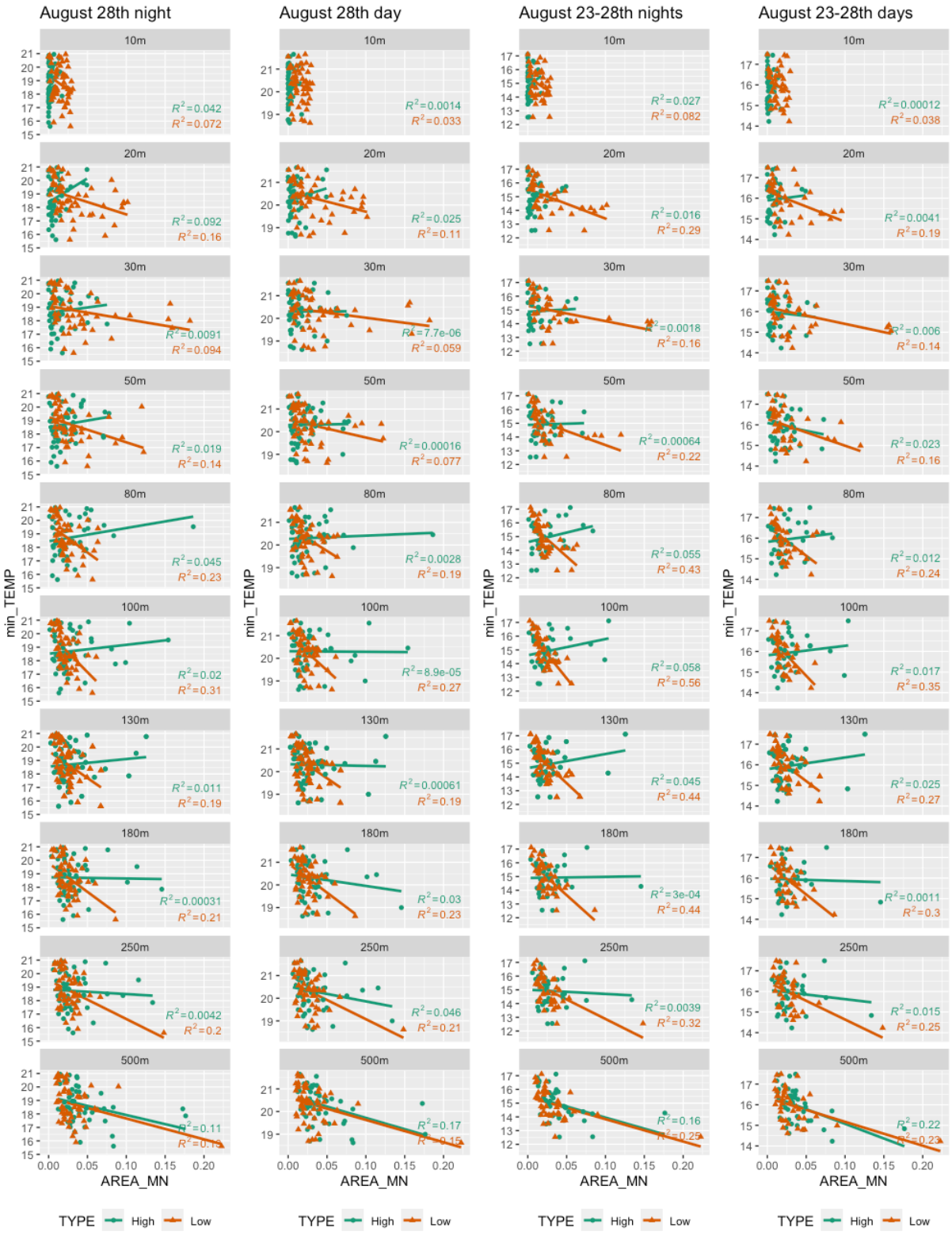

Figure 8.9: Scatterplots between minimum temperature and the mean patch size of high and low green for multiple spatial (10m, 20m, 30m, 50m, 80m, 100, 130m, 180m, 250m and 500m) and temporal scales (August 28th night/day and August 23-28th nights/days).

Figure 8.10: Scatterplots between minimum temperature and the mean shape index of high and low green for multiple spatial (10m, 20m, 30m, 50m, 80m, 100, 130m, 180m, 250m and 500m) and temporal scales (August 28th night/day and August 23-28th nights/days).

8.7.2 Maximum temperature

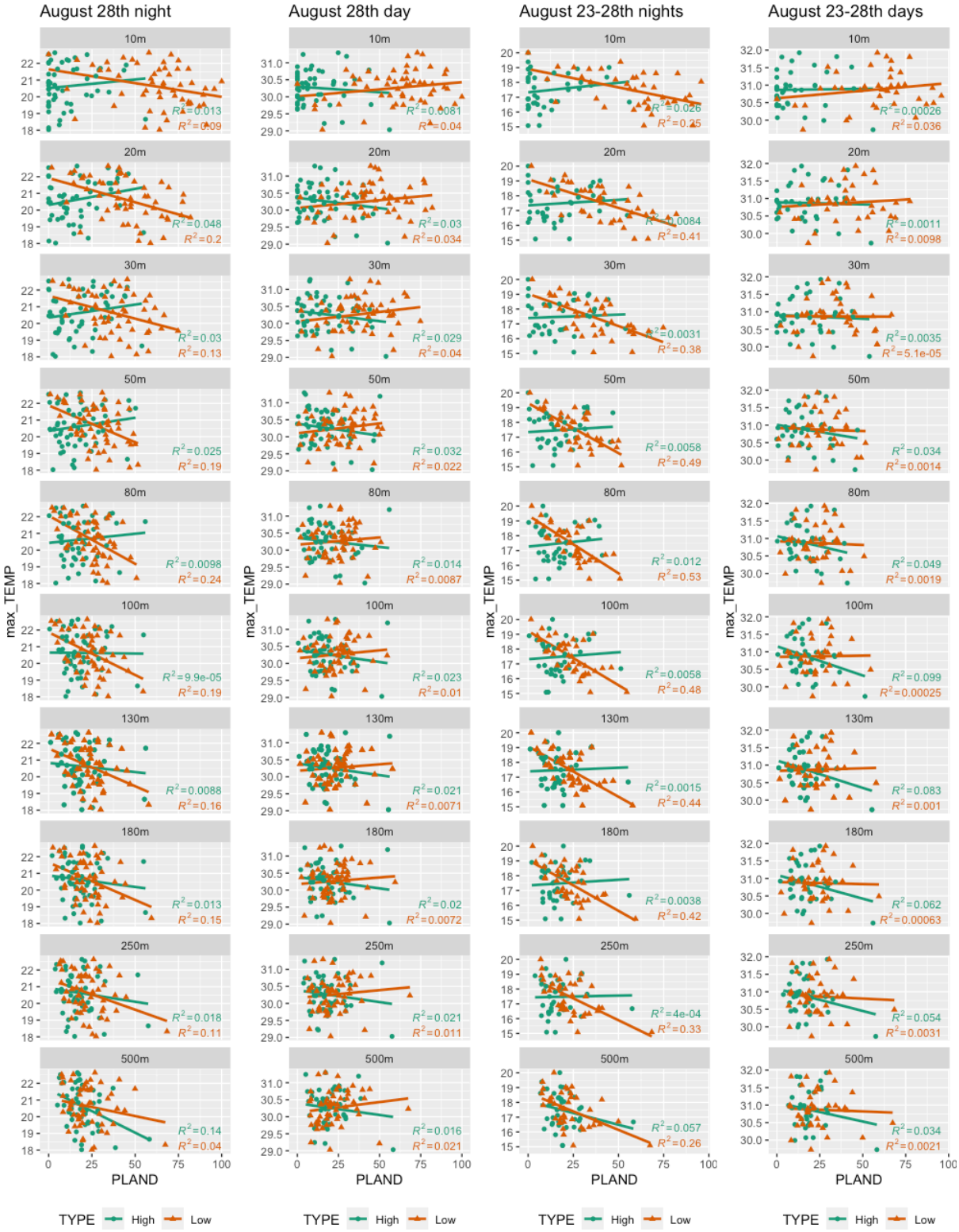

Figure 8.11: Scatterplots between maximum temperature and the percentage cover of high and low green for multiple spatial (10m, 20m, 30m, 50m, 80m, 100, 130m, 180m, 250m and 500m) and temporal scales (August 28th night/day and August 23-28th nights/days).

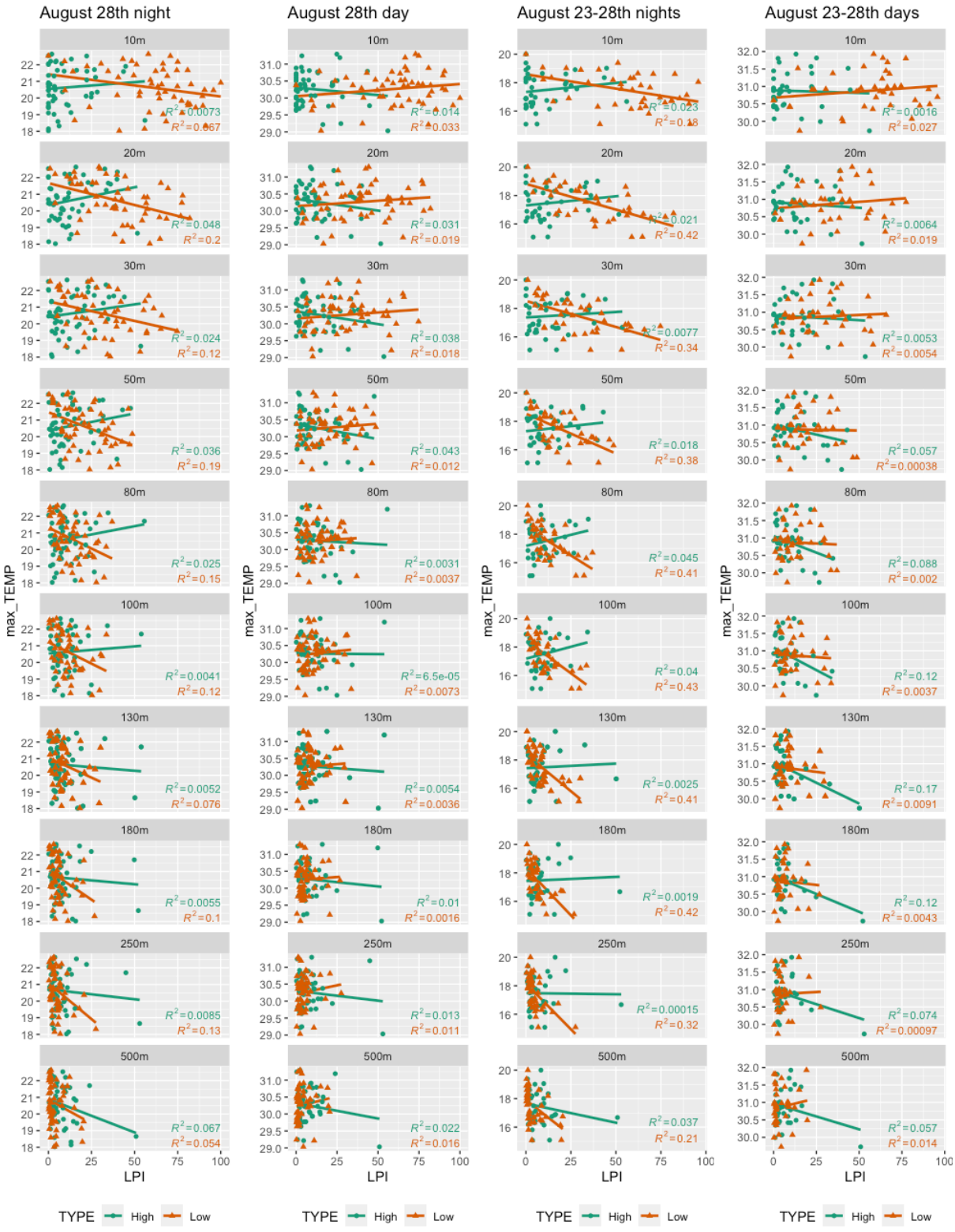

Figure 8.12: Scatterplots between maximum temperature and the largest patch index of high and low green for multiple spatial (10m, 20m, 30m, 50m, 80m, 100, 130m, 180m, 250m and 500m) and temporal scales (August 28th night/day and August 23-28th nights/days).

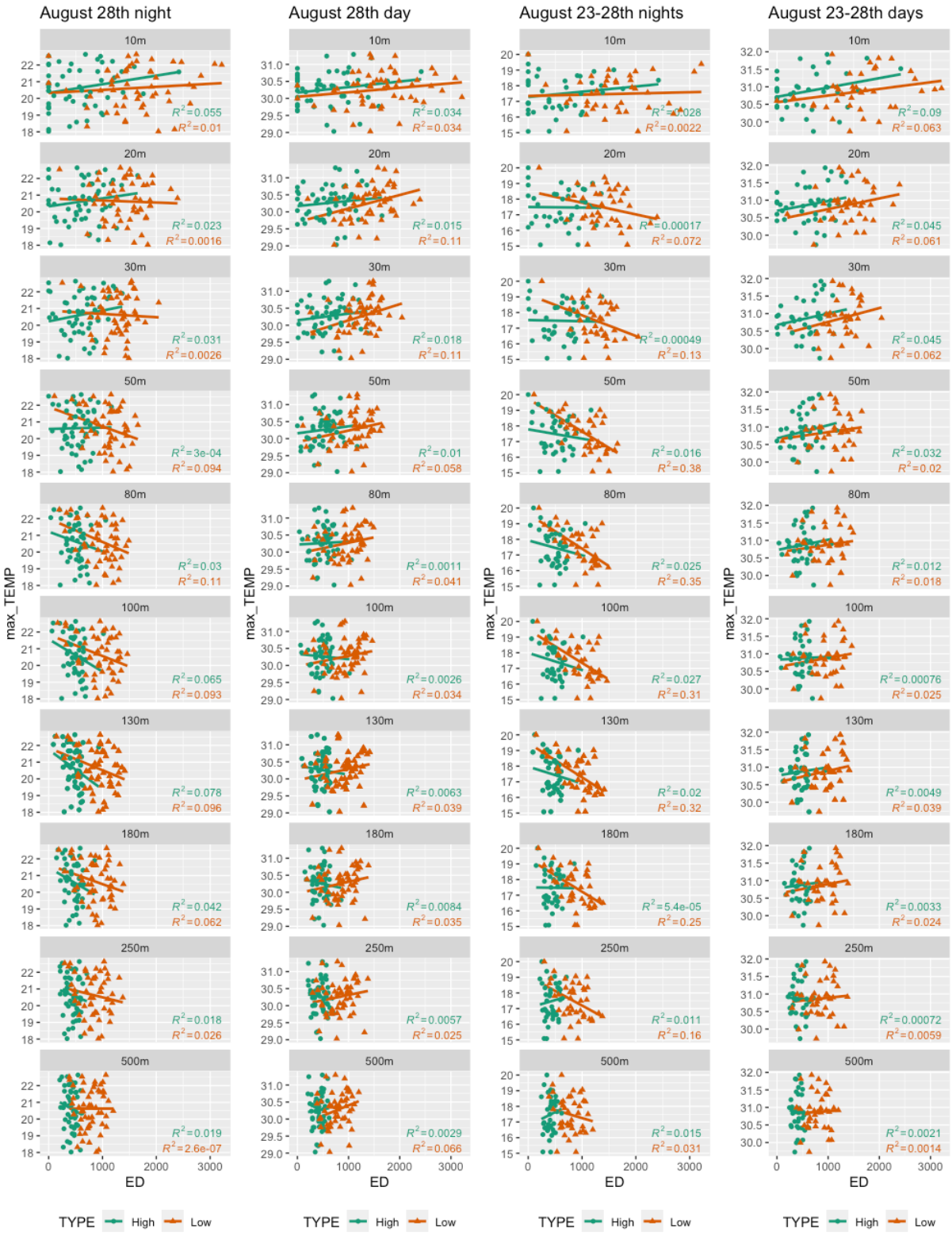

Figure 8.13: Scatterplots between maximum temperature and the edge density of high and low green for multiple spatial (10m, 20m, 30m, 50m, 80m, 100, 130m, 180m, 250m and 500m) and temporal scales (August 28th night/day and August 23-28th nights/days).

Figure 8.14: Scatterplots between maximum temperature and the patch density of high and low green for multiple spatial (10m, 20m, 30m, 50m, 80m, 100, 130m, 180m, 250m and 500m) and temporal scales (August 28th night/day and August 23-28th nights/days).

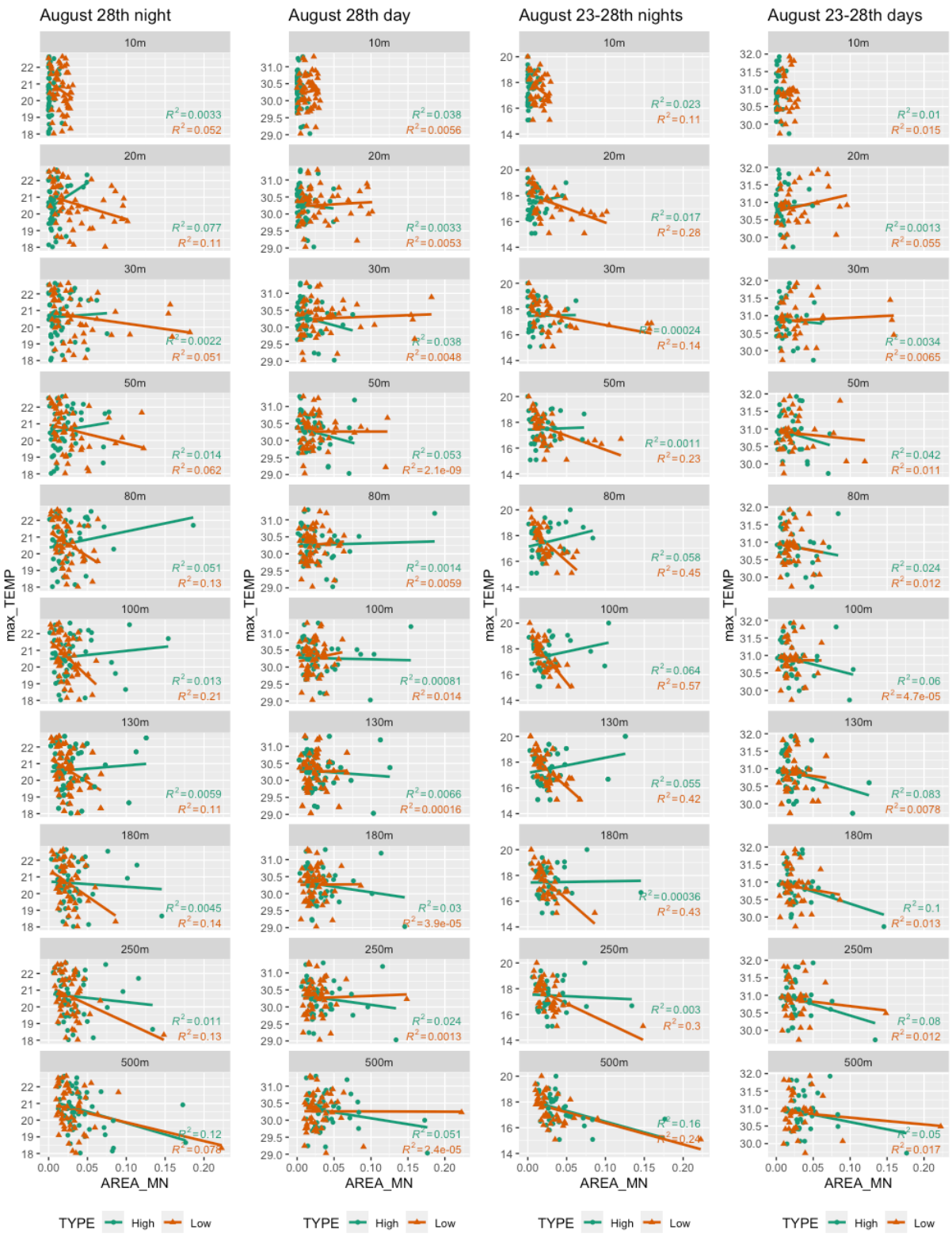

Figure 8.15: Scatterplots between maximum temperature and the mean shape index of high and low green for multiple spatial (10m, 20m, 30m, 50m, 80m, 100, 130m, 180m, 250m and 500m) and temporal scales (August 28th night/day and August 23-28th nights/days).

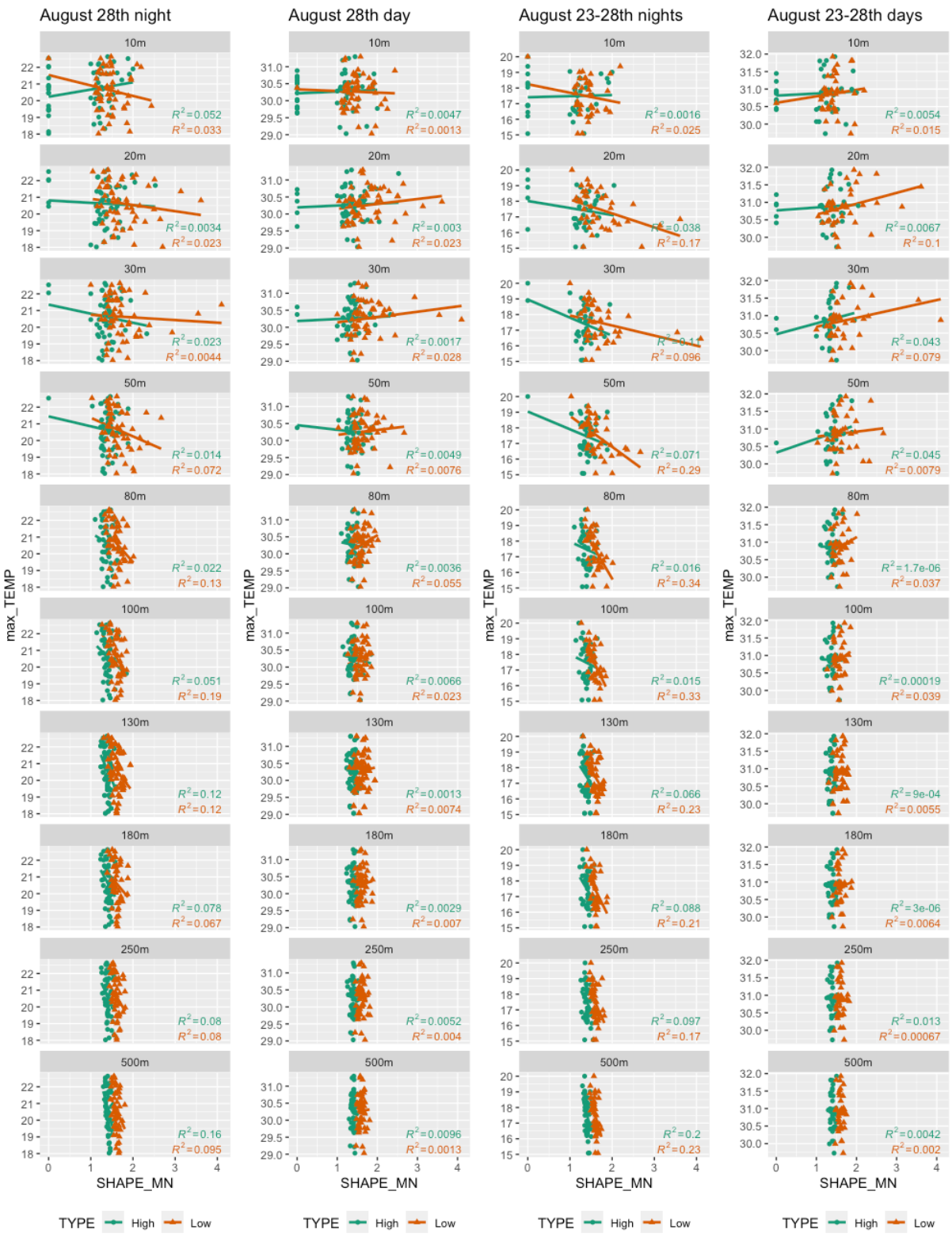

Figure 8.16: Scatterplots between maximum temperature and the mean shape index of high and low green for multiple spatial (10m, 20m, 30m, 50m, 80m, 100, 130m, 180m, 250m and 500m) and temporal scales (August 28th night/day and August 23-28th nights/days).

8.7.3 Mean temperature

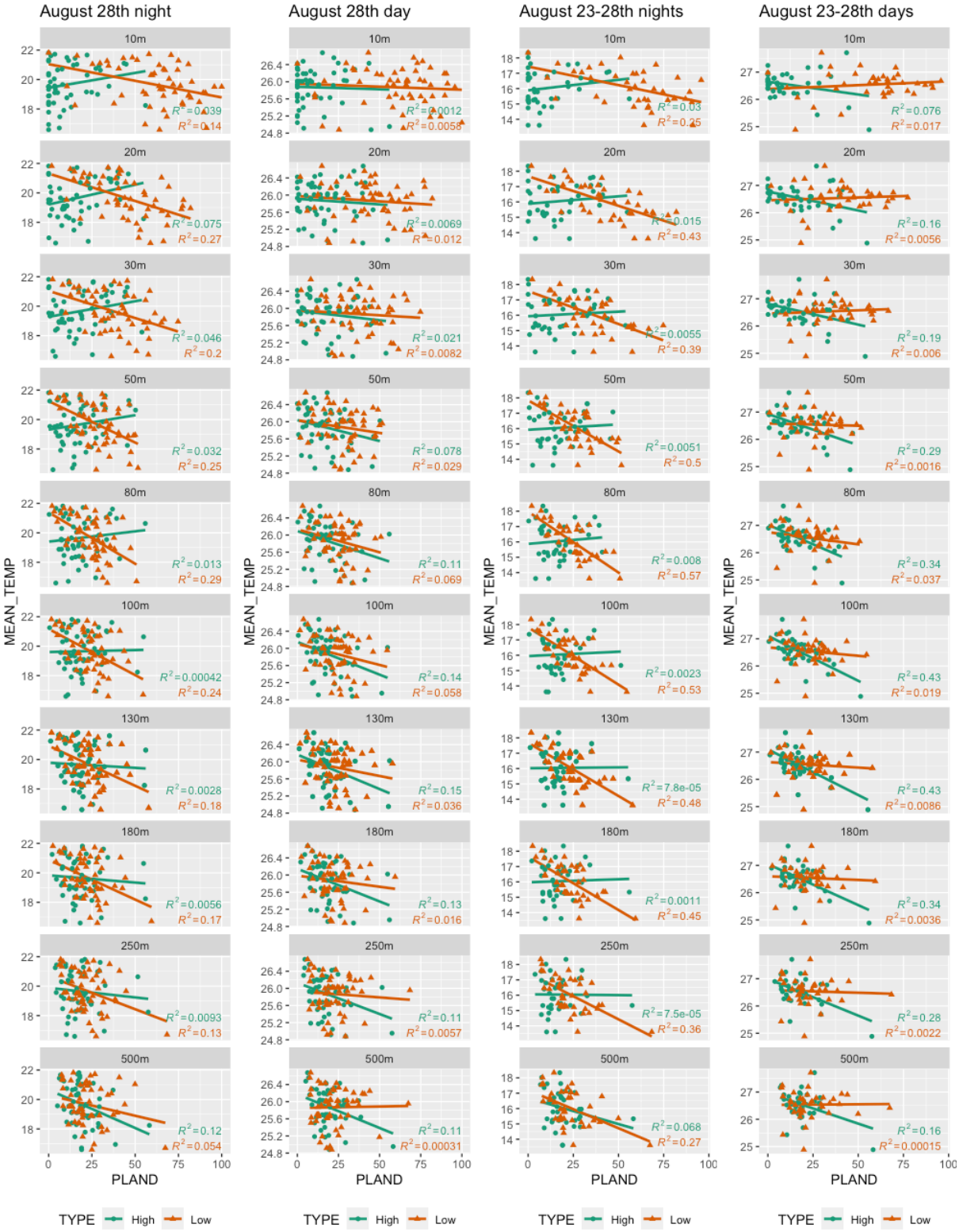

Figure 8.17: Scatterplots between mean temperature and the percentage cover of high and low green for multiple spatial (10m, 20m, 30m, 50m, 80m, 100, 130m, 180m, 250m and 500m) and temporal scales (August 28th night/day and August 23-28th nights/days).

Figure 8.18: Scatterplots between mean temperature and the largest patch index of high and low green for multiple spatial (10m, 20m, 30m, 50m, 80m, 100, 130m, 180m, 250m and 500m) and temporal scales (August 28th night/day and August 23-28th nights/days).

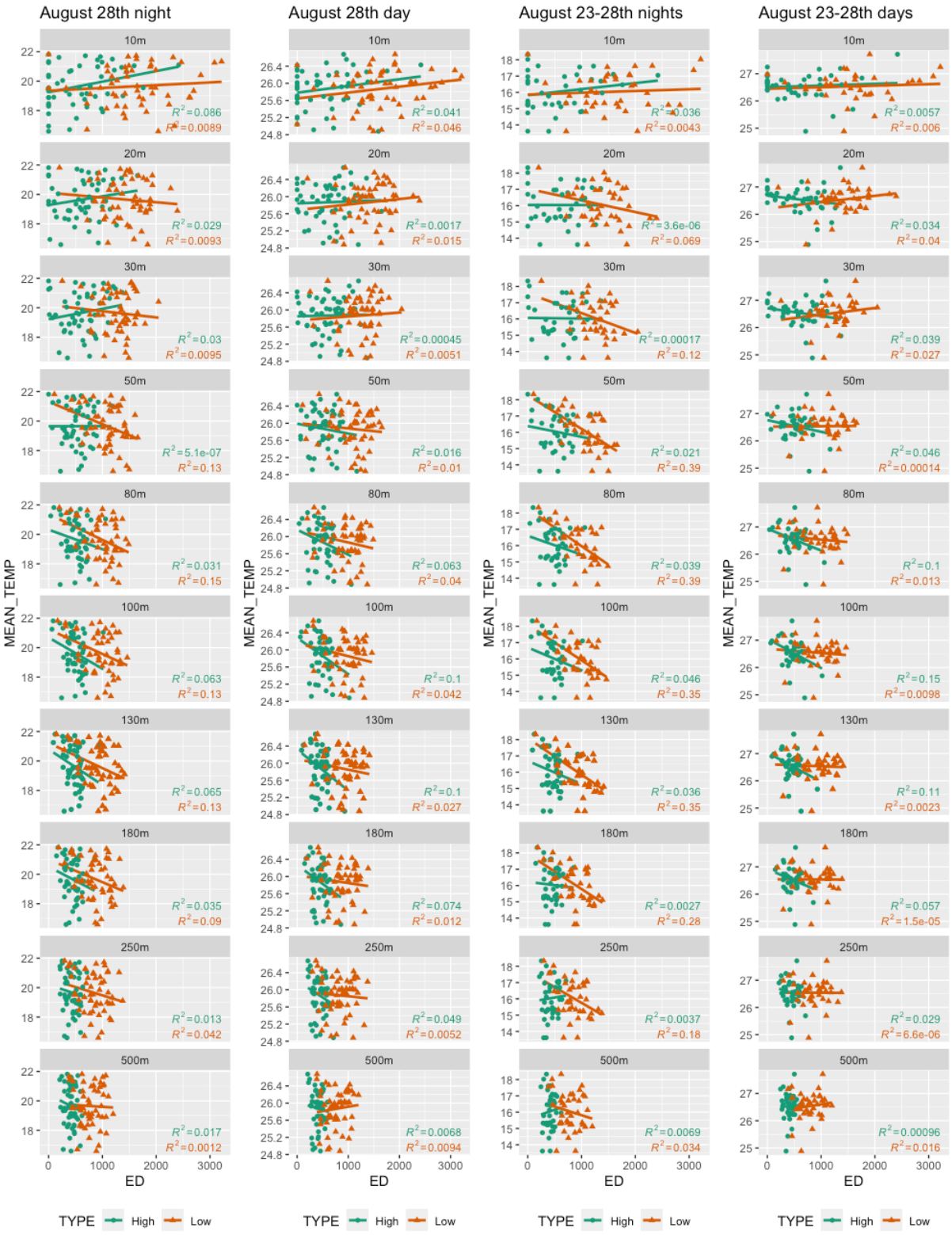

Figure 8.19: Scatterplots between mean temperature and the edge density of high and low green for multiple spatial (10m, 20m, 30m, 50m, 80m, 100, 130m, 180m, 250m and 500m) and temporal scales (August 28th night/day and August 23-28th nights/days).

Figure 8.20: Scatterplots between mean temperature and the patch density of high and low green for multiple spatial (10m, 20m, 30m, 50m, 80m, 100, 130m, 180m, 250m and 500m) and temporal scales (August 28th night/day and August 23-28th nights/days).

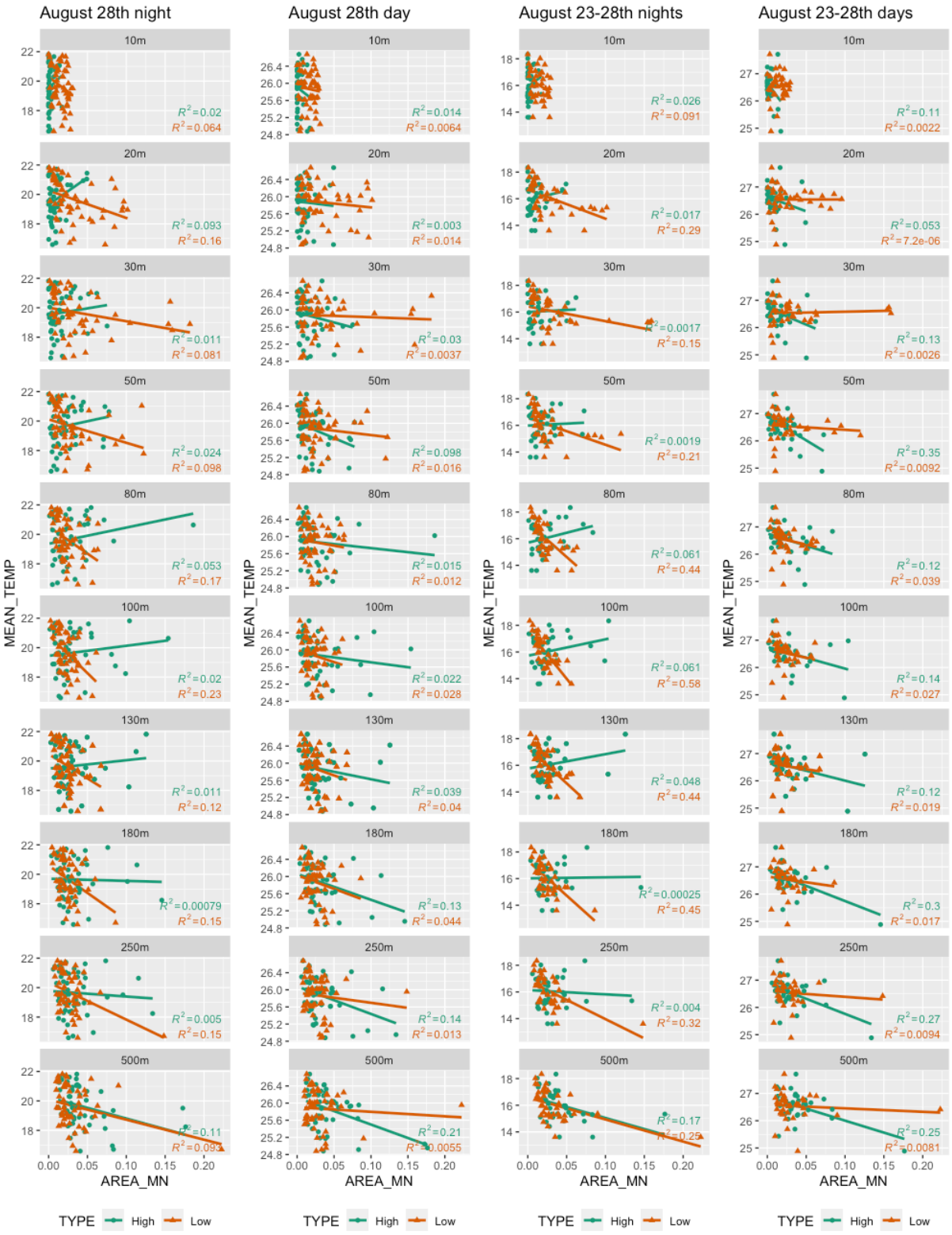

Figure 8.21: Scatterplots between mean temperature and the mean shape index of high and low green for multiple spatial (10m, 20m, 30m, 50m, 80m, 100, 130m, 180m, 250m and 500m) and temporal scales (August 28th night/day and August 23-28th nights/days).

Figure 8.22: Scatterplots between mean temperature and the mean shape index of high and low green for multiple spatial (10m, 20m, 30m, 50m, 80m, 100, 130m, 180m, 250m and 500m) and temporal scales (August 28th night/day and August 23-28th nights/days).

8.7.4 Sum of temperature difference

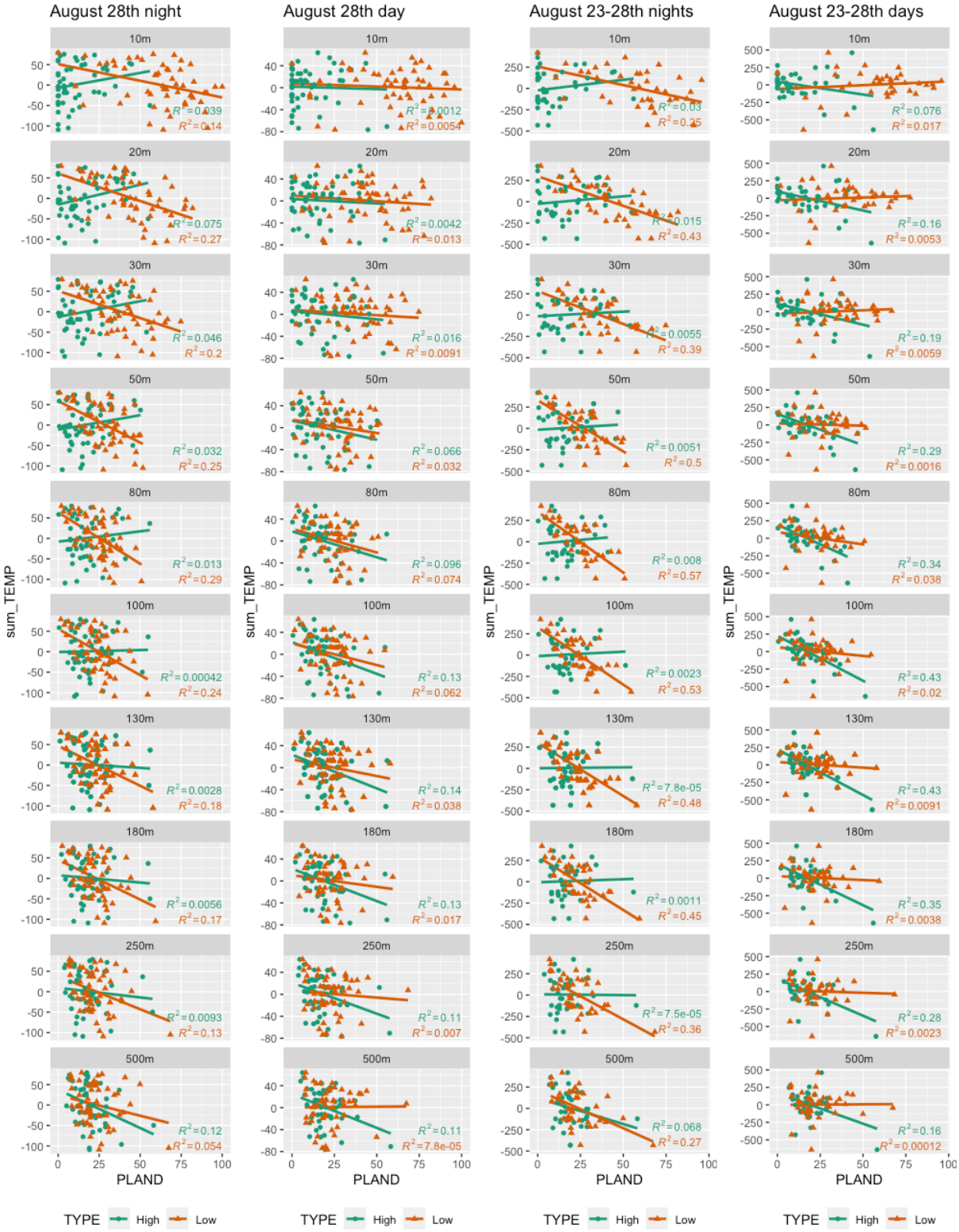

Figure 8.23: Scatterplots between the temperature sum and the percentage cover of high and low green for multiple spatial (10m, 20m, 30m, 50m, 80m, 100, 130m, 180m, 250m and 500m) and temporal scales (August 28th night/day and August 23-28th nights/days).

Figure 8.24: Scatterplots between the temperature sum and the largest patch index of high and low green for multiple spatial (10m, 20m, 30m, 50m, 80m, 100, 130m, 180m, 250m and 500m) and temporal scales (August 28th night/day and August 23-28th nights/days).

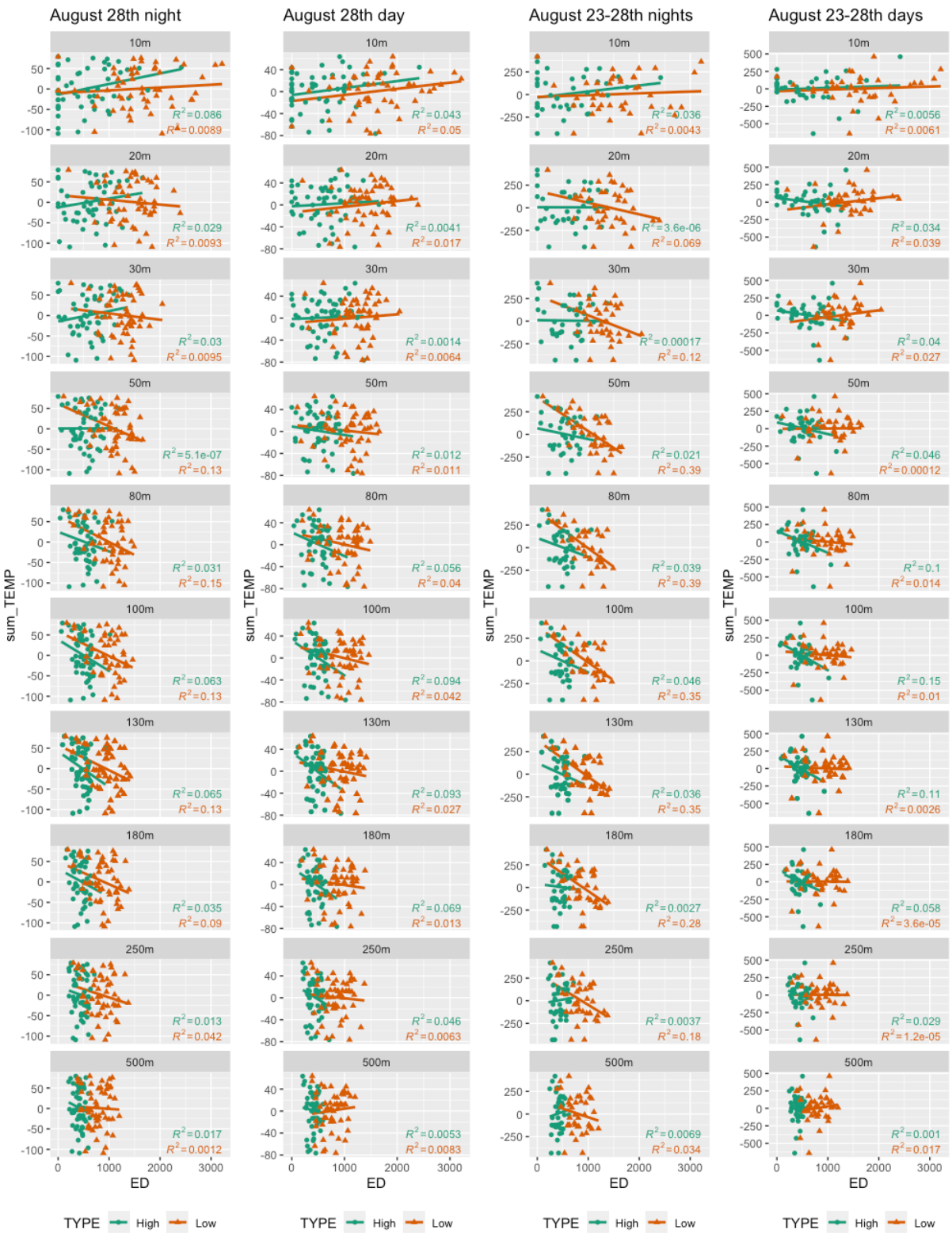

Figure 8.25: Scatterplots between the temperature sum and the edge density of high and low green for multiple spatial (10m, 20m, 30m, 50m, 80m, 100, 130m, 180m, 250m and 500m) and temporal scales (August 28th night/day and August 23-28th nights/days).

Figure 8.26: Scatterplots between the temperature sum and the patch density of high and low green for multiple spatial (10m, 20m, 30m, 50m, 80m, 100, 130m, 180m, 250m and 500m) and temporal scales (August 28th night/day and August 23-28th nights/days).

Figure 8.27: Scatterplots between the temperature sum and the mean patch size of high and low green for multiple spatial (10m, 20m, 30m, 50m, 80m, 100, 130m, 180m, 250m and 500m) and temporal scales (August 28th night/day and August 23-28th nights/days).

Figure 8.28: Scatterplots between the temperature sum and the mean shape index of high and low green for multiple spatial (10m, 20m, 30m, 50m, 80m, 100, 130m, 180m, 250m and 500m) and temporal scales (August 28th night/day and August 23-28th nights/days).

8.7.5 Discomfort index

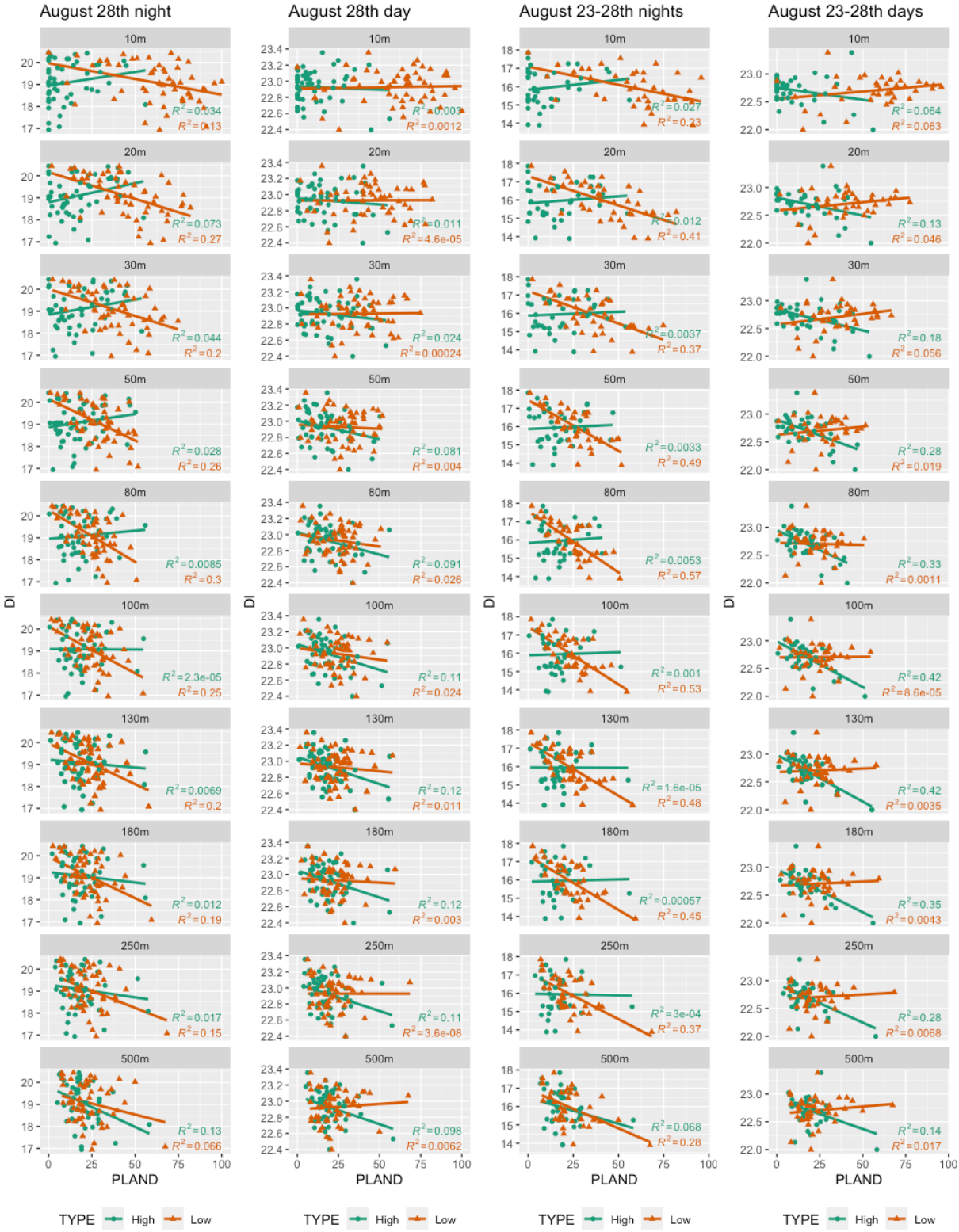

Figure 8.29: Scatterplots between the discomfort index and the percentage cover of high and low green for multiple spatial (10m, 20m, 30m, 50m, 80m, 100, 130m, 180m, 250m and 500m) and temporal scales (August 28th night/day and August 23-28th nights/days).

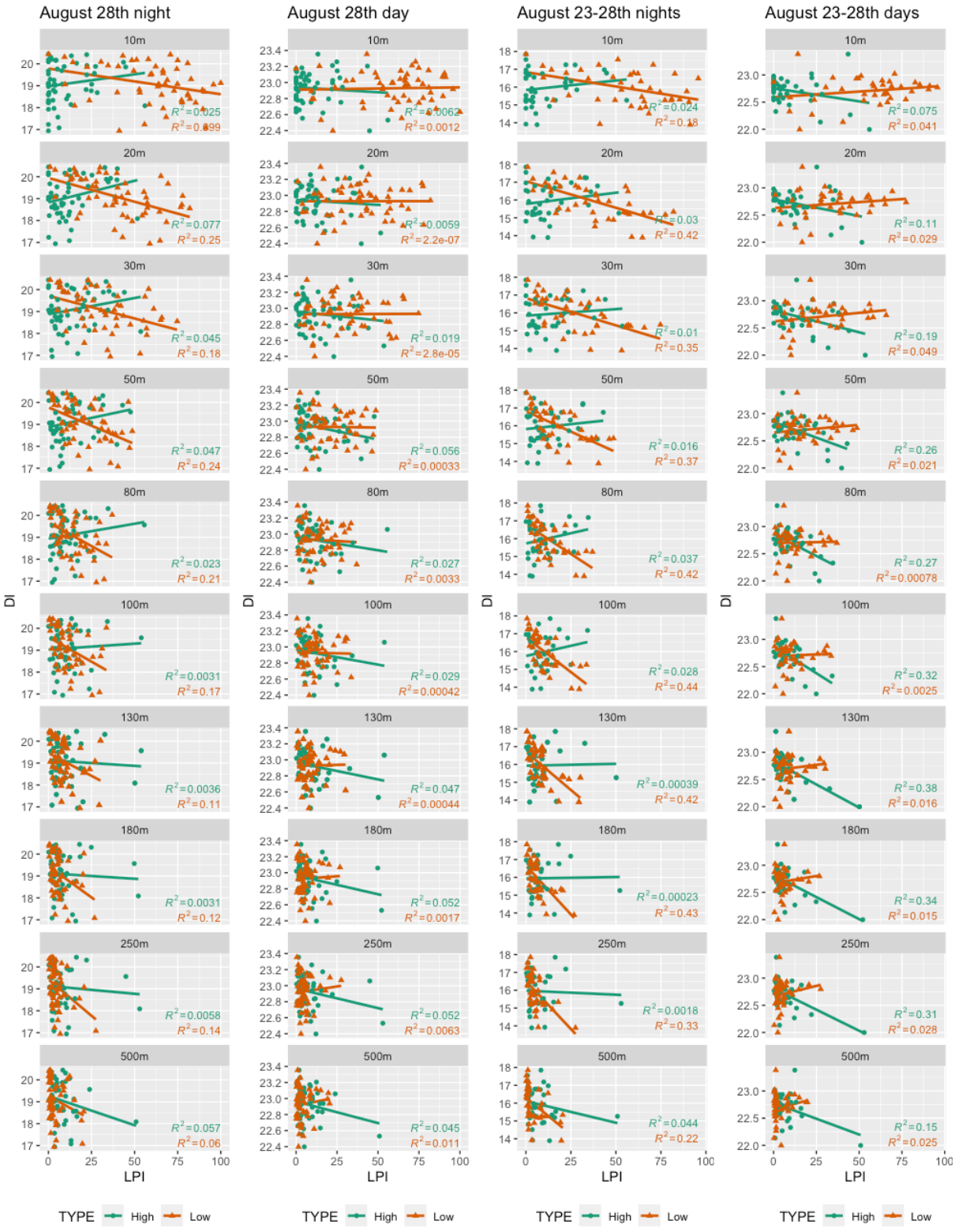

Figure 8.30: Scatterplots between the discomfort index and largest patch index of high and low green for multiple spatial (10m, 20m, 30m, 50m, 80m, 100, 130m, 180m, 250m and 500m) and temporal scales (August 28th night/day and August 23-28th nights/days).

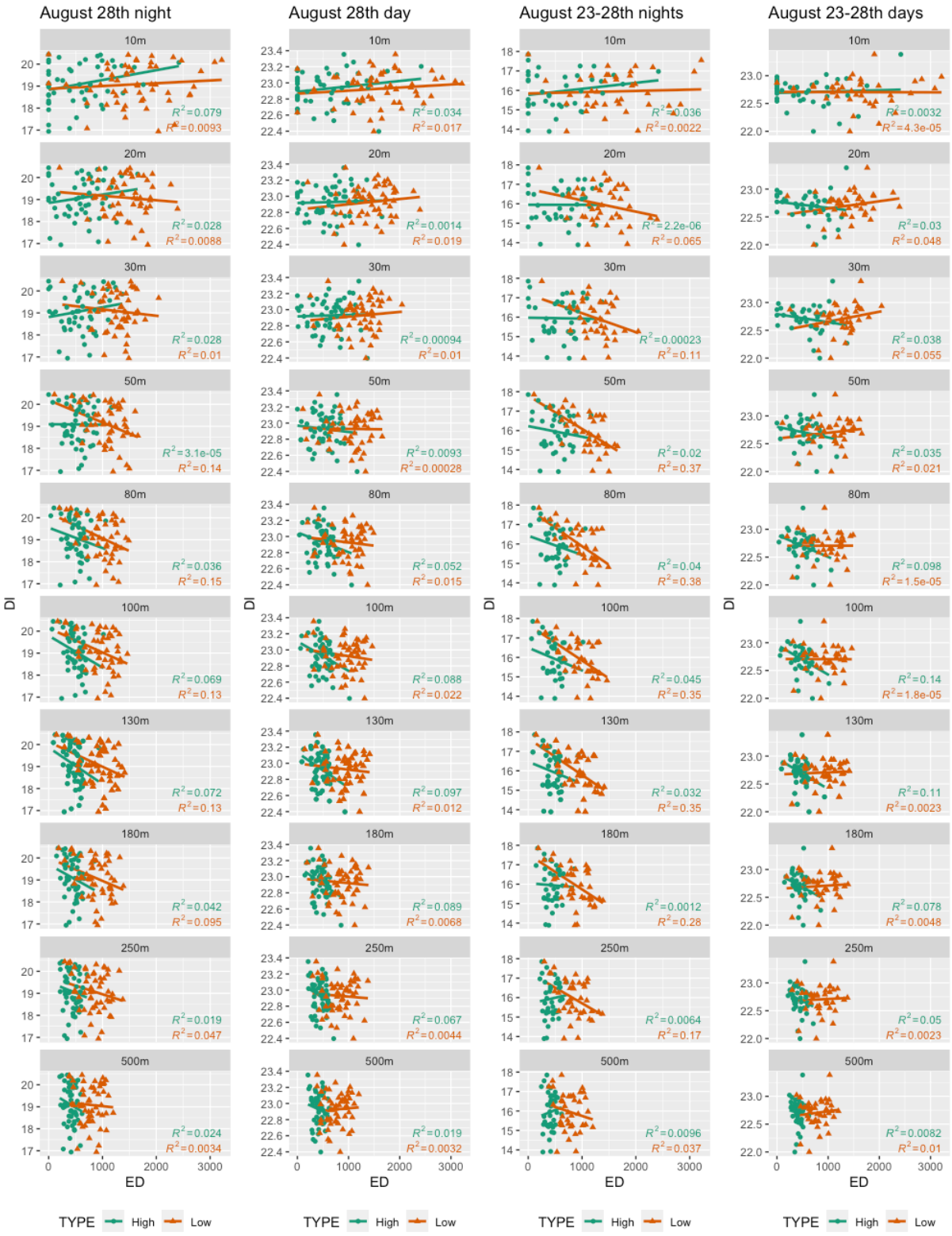

Figure 8.31: Scatterplots between the discomfort index and the edge density of high and low green for multiple spatial (10m, 20m, 30m, 50m, 80m, 100, 130m, 180m, 250m and 500m) and temporal scales (August 28th night/day and August 23-28th nights/days).

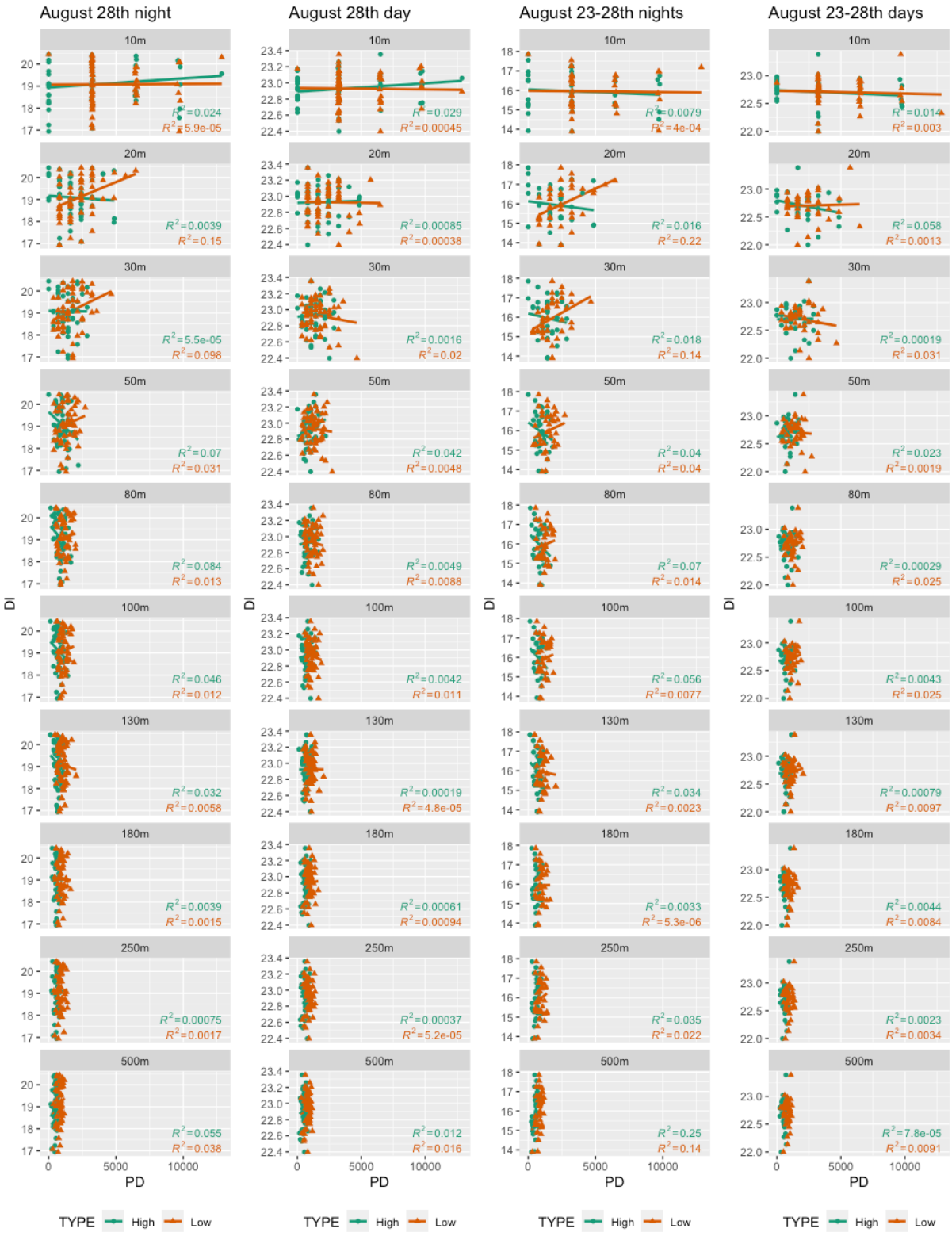

Figure 8.32: Scatterplots between the discomfort index and the patch density of high and low green for multiple spatial (10m, 20m, 30m, 50m, 80m, 100, 130m, 180m, 250m and 500m) and temporal scales (August 28th night/day and August 23-28th nights/days).

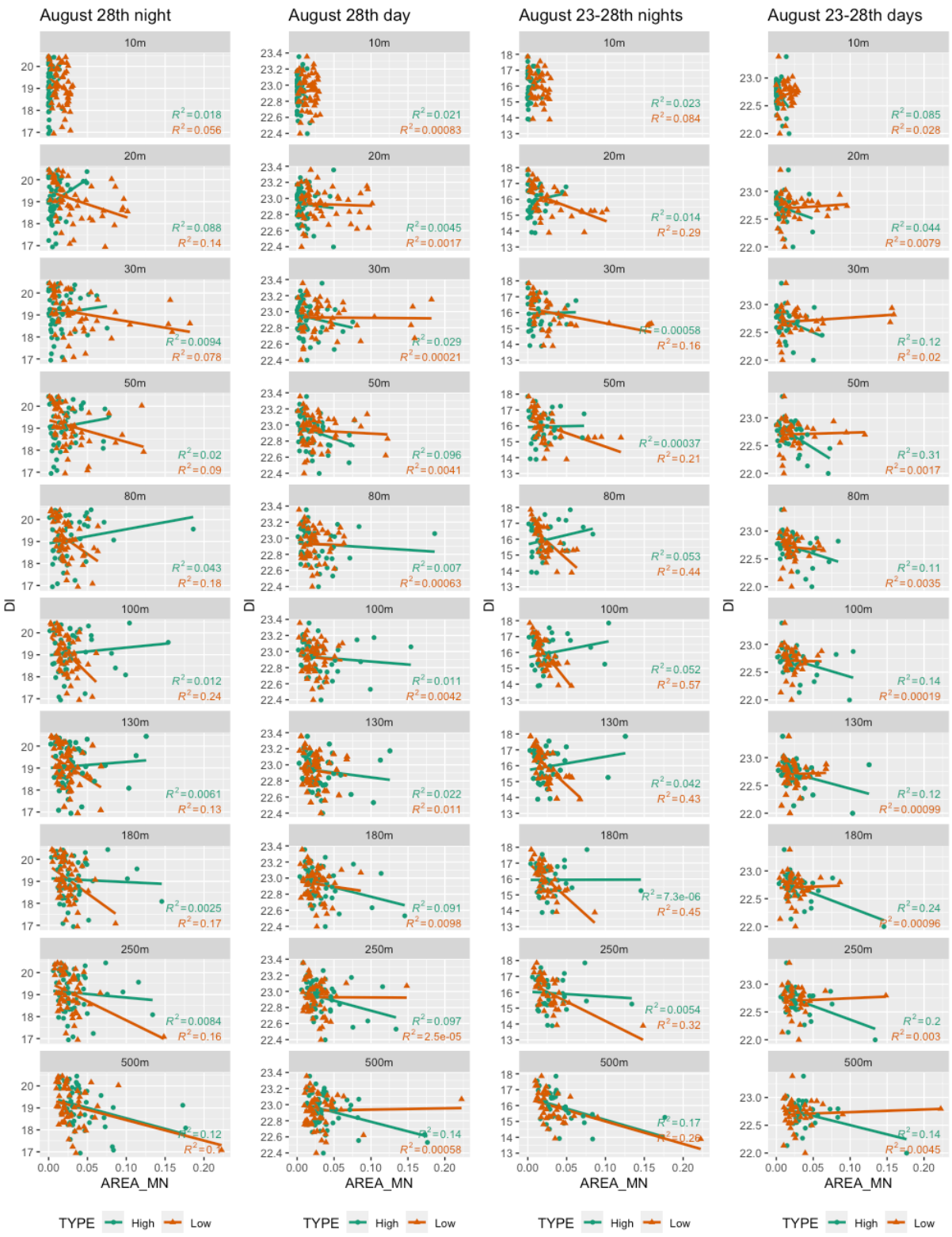

Figure 8.33: Scatterplots between the discomfort index and mean patch size of high and low green for multiple spatial (10m, 20m, 30m, 50m, 80m, 100, 130m, 180m, 250m and 500m) and temporal scales (August 28th night/day and August 23-28th nights/days).

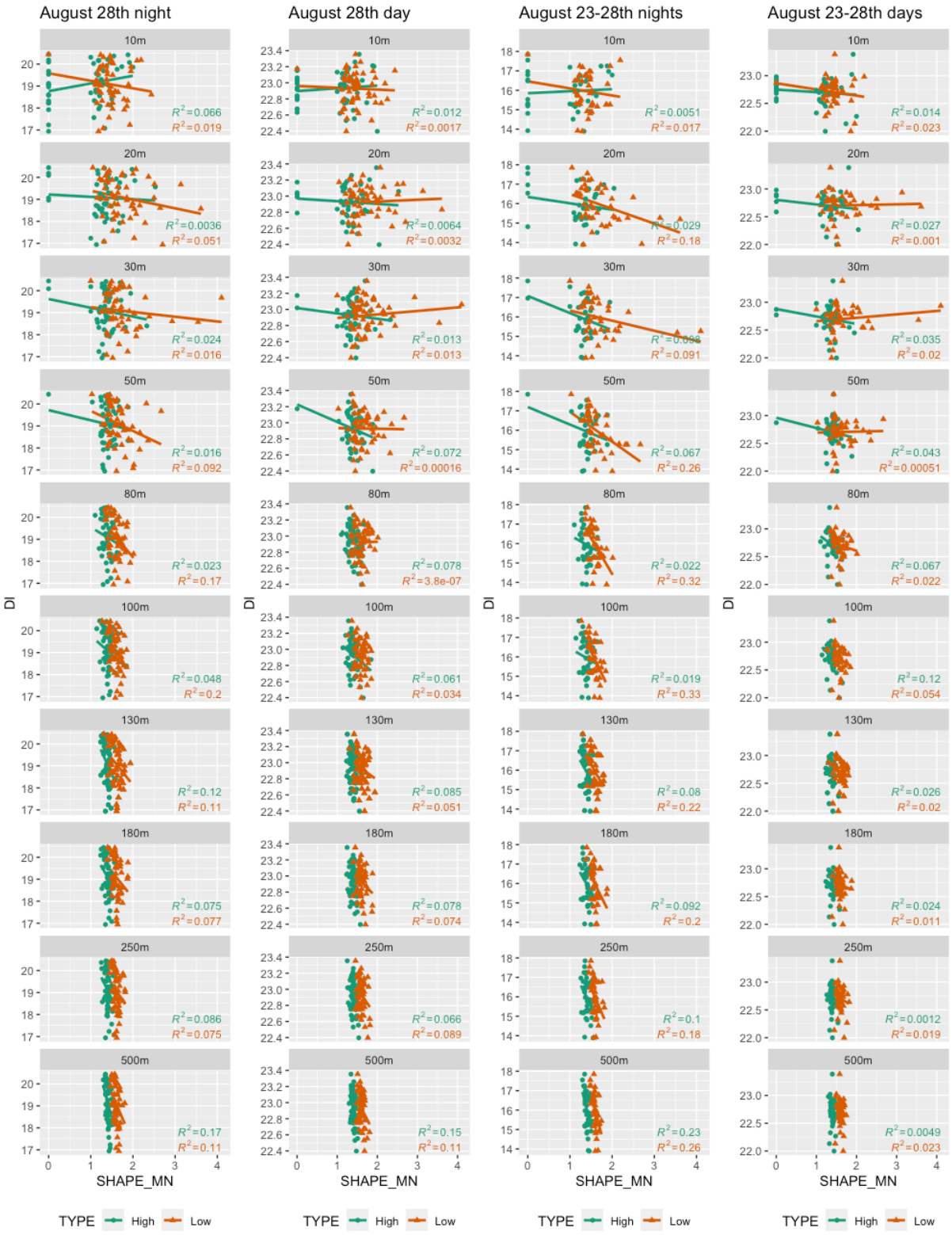

Figure 8.34: Scatterplots between the discomfort index and the mean shape index of high and low green for multiple spatial (10m, 20m, 30m, 50m, 80m, 100, 130m, 180m, 250m and 500m) and temporal scales (August 28th night/day and August 23-28th nights/days).

9 Summary for dissemination

Today more than 50% of the world's population lives in urban areas and predictions show that this number will only rise in the upcoming decennia. During this urbanization process natural surfaces like soil and vegetation are replaced by impervious surfaces like asphalt and concrete. These surfaces tend to capture and store heat more easily, resulting in a phenomenon called urban heat islands (UHIs). UHIs are defined by higher air temperatures in city centers compared to their rural surroundings, something you may have noticed on a warm day with clear-sky conditions. Especially during heatwaves, these UHIs are highly sensible and have a negative effect on human health and well-being. The presence of vegetation or urban green is one of the most promising solutions for mitigating urban heat through evaporation and shading, hereby decreasing human discomfort. These cooling benefits are however highly affected by the abundance and variability (composition) and the spatial distribution (configuration) of urban green patches. Knowing the optimal spatial configuration of urban green would help city managers and decision makers to plan and manage their urban green in order to maximize their cooling effect.

In this research we therefore studied the urban heat island in Leuven by measuring air temperatures using a dense network of local weather stations. Next, we evaluated the cooling benefits of the composition and configuration of two types of urban green; high and low green.

The results show that both the composition and the configuration of high and low green matter in the mitigation of urban heat islands. Not only increasing the percentage cover of high and low green but also larger vegetation blocks with more complex shapes will significantly lower urban air temperatures and subsequently mitigate heat stress. The cooling effect of the two urban green types, high and low green, does however vary for different spatial and temporal scales. At night, low green was found to be the most important mitigating factor along all spatial extents. During daytime, high green was more effective in reducing urban air temperatures and human discomfort.

This research can thus provide important insights for urban green planning and design. We have shown that different urban green types, shapes and sizes at multiple spatial scales are needed to improve thermal comfort of citizens during both night and day.